UC San Diego

UC San Diego Electronic Theses and Dissertations

Title

Coupled Plasmid Systems for Adaptive Bacterial Cancer Therapy

Permalink

https://escholarship.org/uc/item/4r41n9f2

ISBN

9798171605124

Author

Steppe, Paige Lucile

Publication Date

2026-10-19

Supplemental Material

https://escholarship.org/uc/item/4r41n9f2#supplemental

Peer reviewed|Thesis/dissertation

eScholarship.org Powered by the California Digital Library
University of California

UNIVERSITY OF CALIFORNIA SAN DIEGO

Coupled Plasmid Systems for Adaptive Bacterial Cancer Therapy

A dissertation submitted in partial satisfaction of the
requirements for the degree Doctor of Philosophy

in

Bioengineering

by

Paige Steppe

Committee in charge:

Professor Jeff Hasty, Chair
Professor Stephanie Fraley
Professor Gurol Suel
Professor Karsten Zengler

2026

Copyright

Paige Steppe, 2026

All rights reserved.

The Dissertation of Paige Steppe is approved, and it is acceptable in quality and form for publication on microfilm and electronically.

University of California San Diego

2026

DEDICATION

To my family for encouraging my endless questions and
my San Diego community for teaching me to explore the unknown.

EPIGRAPH

Somewhere between the
bottom of the climb and the summit
is the answer to the mystery
why we climb.

Greg Child

TABLE OF CONTENTS

Dissertation Approval Page iii

Dedication iv

Epigraph v

Table of Contents vi

List of Figures ix

List of Tables xi

List of Supplemental Videos xii

Acknowledgements xiii

Vita xv

Abstract of the Dissertation xvi

Chapter 1 Introduction 1
1.1 Bacteria as Therapeutic Agents 1
1.2 The Tumor Microenvironment as a Design Space 2
1.3 Engineering Population-Level Therapeutic Control 4
1.4 Evolutionary Robustness as a Design Constraint 6
1.5 Coupled Plasmid Systems 8
1.6 Dissertation Overview 10

Chapter 2 Phenotypic Patterning through Copy Number Adaptation to Environmental Gradients 13
2.1 Abstract 13
2.2 Introduction 14
2.3 Results and Discussion 16
2.3.1 Microfluidic Device for Plasmid Copy Number Control 16
2.3.2 Modeling of Copy-Number Based Patterning 18
2.3.3 Phenotypic Patterning from Environmental Fluctuations 20
2.3.4 Long-Term Genetic Memory of Population Phenotype 23
2.4 Discussion 25
2.5 Materials and Methods 26
2.5.1 Microfluidics and Microscopy 26
2.5.2 Agent-Based Computational Model 27
2.5.3 Molecular Cloning and Cell Culture 28
2.5.4 Microfluidic Chip Fabrication 28
2.5.5 Data Analysis 29

2.6 Supplemental Figures 29

Chapter 3 Physiological Context Reshapes the Dynamics of Coupled Bacterial Circuits 35
3.1 Abstract 35
3.2 Introduction 36
3.3 Results 37
3.3.1 Microfluidic Platform Design and Fabrication 38
3.3.2 SLC Dynamics under Hypoxic Conditions 40
3.3.3 Duplicate Origin Strain Behavior in the Microfluidic Testbed 43
3.3.4 Cancer Co-culture and Chassis-Dependent Therapeutic Reach 45
3.3.5 DNA Biosensing across Physiological Matrices 47
3.4 Discussion 50
3.4.1 Limitations of the Study 51
3.5 Materials and Methods 52
3.5.1 Microfluidic Device Development and Fabrication 52
3.5.2 Bacterial Strain Preparation 52
3.5.3 Media Preparation 53
3.5.4 Mammalian Cell Culturing 53
3.5.5 Microfluidic Device Loading 54
3.5.6 Microscopy 54
3.5.7 Data Processing 54
3.6 Supplemental Figures 55

Chapter 4 A Lactate-Gated Synchronized Lysis Circuit within a Coupled Plasmid Framework 63
4.1 Abstract 63
4.2 Introduction 64
4.3 Results 66
4.3.1 Construction of TME-Sensing Reporters and Lactate-Induced Burden . . 66
4.3.2 Lactate-Responsive Copy Number Shifting in the dOri_Lac System 67
4.3.3 Spatial Patterning to Discrete and Continuous Lactate Gradients 71
4.3.4 Functional Modulation of Delivery Strains in Response to Lactate 71
4.4 Discussion 74
4.5 Materials and Methods 76
4.5.1 Cell Culturing 76
4.5.2 Anaerobic Cell Culturing 76
4.5.3 Microfluidic Runs 76
4.5.4 Data Analysis 77
4.6 Supplemental Figures 77

Chapter 5 General Discussion 82
5.1 From Controlled Clones to Adaptive Populations 83
5.2 Physiological Context as a Design Variable 83
5.3 Adaptive Delivery through Copy Number Competition 85

5.4 Generalizability and Future Directions 86

Bibliography 89

LIST OF FIGURES

Figure 1.1. General bacterial strategies for cancer therapy. 3

Figure 1.2. The synchronized lysis circuit (SLC). 6

Figure 1.3. Overview of dissertation approach. 11

Figure 2.1. Depiction of the hypothesized spatial distribution of the coupled plasmid system. 17

Figure 2.2. Computational model for spatial distribution of plasmid coupling. 18

Figure 2.3. Copy Number Based Phenotype Separation. 21

Figure 2.4. Copy Number Based Memory Post Induction. 24

Supplemental Figure 2.1. Microfluidic device design details. 29

Supplemental Figure 2.2. Fluorescent quantification of dOri_S3 over time for every trap size and media condition, including single-inducer controls. . 30

Supplemental Figure 2.3. Fluorescent quantification of the control strain with different origins of replication on each plasmid over time for every trap size and media condition. 30

Supplemental Figure 2.4. Fluorescent quantification of dOri_S1 over time for every trap size and mixed-media condition. 31

Supplemental Figure 2.5. Fluorescent quantification of dOri_S2 over time for every trap size and mixed-media condition. 31

Supplemental Figure 2.6. Simulation with no environmental inducer. 31

Supplemental Figure 2.7. Simulation with sustained environmental inducers. 32

Supplemental Figure 2.8. Plasmid quantification over time with inducer removal at varying maximum plasmid capacities. 32

Supplemental Figure 2.9. Histograms depicting simulated frequency of p_1 plasmid counts for a colony under various strengths of dual, uniform inducers. 33

Figure 3.1. Modular testbed for engineered bacteria. 39

Figure 3.2. TME testbed recapitulates *in vivo* SLC dynamics. 42

Figure 3.3. Duplicate origin strain patterning in the microfluidic testbed. 44

Figure 3.4. Cancer co-culture testbed reveals effect of therapeutic chassis. 46

Figure 3.5. DNA biosensing in the gut lumen and solid tissue testbed. 49

Supplemental Figure 3.1. Independent modularity of nutrient distribution and hydrogel composition. 57

Supplemental Figure 3.2. Quorum coupling propagation and matrix mechanics. 58

Supplemental Figure 3.3. Oxygen-dependent modulation of SLC circuit dynamics. . . . 59

Supplemental Figure 3.4. LBMEM supports mammalian viability while preserving strain-specific SLC dynamics. 60

Supplemental Figure 3.5. Survival of the Weakest ecology in the microfluidic testbed. . 61

Figure 4.1. Conceptual overview of adaptive bacterial therapy. 65

Figure 4.2. Characterization of tumor-microenvironment-responsive biosensors. 67

Figure 4.3. Shifting plasmid copy number in response to lactate. 69

Figure 4.4. Spatial patterning in coupled-origin bacterial populations. 70

Figure 4.5. Lactate-induced synchronized lysis circuit. 73

Supplemental Figure 4.1. Microfluidic chip design and fabrication details for Chapter 4 experiments. 78

Supplemental Figure 4.2. Additional TME biosensor construction and validation data. . 79

Supplemental Figure 4.3. dOri_SLC-A batch culture characterization. 80

Supplemental Figure 4.4. dOri_SLC behavior in variable trap size gradient device. 80

LIST OF TABLES

Table 3.1. Engineered bacterial strains used throughout this dissertation. 56

LIST OF SUPPLEMENTAL VIDEOS

Steppe_dOriPattern.mp4

Steppe_LongrangeSLC.mov

Steppe_dOriSLC0mMLac.mp4

Steppe_dOriSLC8mMLac.mp4

ACKNOWLEDGEMENTS

My family planted the first seeds of my scientific mind. Through your unwavering support and countless sacrifices, you nourished every question I ever asked. Mom, Dad, the Johnson family: you constructed the foundation this dissertation is built upon. Steppe, I have always looked up to you. Thank you for setting the bar so high and challenging me to rise to meet it.

Thank you to my San Diego community for teaching me that you must pour into all aspects of your life to perform your best work. My climbing community in particular taught me to face the unknown with curiosity rather than hesitation.

Vic, my love, you have been by my side for nearly this entire journey. Your daily support at home and your constant encouragement to keep me growing have meant more than I can say. I am so grateful to have gained a second family in yours.

Kat, no matter how much time passes between us, your presence feels unchanged. The way you ask questions of everyone around you has always inspired me to dig deeper.

Koe, you believe in me more then I do myself. The way you both tackle challenges head on with no fear and slow to embrace the seasons of life, has profoundly inspired me.

Katie, where do I even begin. You have been with me through every single part of this. From the surf lineup to the morning coffee chats to the work commutes, through my highest moments and my lowest ones: thank you sticking with me through all of it.

Camilo, you taught me to love science again when I was ready to walk away. Your passion is contagious, and the energy you bring to lab every day transformed my entire Ph.D. experience.

Shalni, I treasured every Art of Espresso morning walk and everything that came from them.

Chloe, there is no one I would rather constantly be breaking science with.

To the entire Hasty Lab, thank you for the day-to-day support, the picnic table lunches, and for making it possible to do this science at all.

Jeff, I would not have finished this degree without you. You were in my corner before I was even your student, and you have gone far beyond what mentorship requires. Thank you for guiding me not only through the science but through everything that surrounds it.

Chapter 1, is a partial reprint of the material as it appears in Steppe, P.*, O'Connor, K.*, and Hasty, J. Rational engineering of combinatorial bacterial therapies for cancer. Genome Biology. (2026).

Chapter 2, in full, is a reprint of the material as it appears in Steppe, P.*, Rey-Bedón, C.*, Kumar, S., Forrest, E., Van Der Wagt, N., Tayal, A., Tsimring, L., and Hasty, J. Phenotypic Patterning through Copy Number Adaptation to Environmental Gradients. *ACS Synthetic Biology* (2024). The dissertation author was a primary investigator and co-first author of this paper.

Chapter 3, in part, is currently being prepared for submission for publication of the material. Rey-Bedón, C.*, Steppe, P.*, Rosen, A. Emmanuele, P., Cooper, R., Zarrinpar, A., and Hasty, J. Microphysiological test-bed for engineered bacteria. The dissertation author was a primary investigator and co-first author of this paper.

Chapter 4, in full, is currently being prepared for submission for publication of the material. 2. Steppe, P.*, Kumar, S.*, Erkok, D., Tayal, A., and Hasty, J. Adaptive therapeutic delivery through plasmid coupling in bacteria. The dissertation author was a primary investigator and co-first author of this paper.

VITA

2021 Bachelor of Science in Chemical and Biomolecular Engineering, Georgia Tech, Atlanta

2026 Doctor of Philosophy in Bioengineering, University of California San Diego

PUBLICATIONS

Paige Steppe[*], Katherine O'Connor[*], and Jeff Hasty. Rational engineering of combinatorial bacterial therapies for cancer. *Genome Biology* 27, 53 (2026). https://doi.org/10.1186/s13059-026-03951-0

Katherine O'Connor[*], **Paige Steppe**[*], Daniel Worthley, Jeff Hasty, and Robert Cooper. Bacteria as living biosensors for DNA. *Nature Reviews Bioengineering* (2025).

Kierra A. Franklin, J. Harrison Priode, **Paige Steppe**, and Karmella A. Haynes. An engineered chromatin protein with enhanced preferential binding of H3K27me3 over H3K9me3. *bioRxiv* (2024).

Paige Steppe[*], Camilo Rey-Bedón[*], Shalni Kumar, Emerald Forrest, Niklas Van Der Wagt, Arnav Tayal, Lev Tsimring, and Jeff Hasty. Phenotypic Patterning through Copy Number Adaptation to Environmental Gradients. *ACS Synthetic Biology* (2024).

Yan Zhang, **Paige Steppe**, Maxwell Kazman, and Mark P. Styczynski. Point-of-care analyte quantification and digital readout via lysate-based cell-free biosensors interfaced with personal glucose monitors. *ACS Synthetic Biology* (2021).

Monica P. McNerney, Yan Zhang, **Paige Steppe**, Adam D. Silverman, Michael C. Jewett, and Mark P. Styczynski. Point-of-care biomarker quantification enabled by sample-specific calibration. *Science Advances* (2019).

Submitted

Paige Steppe[*], Shalni Kumar[*], Deniz Erkok, Arnav Tayal, and Jeff Hasty. Adaptive therapeutic delivery through plasmid coupling in bacteria. *Genome Biology* (2026, Submitted).

In Preparation

Camilo Rey-Bedón[*], **Paige Steppe**[*], Alex Rosen, Philip Emmanuele, Robert Cooper, Amir Zarrinpar, and Jeff Hasty. Microphysiological test-bed for engineered bacteria. *Cell Resources* (2026, Final Editing Stage).

([*] authors contributed equally)

ABSTRACT OF THE DISSERTATION

Coupled Plasmid Systems for Adaptive Bacterial Cancer Therapy

by

Paige Steppe

Doctor of Philosophy in Bioengineering

University of California San Diego, 2026

Professor Jeff Hasty, Chair

Engineered bacteria are emerging as programmable therapeutics capable of colonizing solid tumors and delivering therapeutic payloads with spatial precision. Yet most current designs rely on fixed genetic architectures that cannot adapt to the heterogeneous conditions of the tumor microenvironment. Here, coupled plasmid systems offer a generalizable framework for encoding adaptive behavior into bacterial therapeutics. In these systems, two constructs sharing an origin of replication compete for replication machinery, enabling population-level phenotypic flexibility that is directly responsive to environmental context. Using a microfluidic gradient platform, we demonstrate that coupled plasmid strains undergo stable spatial differentiation in response to opposing chemical gradients, with a stochastic model confirming that copy number competition

is sufficient to generate this organization without additional regulatory circuitry. Using a modular tissue-scale testbed designed to recapitulate tumor microenvironmental conditions, we find that oxygen availability drives spatially graded synchronized lysis circuit (SLC) triggering while extracellular matrix architecture modulates AHL-mediated quorum coupling across tissue-relevant distances. Integrating these principles, we couple lactate-responsive lysis with the SLC within a coupled-origin framework, producing a strain that autonomously switches between sensing and delivery phenotypes as a function of local lactate concentration and releases therapeutic payload in a cyclical, self-regulated manner. Together these results establish that coupled plasmid systems can translate environmental heterogeneity into organized therapeutic function, offering a generalizable architecture for programming adaptive behavior into living medicines.

Chapter 1

Introduction

1.1 Bacteria as Therapeutic Agents

The convergence of synthetic biology and oncology has transformed bacteria from passive tumor colonizers into programmable living therapeutics. Although traditional cancer treatments like chemotherapy, radiotherapy, and immunotherapy have dramatically improved patient outcomes, no single modality can fully address the biological and spatial complexity of solid tumors [1, 2, 3]. Irregular vasculature, metabolic heterogeneity, and necrotic regions limit the delivery and efficacy of conventional therapies, while systemic or repeated drug exposure can lead to dose-limiting toxicity in healthy tissues [4, 5, 6]. Bacterial species offer an alternative therapeutic option uniquely suited to these challenges: they remodel tumor architecture, activate localized antitumor immune responses through innate immunogenicity, and selectively colonize hypoxic and necrotic tumor regions [7, 8]. These natural properties provide a foundation for engineering bacteria as disease-specific therapeutic platforms capable of precision delivery within the tumor microenvironment (TME).

Using bacteria as cancer therapy dates back more than a century to William Coley's pioneering use of live microbes to provoke tumor regression [9]. Although this approach was ultimately abandoned due to inconsistent outcomes and safety concerns, recent decades have witnessed its scientific revival [10]. Contemporary genetic engineering has redefined this once empirical pipeline as a programmable platform, enabling precise control over attenuation, safety,

and payload release through rational engineering approaches [7, 8]. The surge in publications and clinical trials since the early 2000s underscores a decisive shift from proof-of-concept to translational application, narrowing the gap between preclinical innovation and clinical deployment [11].

Early bacterial therapies made extensive use of facultative or obligate anaerobes such as *Escherichia coli*, *Salmonella*, and *Clostridium*, leveraging their intrinsic tumor tropism [10, 12, 13]. Recent progress in synthetic biology has dramatically expanded the capabilities of these systems. Higher-order genetic circuits now incorporate quorum sensing [14, 15], logic gating [16], synchronized lysis [17], and environmental feedback [18, 19] to enable precisely timed, tumor-restricted function. These advances have expanded bacterial therapies from single-function payload carriers to multi-layered control systems capable of sensing environmental cues, integrating complex logic, and coordinating behavior across populations. Such programmable circuits not only improve safety and therapeutic precision but also enable bacteria to dynamically respond to the tumor microenvironment, allowing treatments to adapt in real time as tumor conditions change.

1.2 The Tumor Microenvironment as a Design Space

Solid tumors are not uniform masses of malignant cells but spatially heterogeneous ecosystems defined by competing metabolic demands, variable immune infiltration, and structural disorganization that develops as tumor growth outpaces vascularization [3]. As tumors expand, regions distant from functional blood vessels become progressively oxygen-depleted, generating a hypoxic gradient that extends from the vascularized periphery inward toward a necrotic core. This oxygen gradient is accompanied by the accumulation of metabolic byproducts, most notably lactate, that result from the shift to anaerobic glycolysis that characterizes hypoxic tumor regions [4]. The resulting microenvironment is immunosuppressive, mechanically stiff due to extracellular matrix remodeling, and largely inaccessible to systemically administered therapies

that depend on intact vasculature for delivery.

These same features that frustrate conventional treatments create a privileged niche for bacteria. Obligate and facultative anaerobes preferentially colonize hypoxic and necrotic tumor regions, achieving intratumoral accumulation ratios that can exceed those of surrounding healthy tissue by several orders of magnitude [7]. Bacterial colonization of solid tumors is not simply passive accumulation but an active process involving chemotaxis toward tumor-derived nutrients, resistance to the hypoxic microenvironment, and evasion of immune clearance that is impaired in immunosuppressed tumor cores. This intrinsic tumor tropism means that engineered bacteria can be administered systemically but concentrate their activity at the site of disease, providing a degree of therapeutic localization that no small molecule or antibody can achieve through passive distribution alone.

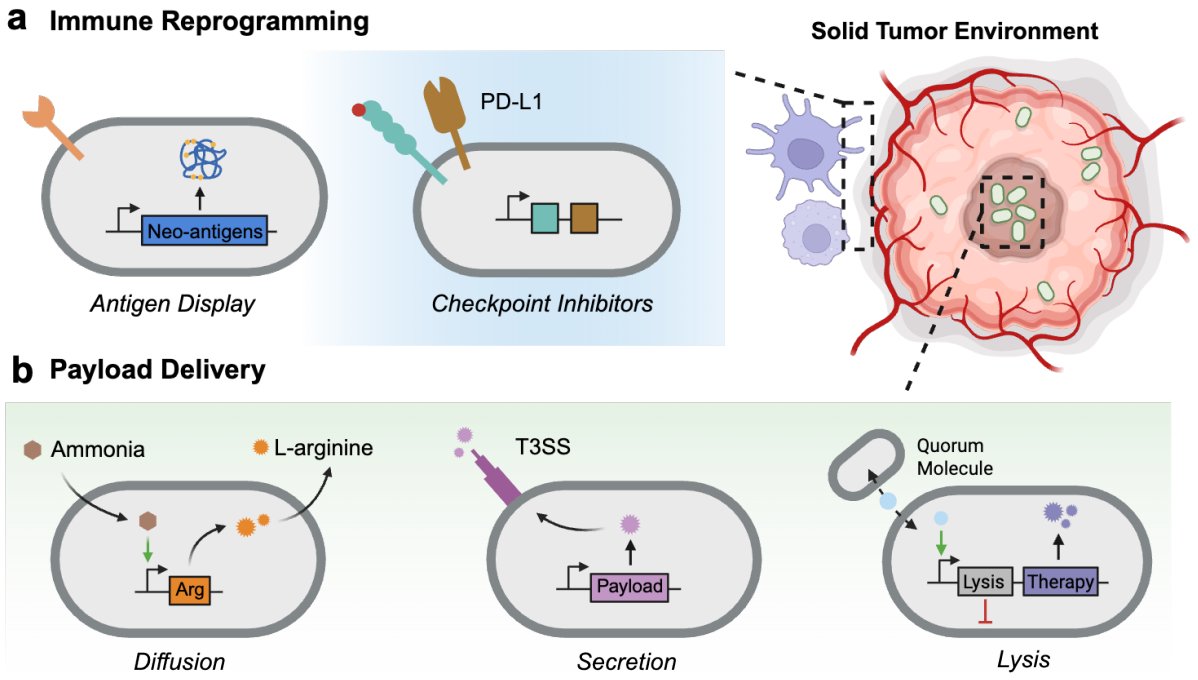


Figure 1.1. Engineered bacterial strategies for immune modulation and therapeutic delivery in solid tumors. a Immune reprogramming. Bacteria can be engineered to display neoantigens or secrete checkpoint-modulating proteins, enabling targeted engagement of immune cells within the tumor microenvironment. b Payload delivery. Therapeutic molecules can be delivered through diffusion of metabolic or small-molecule payloads, active secretion systems such as T3SS, or quorum-regulated lysis circuits that coordinate population-wide release of intracellular therapies.

Beyond colonization, bacteria interact with the TME in ways that can be exploited for therapy. Their recognition by innate immune receptors triggers local inflammatory responses that can remodel the tumor immune landscape, converting immunosuppressive environments into ones permissive for T-cell activity [8]. Bacterial surface components, secretion systems, and lysis products can deliver immunomodulatory payloads directly within the tumor stroma, and the spatial confinement of bacterial populations to the TME provides a natural mechanism for restricting therapeutic activity to the site of disease. The challenge is not whether bacteria can colonize and persist in tumors, a property well established across numerous preclinical models, but whether they can be engineered to execute complex, precisely timed therapeutic programs once there.

1.3 Engineering Population-Level Therapeutic Control

The ability to program bacteria to deliver therapeutic payloads in a controlled manner rather than through constitutive expression or passive diffusion represents a central goal of the field. Early engineered strains relied on simple transcriptional circuits linking TME-responsive promoters to payload genes, achieving a degree of tumor-specificity but limited temporal control over when and how much therapeutic material was released [19]. A more sophisticated approach exploits the collective behavior of bacterial populations to coordinate therapeutic output at a defined density threshold, using quorum sensing as the regulatory mechanism.

Quorum sensing is a cell-to-cell communication system in which bacteria produce and detect diffusible signaling molecules, known as *N*-acyl homoserine lactones (AHLs) in Gram-negative species, whose extracellular concentration scales with population density [14]. Above a threshold concentration, AHL binding to its cognate transcription factor activates gene expression in a population-coordinated manner, allowing large numbers of cells to switch behavior simultaneously. In its natural context, quorum sensing regulates behaviors including biofilm formation, virulence factor secretion, and bioluminescence that are only beneficial when

the population is large enough to produce a collective effect. In synthetic biology, this property has been repurposed as a population-level switch for coordinating therapeutic output across an engineered bacterial community.

One of the most influential implementations of this principle is the synchronized lysis circuit (SLC), first developed in the Hasty Lab and representing the conceptual foundation upon which this dissertation builds [14]. The SLC encodes a positive feedback loop through the *Lux* quorum sensing operon, in which LuxI produces AHL and LuxR activates further LuxI expression upon AHL binding. As a bacterial population grows and intracellular AHL accumulates past a threshold, this positive feedback drives expression of the phiX174E lysis gene, causing population-wide cell death and release of intracellular contents, including any therapeutic payload encoded in the same circuit. Because a fraction of cells lyse before reaching the quorum threshold, a subpopulation survives and reseeds the colony, allowing the population to regrow and repeat the lysis cycle. This produces a pulsatile, oscillatory pattern of therapeutic release that is self-regulated by bacterial population dynamics rather than external control inputs.

The SLC framework proved influential not only as a delivery mechanism but because it integrated a built-in safeguard for biocontainment: pulsatile lysis prevents unconstrained bacterial growth and continuously resets population density, limiting the accumulation of bacteria within the tumor to a self-regulated steady state [14]. Subsequent work extended the SLC to deliver immunomodulatory payloads including GM-CSF, α-PD-L1, and α-CTLA-4 nanobodies, demonstrating robust antitumor effects in preclinical models [17]. Separately, efforts to improve the spatial specificity of bacterial therapeutics have employed TME-responsive promoters to restrict bacterial colonization and survival to tumor tissue, linking environmental signals such as hypoxia, lactate, and acidity to the regulation of essential bacterial genes [18, 19]. These two lines of work, population-level lysis control and TME-responsive transcriptional regulation, have largely advanced in parallel, and their combination has remained elusive in part because both operate through the same design logic: fixed genetic architectures that respond to environmental inputs but do not adapt to them. What has been missing is a mechanism that allows the

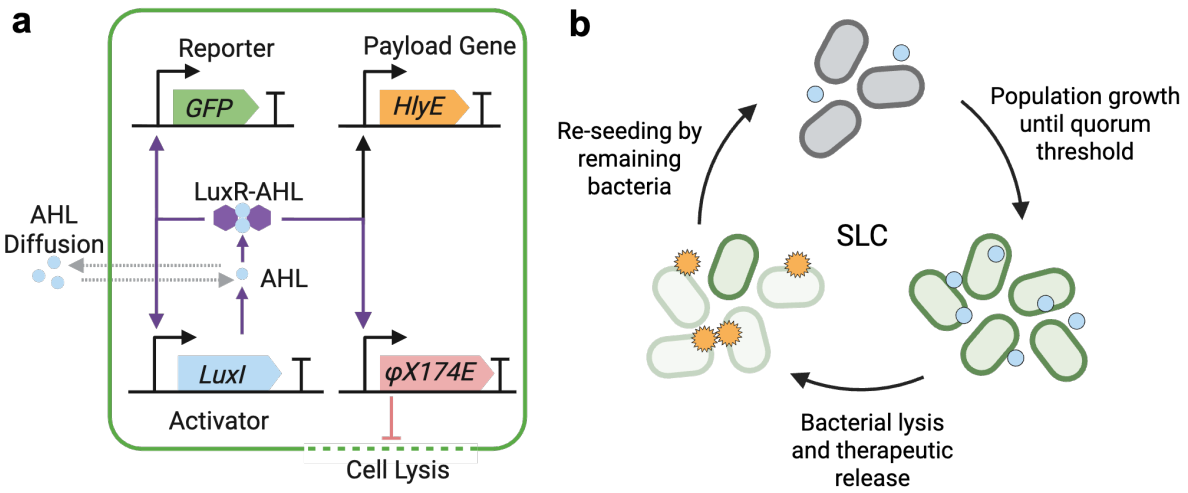


Figure 1.2. The synchronized lysis circuit (SLC). (a) Genetic architecture of the SLC. LuxI produces the quorum sensing molecule AHL, which accumulates with population density and drives LuxR-AHL-mediated positive feedback, ultimately activating expression of the lysis gene *φX174E* and a co-encoded payload gene of Hemolysin E (HlyE). (b) Population dynamics of the SLC. Bacteria grow until AHL accumulates past a quorum threshold, triggering population-wide lysis and therapeutic release. A surviving subpopulation reseeds the colony, allowing the cycle to repeat in a pulsatile, self-regulated manner.

population itself to redistribute its functional resources in response to the tumor landscape, aligning therapeutic output with local conditions without requiring a new sensor or promoter for every context. This dissertation proposes that the answer lies not in more sophisticated transcriptional circuitry but in rethinking the relationship between plasmid architecture and population heterogeneity.

1.4 Evolutionary Robustness as a Design Constraint

A persistent and underappreciated challenge in engineering complex bacterial circuits for therapeutic application is evolutionary robustness: the capacity of a synthetic construct to maintain its intended function under the selective pressures that accumulate during prolonged residence in a physiological environment. In controlled laboratory conditions, bacteria carrying synthetic circuits can be maintained under antibiotic selection that penalizes plasmid loss and rewards cells with intact constructs. In vivo, this selection pressure is absent, and bacteria are

instead subject to the sustained metabolic cost of expressing foreign genetic material. The more complex the circuit, the greater this burden, and the stronger the selective advantage conferred on any cell that acquires a mutation reducing or eliminating circuit expression [20, 21].

This problem manifests in several ways. Plasmids can be lost during cell division if partitioning is imperfect, generating a population of plasmid-free cells that proliferate faster than circuit-carrying counterparts. Point mutations in promoters, ribosome binding sites, or coding sequences can reduce or abolish gene expression without eliminating the plasmid entirely, producing constructs that appear intact by sequencing but are functionally silent. In the context of a tumor, where bacteria may persist for days to weeks, even a small initial frequency of circuit-loss mutants can expand to dominate the population through clonal competition, eroding therapeutic function precisely when sustained output is most needed. Conventional approaches to managing this instability, including toxin-antitoxin systems [22, 23], active partitioning modules [24], and essential gene manipulation [25], mitigate plasmid loss but do not resolve the deeper tension between circuit complexity and evolutionary durability. Prolonged selective pressure specific to the TME can still drive mutational escape, underscoring the need for stabilization mechanisms that are architecturally integrated rather than appended.

Recent work has begun to address this problem by rethinking the relationship between copy number variation and circuit function. In conventional multi-plasmid systems, the assumption is that copy number stability is a prerequisite for reliable gene expression: fluctuations in plasmid abundance introduce variability in circuit output and are therefore to be minimized. An alternative view treats copy number variation not as noise to be suppressed but as a regulatory resource that can be harnessed. If the fitness consequences of copy number shifts can be aligned with therapeutic goals, then the same selective dynamics that ordinarily erode synthetic function can instead be used to maintain it. Coupled plasmid systems, in which two constructs share a single origin of replication and therefore compete for the same replication machinery, instantiate precisely this logic, and form the architectural basis of the work described in this dissertation.

1.5 Coupled Plasmid Systems

Bacterial cells maintain plasmids at a specific copy number through the autoregulation of the origin of replication. In the ColE1 family of origins, which includes the widely used pUC and pBR322 backbones, copy number is controlled by the balance between a replication primer and its antisense inhibitor, whose relative concentrations set replication rate at a stable equilibrium [26, 27]. Synthetic biology has long exploited this system to tune construct expression, and orthogonal origins from different incompatibility groups are routinely used when two or more plasmids must be maintained independently in the same cell [28].

When two plasmids instead share the same origin of replication, they become coupled through competition for the same autoregulatory machinery. Because the antisense inhibitor suppresses replication of any ColE1-origin plasmid regardless of its other genetic content, two such plasmids share a total copy number budget: an increase in copy number of one necessarily reduces the copy number of the other. The ratio between them is therefore not fixed by the origin sequence but governed by the relative fitness of cells carrying different distributions, which in turn depends on the metabolic burden each plasmid imposes under the current environmental conditions. Tang and Liu first demonstrated that this coupling could be used to stably record environmental events by controlling output plasmid ratios [29]. Subsequent work showed that copy number flexibility in coupled systems allows populations to minimize encoded metabolic burden as a function of environment, directing population-level adaptation toward configurations that are collectively optimal for current conditions [30, 31, 32].

What emerges from this architecture is a form of heritable phenotypic heterogeneity that does not require dedicated sensing or switching circuits. Cells carrying higher copy numbers of one plasmid occupy a distinct functional state from cells dominated by the other, and the relative frequencies of these states shift as environmental conditions change and different copy number distributions become selectively advantageous. This is analogous to the way a stem cell population maintains both self-renewal and differentiated progeny through asymmetric

division, distributing functional roles across a heterogeneous population without requiring each cell to execute a binary decision. In the context of bacterial cancer therapy, this property creates the possibility of programming a single strain to simultaneously maintain a sensing-competent subpopulation and a delivery-competent subpopulation, whose relative abundances are automatically adjusted by the environmental signals present in different tumor regions. Rather than requiring separate strains or external switching signals, coupled plasmid systems allow this functional differentiation to emerge from the architecture of the construct itself.

The tumor microenvironment is a particularly apt context for this approach. Solid tumors are not static targets but spatially and temporally heterogeneous landscapes whose metabolic and immune properties vary across regions and evolve over the course of colonization. A bacterial population engineered with a fixed genetic architecture will perform optimally only within the narrow environmental window it was designed for, becoming either ineffective or indiscriminate as conditions shift. Coupled plasmid systems resolve this mismatch by making the population's functional composition continuously responsive to local selective pressure. In lactate-rich, hypoxic tumor cores, the burden of carrying a lactate-inducible lysis plasmid selectively eliminates high-copy sensing cells, enriching for the delivery phenotype precisely where delivery is needed. In low-lactate peripheral or off-target tissue, the inverse pressure operates, maintaining the sensing-dominant state that conserves therapeutic activity for genuine tumor encounters. The architecture does not require the engineer to anticipate every condition the bacteria will face; instead, it delegates that decision to the population itself, which resolves it through fitness-based competition in real time.

Mechanistically, this buffering capacity has also been shown to protect against mutational inactivation. Because both plasmids compete for replication, a mutation that inactivates one construct does not confer an immediate growth advantage if the competing plasmid simply increases in copy number to fill the vacated replication budget, imposing its own metabolic cost. This creates a form of mutational resistance that is intrinsic to the coupled architecture, allowing cells to maintain circuit function significantly longer under evolutionary pressure than

equivalent orthogonal designs [30, 33]. In the TME, where sustained selective pressure over the timescale of therapeutic residence would otherwise erode function, this property is not merely advantageous but may be essential for maintaining reliable therapeutic output.

1.6 Dissertation Overview

This dissertation develops coupled plasmid systems as a generalizable framework for engineering adaptive bacterial cancer therapeutics. The central argument, developed across three research chapters, is that coupling plasmid origins of replication provides a single-chassis mechanism for achieving the spatial and temporal adaptability that solid tumor environments demand, without requiring the additional regulatory complexity that would otherwise make such systems evolutionarily fragile.

Chapter 2 establishes the biological principle. Using a microfluidic platform capable of maintaining continuous, opposing gradients of two chemical inducers, we demonstrate that a coupled plasmid strain undergoes pronounced phenotypic partitioning in response to environmental gradients, with distinct subpopulations emerging and stabilizing across the spatial domain within hours of gradient imposition. A stochastic computational model developed alongside these experiments recapitulates the observed patterning behavior and provides a theoretical framework for understanding how copy number competition generates stable spatial heterogeneity. These results establish that coupled plasmid systems can translate environmental gradients into organized population structure without additional regulatory circuitry, an important proof of principle for their use in spatially heterogeneous therapeutic contexts.

Chapter 3 interrogates how physiological context shapes the dynamics of coupled bacterial circuits. A modular microfluidic platform designed to recapitulate key features of the tumor microenvironment, including hypoxic gradients and a diffusion-limited extracellular matrix, is used to characterize the behavior of SLC and coupled plasmid strains under conditions that diverge substantially from well-mixed bench-scale experiments. The results reveal that oxygen

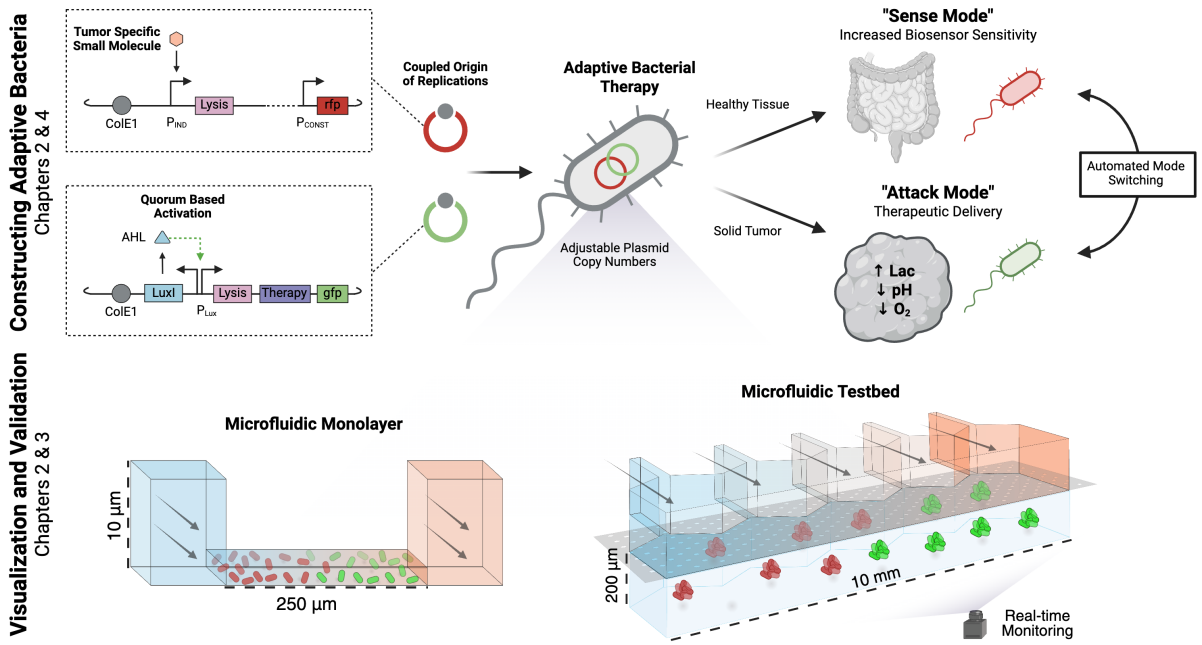


Figure 1.3. Overview of dissertation approach. (Top) Coupled plasmid architecture underlying the adaptive bacterial therapy framework. Two plasmids sharing a ColE1 origin of replication carry an environmentally inducible lysis module and a quorum sensing-driven synchronized lysis circuit, respectively. Copy number competition between the two constructs enables autonomous switching between a biosensor-dominant sense mode in healthy tissue and a therapeutically active attack mode in the solid tumor microenvironment. (Bottom) Microfluidic platforms used to characterize and validate coupled plasmid circuit dynamics. A monolayer gradient device enables single-cell resolution imaging of phenotypic patterning across chemical gradients, while a tissue-scale testbed recapitulates tumor microenvironmental conditions including hypoxic gradients and a collagen extracellular matrix for real-time circuit characterization.

availability modulates SLC triggering dynamics in a spatially graded manner, and that AHL diffusion through the matrix mediates inter-colony quorum coupling across tissue-scale distances in ways that are not observable in standard culture conditions. Critically, dOri_AHL patterning behavior established in Chapter 2 persists robustly in this physiologically structured context, confirming that the coupled plasmid architecture operates across the spatial and physical scales relevant to solid tumor colonization.

Chapter 4 applies the coupled plasmid framework to a fully integrated therapeutic design. The dOri_SLC system couples a lactate-responsive lysis module to the SLC within a shared ColE1 origin, creating a strain that autonomously switches between a sensing-dominant and delivery-

dominant phenotype as a function of local lactate concentration. This design demonstrates that copy number competition, driven here by the differential metabolic burden of the lactate-inducible and quorum-controlled lysis plasmids, can produce biomarker-dependent therapeutic output that is spatially confined to lactate-rich tumor regions and cyclically self-regulated through the SLC dynamics. Together, these chapters demonstrate that coupled plasmid systems are not a laboratory curiosity but a practical and generalizable architecture for programming adaptive behavior in bacterial therapeutics.

Chapter 1, is a partial reprint of the material as it appears in Steppe, P., O'Connor, K.*, and Hasty, J. Rational engineering of combinatorial bacterial therapies for cancer. Genome Biology. (2026) and of O'Connor*, K., Steppe*, P., Worthley, D., Hasty, J., and Cooper, R. Bacteria as living biosensors for DNA. Nature Reviews Bioengineering (2025)*

Chapter 2

Phenotypic Patterning through Copy Number Adaptation to Environmental Gradients

2.1 Abstract

Plasmid coupling, in which two constructs sharing a ColE1 origin of replication compete for replication machinery, generates copy number heterogeneity that allows bacterial populations to adapt phenotypically to environmental conditions. Here, we use plasmid coupling to produce spatially separated and phenotypically distinct subpopulations in response to heterogeneous chemical environments. Using a custom microfluidic device with continuous inducer gradients, we tracked engineered populations at single-colony resolution and observed pronounced phenotypic separation within four hours of exposure to opposing AHL and arabinose gradients. By modulating the burden strength balance between coupled plasmids through a ribosome binding site (RBS) library, we characterize the tunability and inherent limits of this spatial patterning behavior. Phenotypic separation persists well beyond the period of active inducer exposure, indicating a population-level spatial memory encoded in copy number inheritance rather than sustained transcriptional input. A stochastic computational model recapitulates the observed patterning dynamics and confirms that copy number competition alone is sufficient to generate stable spatial organization without additional regulatory circuitry.

2.2 Introduction

Having colonized every conceivable niche on Earth, from human tumors to deep-sea vents, microorganisms have evolved diverse strategies to adapt to ever-changing environments. Phenotypic heterogeneity stands out as a pivotal mechanism, allowing genetically identical microbes to exhibit diverse phenotypes and enhance survival across various conditions[34, 35]. This adaptability manifests in microbial behaviors such as division of labor in biofilm formation or bet-hedging persistence to endure antibiotic treatments[34, 36, 37, 38]. From a theoretical standpoint, some molecular heterogeneity is expected. Genetic expression, governed by a limited number of molecules, results in fluctuations in the molecular composition of individual cells within a population[39, 40]. While this is intrinsic to any molecular mechanism, microbial genomes have strategically evolved to harness and modulate this molecular stochasticity. This is evidenced in organisms like *Escherichia coli* and *Saccharomyces cerevisiae*, where conserved and essential genes exhibit drastically reduced expression variation compared to metabolic and stress response genes[41, 42, 43]. Given the various mechanisms that underlie and regulate phenotypic heterogeneity, such as autoregulation, aging, circadian rhythms, and cell-cell interactions, this versatile strategy is seen not just as a survival tool in nature but also as a promising avenue for crafting robust and adaptive synthetic biological systems[44].

Recent research has pioneered the concept of plasmid copy number coupling in synthetic multi-plasmid systems. Tang and Liu first showed the use of such systems to stably record environmental events by controlling output plasmid ratio[29]. Later works employed dynamic copy number response of coupled plasmids for adaptation to specific environments, in one case directing reinforcement learning within a microbial population and in the other allowing burden reduction of synthetic constructs[32, 31]. Specifically, Kumar et al. showed that copy number flexibility in coupled plasmid systems allows populations to minimize encoded metabolic and other cellular burdens as a function of environment[31]. Bacterial cells housing plasmids sustain them at a specific copy number, steered by the autoregulation of its origin of replication. In

synthetic biology, orthogonal origins of replication are typically employed when integrating multiple plasmids into a cell, a necessary approach for stable maintenance of copy number for each construct. However, when identical origins of replication are used across different constructs, it was observed that engineered bacterial populations could dynamically adjust each plasmid's copy number in response to environmental condition. This deliberate induction of heterogeneity in the copy number of independent constructs sets the stage for bet-hedging during environmental fluxes where certain copy number ratios become advantageous. Termed "plasmid coupling," this mechanism enables bacterial populations to exploit phenotypic heterogeneity in ways that echo the natural tactics employed by microbes in variable environments[45].

To date, much of synthetic biology research operates under the assumption of "well-mixed" conditions. To prepare engineered populations for dynamic interaction with complex, non-homogeneous environments there is a need for both quantitative measurement and model-driven optimization of phenotypically variable populations in a multi-dimensional context. In this study we build a framework for simulation and testing of the spatiotemporal dynamics of plasmid-coupled strains within controlled 2D environments. A custom microfluidic platform allows continuous monitoring of bacterial proliferation across an adjustable gradient of inducers, while a stochastic computational model simulates the hypothesized spatial separation of phenotypes and provides a theoretical framework that supports the empirical observations. The combined experimental and computational results reveal pronounced phenotypic divisions in bacterial populations exposed to environmental inducer gradients, demonstrating that plasmid coupling can translate a chemical gradient into organized population structure without additional regulatory circuitry. This approach allows for environmental genetic modulation, bypassing the need for sense-and-respond circuits and thereby emulating the phenotypic plasticity observed in natural microbial communities.

2.3 Results and Discussion

2.3.1 Microfluidic Device for Plasmid Copy Number Control

Previous work on plasmid copy number regulation has successfully created small-molecule inducible copy number and mutated copy number variants[46, 26]. Recently, single strains carrying coupled plasmid systems have been developed which are capable of copy number-mediated differentiation and thereby population adaptation[31, 47]. The single strain contains two distinct plasmids with shared replication machinery coupling their copy numbers and generating a new source of heterogeneity. The above work with ColE1 plasmids has shown that due to shared replication inhibition, two distinct ColE1 constructs will share a total copy number but have a flexible distribution of each plasmid. Plasmid copy number can be visualized by a constitutively expressed unique fluorescent marker per construct where the fluorescence ratio represents the overall plasmid distribution. Here, we employed strains containing negative environmental burden in the form of induced production of protein phi X-174 (E-Lysis) which disrupts membrane integrity leading to a halt in ATP production and eventually lysis in gram-negative bacteria[48, 14] (Fig. 2.1a). Each plasmid in the coupled system has a unique environmental lysis inducer, either N-acylated-l-homoserine lactones (AHL) or arabinose, plus a unique reporter, either GFP or RFP, respectively. This coupled plasmid system with negative environmental feedback was kindly donated from Kumar et al. (2023) and served as a model system for testing bacterial self-adaptation to environmental conditions across spatial gradients. Figure 2.1b demonstrates the hypothesized spatial phenotypic plasticity with a coupled plasmid system compared to uniform expression expected from traditional compatible plasmids.

We developed a multi-dimensional microfluidic device capable of producing and maintaining superimposed continuous gradients of small molecules across a bacterial cultivation chamber. This is achieved by connecting two flowing channels, each carrying a small molecule, with a bacterial trap of 1 micron in height for 2-D microscopy of a monolayer of cells. This device allows us to superimpose opposing gradients of AHL and arabinose to enable spatial

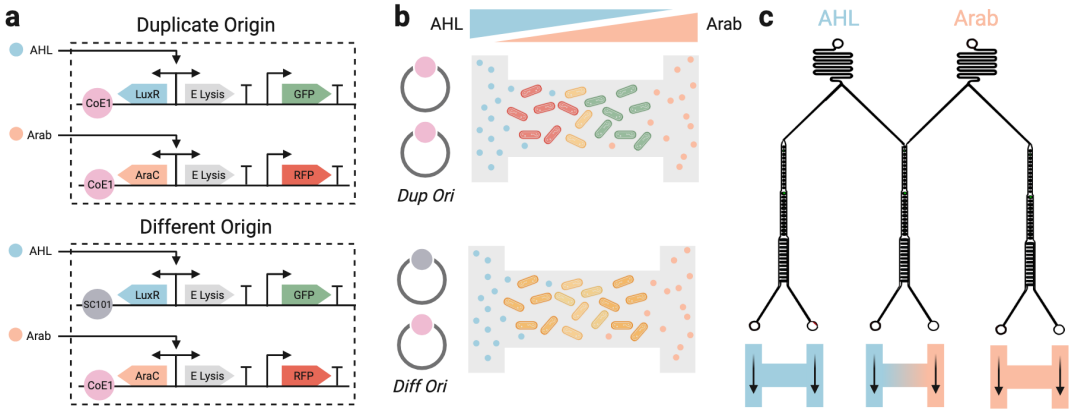


Figure 2.1. Depiction of the hypothesized spatial distribution of the coupled plasmid system. **a** Overview of dual plasmid genetic circuitry where either AHL or arabinose induces cellular lysis. In the duplicate origin system, both plasmids have the ColE1 origin of replication while in the different origin system one plasmid has SC101 and the other has ColE1. **b** Representation of expected phenotype distribution across trap of opposing AHL and arabinose gradients. **c** Layout of the microfluidic device with continuous cell cultivation chambers of 50 µm, 100 µm, and 250 µm in either inducer or a gradient of the two.

patterning of the environmentally-responsive coupled plasmid strain (Fig. 2.1b). When both inlet sources have equal flow rates a continuous steady-state gradient of environmental inducers is generated across the cell chamber. The device also carries multiple trap lengths of 50, 100, or 250 microns to probe different gradient spans based on the inducer's diffusivity[49]. Upholding this basic design principle two distinct chip variations were constructed. In the first design, each inlet channel immediately flanks to either side and fully feeds an entire trap. This creates three unique cell cultivation chamber conditions from the same inlet media sources of only media 1, only media 2, and gradient from media 1 to media 2 (Fig. 2.1c). The second design has two fully independent gradient-generating microfluidic systems within a single chip allowing for two device technical replicates per experiment (Fig. 2.1b). To further optimize our experimental setup and anticipate potential outcomes, it is vital to generate a computational framework that can predict the behavior of bacterial populations under our proposed coupled plasmid system.

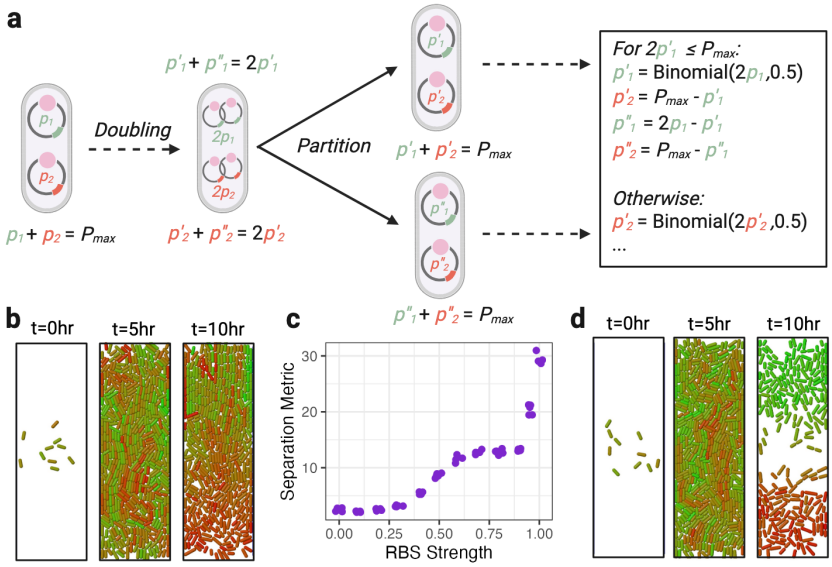


Figure 2.2. Computational model for spatial distribution of plasmid coupling. **a** Schematic diagram of binomial plasmid partitioning during cell division, restricted to a total copy number of $p_{\max}$. **b** Snapshots of cell chamber during simulation of weak arabinose RBS relative to AHL RBS. **c** Effect of arabinose RBS strength on final trap separation ($n = 5$). **d** Snapshots of cell chamber during simulation of balanced arabinose and AHL RBS strengths.

2.3.2 Modeling of Copy-Number Based Patterning

To model the spatiotemporal dynamics of bacterial colonies in our microfluidic devices, we used an agent-based approach. There have been a number of mechanistic agent-based models of cellular populations described in the literature that share the same general methodology[50, 51, 52, 53, 54]. Briefly, individual cells are represented as spherocylinders which increase in length based on their growth rate and divide once reaching a set length. Cells repel contact with each other and the chamber walls. Each cell also carries two variables representing the number of plasmids of type 1 and 2. These plasmid numbers are updated on cell division by doubling prior to binomial partitioning between the two daughter cells, as depicted in Figure 2.2a. Thus, daughter cells retain memory of the plasmid distribution of the mother cell, however gradually this memory is lost, and the distribution returns to the equilibrium.

To model the experiments with plasmid separation by external signals, we allowed the cell colony in our simulations to grow for 5 hours to fill up the chamber, after which we applied

two different chemical inducers (AHL and arabinose) on two opposing sides of the chamber. We assumed that the concentration of each inducer decays inward exponentially, according to the distributions

$$\mathrm{AHL}(y) = \mathrm{AHL}_0 \exp[\alpha(y - L_y/2)] \tag{2.1}$$

$$\mathrm{Ara}(y) = \mathrm{Ara}_0 \exp[-\alpha(y + L_y/2)] \tag{2.2}$$

Since experimentally each inducer activates a lysis gene on the plasmid that carries the corresponding promoter, the probability of a cell lysing depends on both the local concentration of the inducer and the number of its cognate plasmids. We remove a cell i from the colony if either of the two conditions is fulfilled: $\mathrm{AHL}(y^i)p_1^i > \varepsilon$ or $\mathrm{Ara}(y^i)p_2^i > \varepsilon$. Here y_i is the location of cell i, $p_{1,2}^i$ are the copy numbers of plasmids of both types in that cell, and ε is a nominal threshold value. Sample snapshots of a typical simulation illustrate a quick separation of "red" and "green" cells inside the computational domain (Fig. 2.2d). The distributions of p_1 and p_2 quickly become bimodal, and the average numbers of plasmids in the top and bottom halves of the computation domain strongly diverge (Fig. 2.6a–b). We further simulate the dynamics of a population under the spatially uniform presence of both inducers (Fig. 2.9). In this case, increased lysis pressure selects for cells with intermediate plasmid ratios and thereby stabilizes population copy number.

To probe the robustness of our model, we explored the effect of an imbalance in inducer sensitivity between the plasmids. Experimentally, this would correspond to mutating (and weakening) the RBS sequence at one of the plasmid's lysis gene promoters. In our computer simulation, we modified the second condition for cell lysis by $RBS \cdot \mathrm{Ara}(y^i)p_2^i > \varepsilon$ with the parameter $RBS < 1$. For a weak $RBS = 0.1$, red-shifted cells are less prone to lysis and dominate throughout the chamber, however this domination gradually weakens away from the lower open side (Fig. 2.2b). Unlike the case of balanced lysis, the average copy numbers of plasmids in top and bottom halves show much weaker separation. We quantified this separation by the separation

parameter S computed as follows:

$$S = \frac{\langle \langle p_2 \rangle_t / \langle p_1 \rangle_t \rangle_t}{\langle \langle p_2 \rangle_b / \langle p_1 \rangle_b \rangle_t}$$

where $\langle p_{1,2} \rangle_{t,b}$ are the average copy numbers of plasmids $p_{1,2}$ in top and bottom halves, respectively, and the outside brackets indicate averaging over time after the steady state has been reached. Figure 2.2c shows a rather non-trivial behavior of this separation parameter as we varied the RBS parameter. For small *RBS*, when one plasmid dominates, this parameter is small (close to 2 in our simulations). It then grows gradually with *RBS* and reaches a plateau of about $S = 15$ between $RBS = 0.6$–0.9 and then grows rapidly at very large *RBS*, eventually reaching a large value of approximately 30 for $RBS = 1$. Our computational modeling provides insights into the anticipated spatiotemporal patterns in our experimental setup, emphasizing the complex interplay between induction strength and population-level behavior.

2.3.3 Phenotypic Patterning from Environmental Fluctuations

Our preliminary spatial modeling of the coupled plasmid system underscored the importance of balancing RBS strength across both plasmids to achieve phenotypic separation. Therefore, we investigated three unique coupled plasmid *E. coli* MG1655 strains with variable RBS sequences upstream of arabinose-inducible lysis (Fig. 2.3a). After a lysis screening of RBS mutants, we selected strains here named strains 1, 2, and 3, representing weak, medium, and strong RBS lysis. Using microfluidics, as described in the methods, exponential phase cells were loaded at low density into cell chambers and exposed to superimposed opposing gradients from 200 μM AHL and 0.02% arabinose. The cells were then able to colonize and adapt to this heterogeneous environment while being monitored through fluorescent microscopy.

For dOri_S1, during the first 3 hours of growth, cells appeared to follow their initial seeding pattern, highlighted by the mixed populations of RFP-shifted and GFP-shifted cells representing high arabinose-induced plasmid and high AHL-induced plasmid copy number,

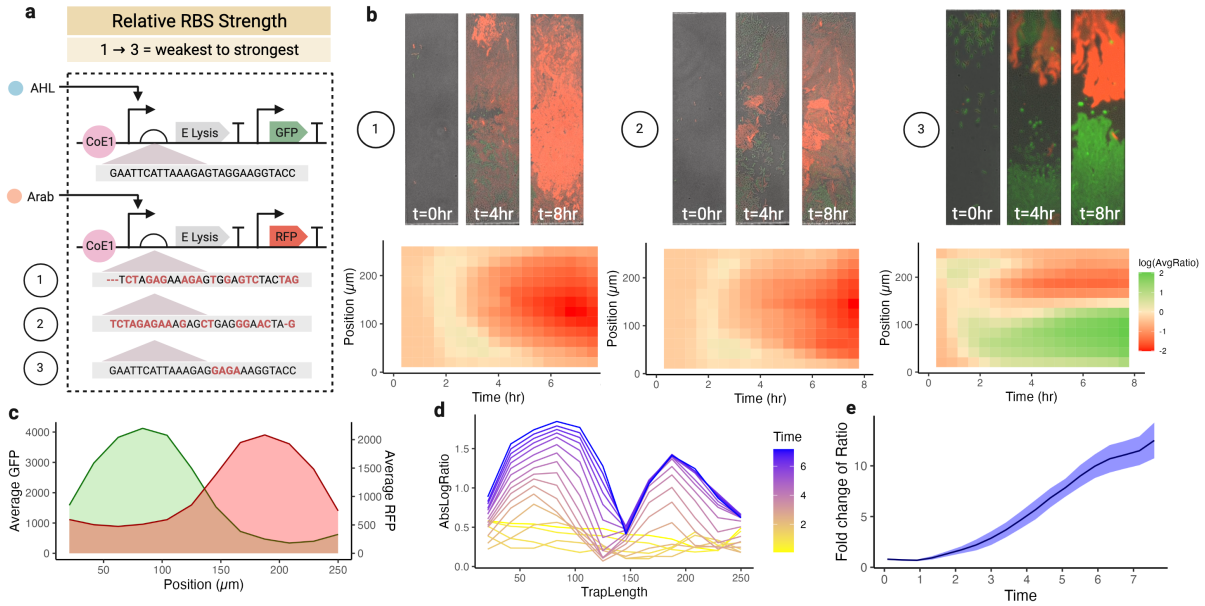


Figure 2.3. Copy Number Based Phenotype Separation. **a** Sequencing of mutations generated in RBS library and relative strength. **b** Snapshots from microfluidic runs on RBS library showcasing observed phenotype separation and heat maps summarizing fluorescent localization over time ($n = 12$). **c** Average GFP and RFP fluorescence across a single trap at 4 hours ($n = 12$). **d** Ratio of fluorescent proteins across trap length over time. **e** Separation metric across all 12 traps over 8 hours.

respectively (Fig. 2.3b). However, starting at 4 hours and continuing for the remainder of the experiment, the entire cell trap was taken over by high RFP expressing cells indicating a preference for high arabinose plasmid copy number independent of the gradient (Fig. 2.3b). This indicates that the weak lysis induction allows RFP-shifted cells to thrive even at the highest arabinose concentration. Due to this advantage in fitness, they quickly overgrow and displace GFP-shifted cells from the initial mixed heterogeneous population.

dOri_S2 behaved similarly to dOri_S1 with an initially mixed population for the first 3 hours followed by the majority of cells having high arabinose-induced copy number ratio and low AHL-induced copy number ratio. Despite both strains preferring high arabinose-induced copy number, dOri_S2's magnitude of red fluorescence is lower than dOri_S1, indicating improvement toward balanced plasmid coupling (Fig. 2.3b). For dOri_S3, a notable separation between plasmid copy preference was achieved within the 250 μm cell chambers, indicated by clear differential localization of green and red fluorescence to opposing trap ends after 4 hours, and becoming

starker thereafter (Fig. 2.3c,d,e). In chamber sizes of 50 μm and 100 μm, the higher inducer pressure led dOri_S3 to follow initial seeding patterns as opposed to environmental selection, suggesting a spatial limit in phenotypic separation that might be expanded with fine-tuning of inducer gradient (Fig. 4.3).

Interestingly, as the cells populated the trap we observed an illusion of population swarming along the trap, likely due to balanced growth and death rates at the beginning of each experiment. In addition, a boundary layer lacking cell growth emerged in the middle of the cell trap completely dividing the two subpopulations of RFP-shifted and GFP-shifted cells (Movie 1). This behavior, observed over a prolonged period, highlights the influence of environmental gradients on phenotypic outcomes among genetically identical cells thanks to plasmid copy number heterogeneity. In addition to lysis as the main driving force for preferential plasmid separation, secondary effects of specific circuit induction could lead to reduced growth rate or plasmid replication of cells carrying larger numbers of induced plasmids. This added feedback could enhance spatial separation in non-trivial ways and also may operate at slower time scales[55]. Strikingly, this separation mimics the effects of phenotypic plasticity, where drastic phenotypic differences can emerge from the same genetic background based on external cues.

For controls, dOri_S3 was also run in our microfluidic device containing cell cultivation chambers with single uniform inducer presence. dOri_S3 followed the expected patterning with dominant arabinose-induced copy number ratio in only 200 μm AHL conditions and dominant AHL-induced copy number ratio in only 0.02% arabinose conditions (Fig. 2.2, Movie S1/S2). These results align with the findings of Kumar et al. and highlight that selective pressure from a single homogeneous inducer causes rapid lysis of subpopulations carrying high copy number of the induced plasmid and thereby leads to decline of this plasmid in the overall population[31]. A fourth strain with different origins of replication on each plasmid served as a comparison against traditional compatible plasmids. Without plasmid coupling the microfluidic experiments showed dOri_ctrl was unable to adapt to the environmental cues and large-scale cell death occurred across

all cell traps (Fig. 4.4).

2.3.4 Long-Term Genetic Memory of Population Phenotype

To further probe the longevity of plasmid-mediated phenotypic segregation, additional microfluidic experiments with inducer removal were conducted on dOri_S3. As anticipated from our prior experiments, all cell traps showed complete phenotype separation in 4 hours. After 12 hours, all inducers were removed from half of the cell traps, releasing inducer-mediated environmental pressure. Thereafter, the population still maintained a clear separation for several hours until GFP-shifted cells began to slowly take over the cultivation chamber (Fig. 2.4c, Movie 4). This was also the case for traps with sustained long-term inducer cues. This slow trend towards GFP-shifted dominance sheds light on the intricacies of plasmid-mediated phenotypic dynamics. While the external inducers play a crucial role in driving phenotypic differentiation in the initial stages, notably within the first 4–8 hours, the system seems to transition towards a new equilibrium favoring the green phenotype independent of these cues. A plausible explanation for this shift might lie in the evolutionary and cellular mechanics at play. If the AHL-induced plasmid imparts a slightly reduced burden on the cellular machinery than the arabinose-induced counterpart, cells harboring this GFP-expressing plasmid could exhibit a fitness advantage over time. Additionally, following inducer removal, leaky expression from the pBAD promoter or biases in plasmid replication could result in the apparent dominance of GFP-shifted cells. Concurrently, sporadic mutations impacting lysis induction differently could also accelerate this green-dominant trend. This result illustrates the population's adaptive strategy to optimize growth and sustainability, despite the constraints of earlier external pressures.

To supplement these findings, we used our computational model to simulate the relaxation from a plasmid-separated regime after inducer removal. Similar to experimental runs, the simulations showed maintenance of phenotypic separation for the first few hours after the removal of inducers. However, unlike our observations in microfluidics, the simulated population returned to a mixed heterogeneous state soon after. Based on our model, we hypothesized

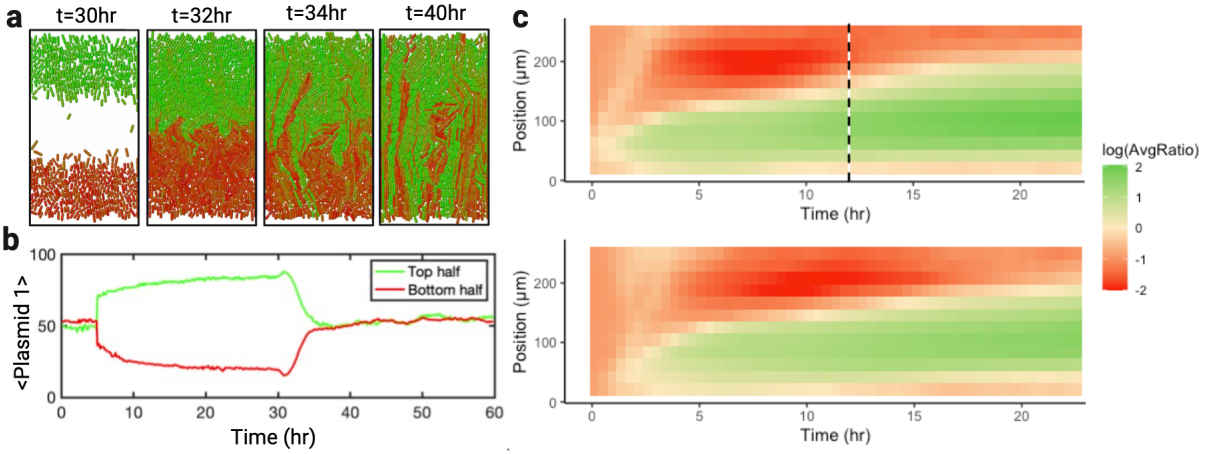


Figure 2.4. Copy Number Based Memory Post Induction. **a** Simulation results highlighting the expected relaxation after media swapping. **b** Quantification of Plasmid 1 copy number in the top and bottom half of the simulation trap. **c** Fluorescent quantification across microfluidic run where dashed line indicates removal of inducers from media ($n = 12$).

that this memory effect should be more pronounced for high copy number $p_{\max}$ since a larger pool of plasmids reduces stochastic effects and slows down the stochastic copy-number drift (Fig. 2.8). Surprisingly, we did not observe a strong memory effect for all values of copy numbers tested, presumably because the red-shifted and green-shifted cells on the edges of the chamber get quickly pushed away by growing cells in the middle of the chamber that have approximately equal values of p_1 and p_2. Moreover, there was not a slow takeover of green-shifted cells in the simulations as seen experimentally, presumably due to the precisely equal plasmid burden in the model and a lack of other natural factors such as spontaneous mutations or physical interactions between biofilms and inducer removal rates present in the complexity of the microfluidic experiments. While the computational model offers insightful predictions, the discrepancies observed with experimental results highlight the intricate complexities of biological systems. Our findings emphasize the essential interplay between genetic factors, molecular stochasticity, and environmental influences, underscoring the need for a synergistic approach between modeling and empirical studies in understanding microbial adaptability and its engineering for synthetic applications.

2.4 Discussion

Generating spatial patterns in engineered communities has been of great interest to synthetic biologists hoping to gain insight into the morphogenesis of natural systems[56]. To date, gene-regulatory networks carrying incoherent feedforward loops have been a classical method for generating phenotypic patterns in response to simple environmental gradients[57, 58]. Here we show how the use of plasmid coupling for the generation of population phenotypic diversity enables an initially clonal population to respond to non-homogeneous external conditions. Unlike traditional sense-and-respond circuitry, we demonstrate the use of cellular burden as a driving force for spatial differentiation by introducing copy number heterogeneity. Fitness-based population response allows for dynamic adaptation to fluctuating conditions on timescales distinct from transcriptional circuits: phenotypic diversity allows immediate survival of subpopulations in the face of extreme lytic pressure, while plasmid inheritance creates long-term memory of spatial distribution in the absence of selection. The RBS library results further underscore that this spatial behavior depends on both genetic and environmental parameters in concert: neither the duplicate origin architecture alone nor the gradient alone was sufficient to produce stable patterning. What the microfluidic platform reveals is that this capacity for spatial differentiation was always latent in the coupled plasmid design; well-mixed batch culture simply had no way to express it.

This observation reframes how we interpret the result. The gradient device did not engineer new behavior into the population ; it changed the lens through which existing behavior became visible. In standard culture conditions, environmental homogeneity averages away the phenotypic heterogeneity that copy number variation continuously generates, leaving only a population mean that masks the underlying diversity. Imposing a spatial gradient breaks that averaging, allowing fitness-based selection to act on the pre-existing distribution and organize it into functional structure. This distinction has practical implications beyond the specific system studied here. It suggests that other synthetic circuits harboring latent functional diversity may

similarly be unlocked by moving from well-mixed to spatially structured environments, and that the environment itself is an underutilized regulatory parameter for synthetic circuit design. The chapters that follow develop this idea directly, using physiologically relevant environments to expose and exploit circuit behaviors that homogeneous *in vitro* conditions cannot access.

2.5 Materials and Methods

2.5.1 Microfluidics and Microscopy

The microfluidics techniques are similar to those described previously by our group[59]. Our microfluidic devices were constructed from PDMS (polydimethylsiloxane), which was molded and baked on a silicon wafer with micron-scale features formed by cross-linked photoresist. After about 12 hours of baking at 65°C, the PDMS was peeled from the wafer and features were transferred onto the PDMS. Individual devices were then cut out of the baked PDMS and holes were punctured in the devices to allow for the connection of fluid lines. The devices were then bonded onto coverslips and placed on a microscope stage for cell loading and imaging. Before each experiment, the devices were left for 45 min in a vacuum chamber. After taking the device out of the vacuum chamber, 10 μL droplets of cells were positioned on the outlets. Similarly, 10 μL droplets of sterile media were placed on the inlet openings. The media used contained LB and antibiotics of appropriate concentration along with either 200 nM of AHL or 0.02% of arabinose sugar. In every case, 0.075% Tween 20 was added to the media to prevent cells from sticking to the PDMS walls. After all the chip features were wetted, fluid lines were connected to the devices from various syringes supplying media or acting as waste reservoirs. The flow direction in the device was controlled by changing the relative heights between the relevant syringes resulting in hydrostatic pressure driven flow. Images were acquired using a Nikon Ti-2 microscope. The microscope was housed in a plexiglass incubation chamber maintained at 37°C by a heating unit. Phase-contrast images were taken at 20x magnification. For mCherry the fluorescence exposure time was 50 ms at 50% intensity while for GFP the

fluorescence exposure time was 40 ms at 50% intensity. Images were taken every 10 min for each experiment.

2.5.2 Agent-Based Computational Model

In our simulations we used the agent-based code developed in Warren et al.[54] and adapted it for our purposes. Each individual bacterial cell is modeled as an elongating and dividing spherocylinder. The cell increases its length exponentially with a nominal growth rate $\gamma = 1.36\ \mathrm{h}^{-1}$ that corresponds to a cell doubling time of 0.5 hours. When the cell length reaches a certain pre-determined value $l_{\max}$, the cell divides into two collinear daughter cells of lengths $l_{\max}/2$ touching by their newly formed poles. The cells in our case are non-motile, so they only move when they experience external forces, typically from neighboring cells. Whenever two cells overlap, they experience repulsion forces at the point of contact that scale with the overlapping distance d according to a Hertzian law $F \sim d^{3/2}$. They also experience repulsive forces from solid walls and friction forces from the bottom or top of the chamber and the surrounding fluid. Since cells are very small and move slowly, a typical Reynolds number for cellular motion is very small, and the Newton law describing cell motion can be simplified to ignore inertia effects. Thus the cell velocity is simply proportional to the vector sum of all forces and the cell angular velocity is proportional to the sum of all momenta.

For our simulations, we confined all spherocylinders to a monolayer in the x,y plane to reflect the design of our microfluidic chambers. The cells were growing in a rectangular domain of width L_x and length L_y. As in experiment, the walls at $x = \pm L_x/2$ were solid, and the walls at $y = \pm L_y/2$ were open, so that as soon as the center of mass of a cell crosses those virtual walls, the cell is immediately removed from the colony. We endowed all cells with two internal variables p_1 and p_2 for the copy numbers of plasmids of type 1 and 2, respectively. We assume that the total number of both plasmids in every cell is fixed, $p_1 + p_2 = p_{\max}$. We also assume that the plasmid copy numbers do not change during the life cycle of individual cells. However, at cell division, daughter cells get random numbers of plasmids 1 and 2 in approximate proportion

to their fraction in the mother cells that add up to $p_{\max}$. We perform this partition by splitting the cell division event into two sub-steps: in the first, the number of plasmids in the cell doubles to $2p_1 + 2p_2 = 2p_{\max}$, and then each plasmid is placed randomly into one of the two daughter cells (Fig. 2.2a).

2.5.3 Molecular Cloning and Cell Culture

All plasmids were transformed into *E. coli* strain MG1655. Strains were cultured in lysogeny broth (LB) with 20 μg mL^{-1} of chloramphenicol and 60 μg mL^{-1} of spectinomycin in a 37°C shaker. Primer sequencing was conducted on all plasmids within the study. Sequencing identified the arabinose RBS mutations and the AHL RBS described in Figure 2.3a. For microfluidic experiments, the appropriate *E. coli* strains were seeded from a −80°C glycerol stock into 1 mL LB with appropriate concentrations added and incubated at 37°C. Samples were monitored for an OD of 0.1 every 20 minutes and measured at OD_{600} using a DU 740 Life Science UV/vis spectrophotometer.

2.5.4 Microfluidic Chip Fabrication

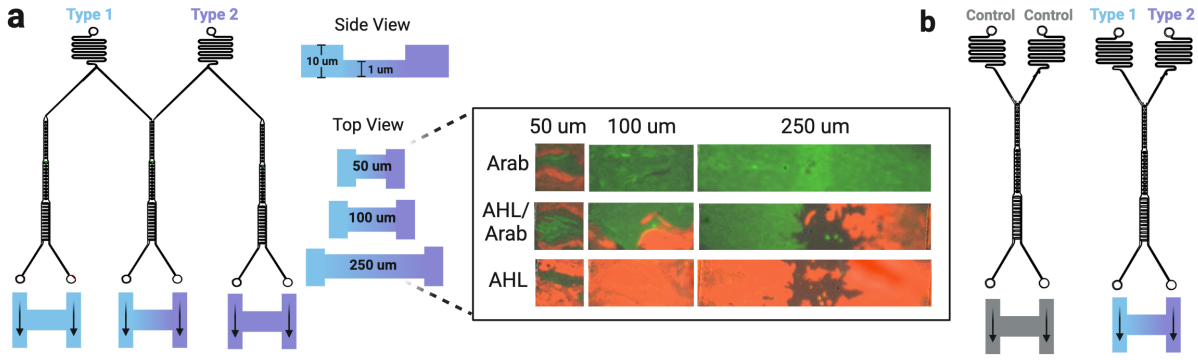
High contrast, epoxy-based photoresist SU-8 2000.5 is pipetted on top of a 4-inch silicon wafer substrate which is subsequently spun at 400 RPM for 2 minutes to achieve the first layer height of approximately 1 μm. It is then soft-baked for one minute at 95°C. This photoresist-coated wafer is exposed to UV light for 7 seconds while in contact with a mylar ink photomask, exposing, and therefore cross-linking, only the geometries left translucent in the mask design. The wafer is again baked at 95°C for 1.5 minutes and a development process takes place for one minute. This results in the approximately 1 μm layer that will come to contain the traps of this device design. This process is repeated to make the second layer which forms the main channels of the device. For this approximately 10 μm layer, SU-8 2007 is applied to the wafer and spun at 1500 RPM for one minute. It is soft-baked for 2.5 minutes at 95°C and exposed to UV light from under the photomask for 10 seconds. Post-exposure, the wafer is baked at 95°C for 3.5 minutes

and developed for 2.5 minutes.

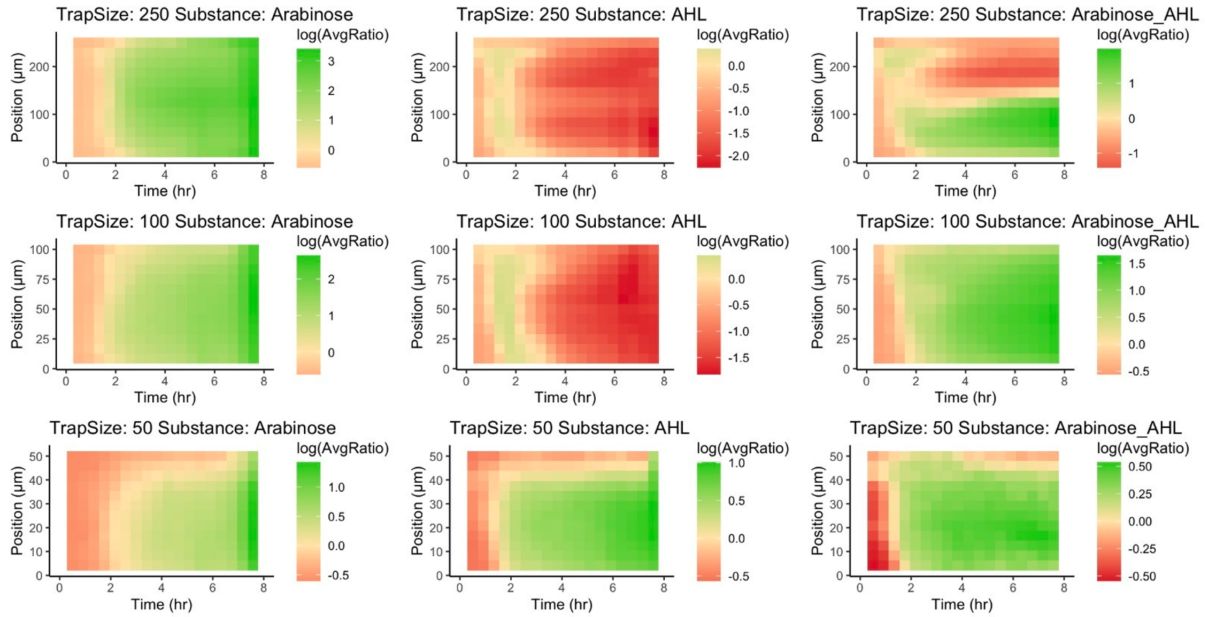
2.5.5 Data Analysis

Fluorescence intensity profiles were obtained by analyzing frames from the fluorescent channel recorded on the Nikon Ti-2. The mean fluorescence intensity was calculated by first identifying the trap bounds and parsing them into 12 equivalent subsections. The mean value of both the RFP and GFP fluorescent channels were calculated with `np.mean()` for each subsection and normalized with a trap image prior to loaded cells. Log of the GFP/RFP ratio was plotted following normalization for visualization within heatmaps and calculation of the separation metric S, defined previously.

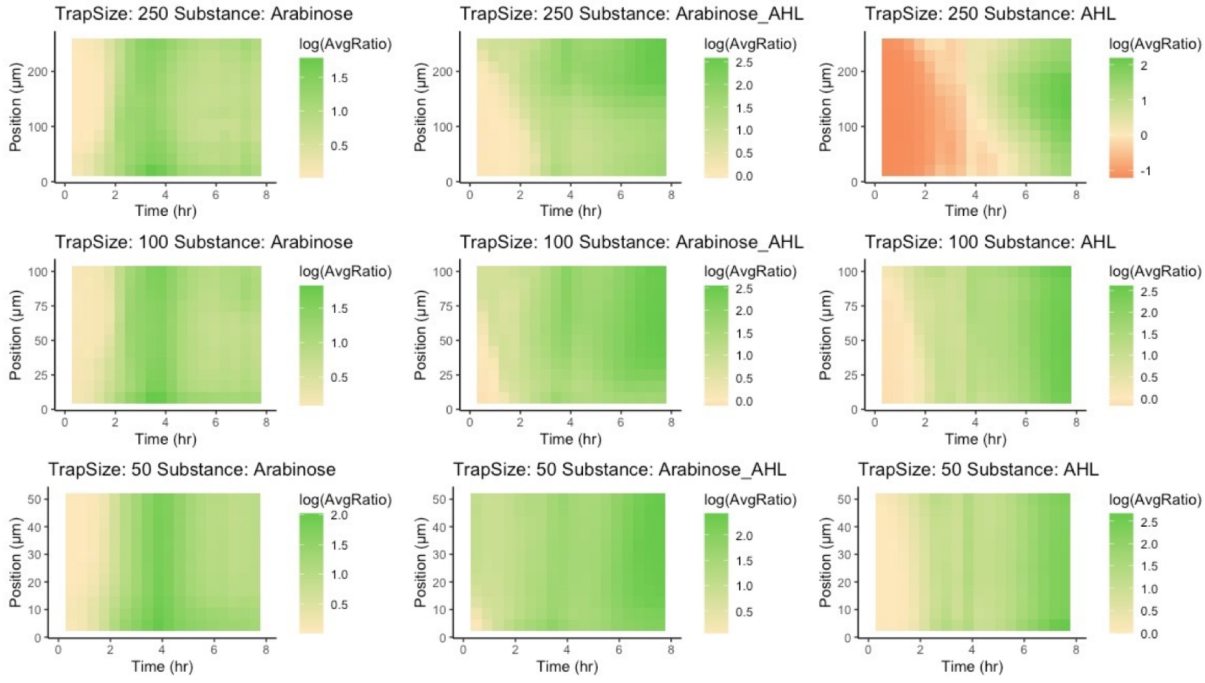
2.6 Supplemental Figures



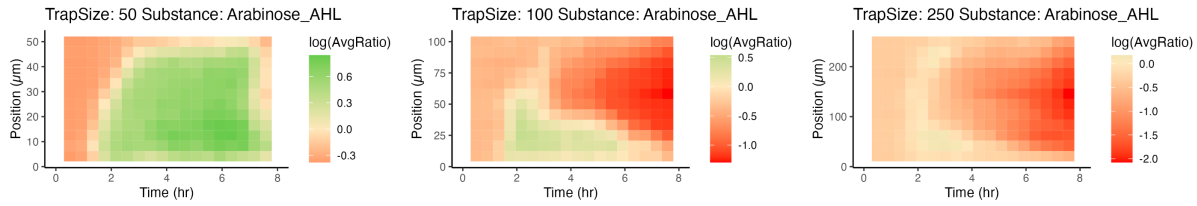
Supplemental Figure 2.1. Microfluidic device design details. **a** Layout of channel heights, cell trap widths, and media concentrations with example experimental results. **b** Layout of second chip design with independent media reservoirs and media chambers allowing two device technical replicates per experiment.



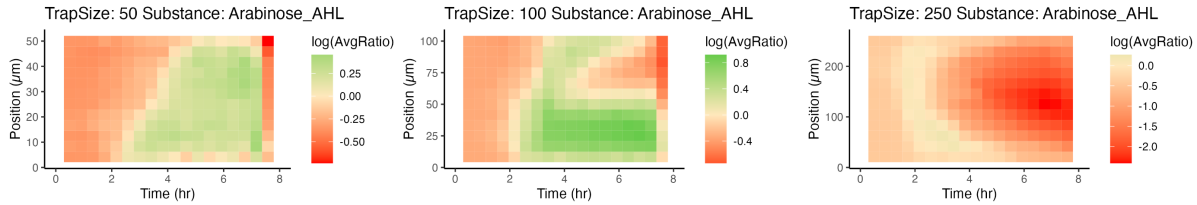
Supplemental Figure 2.2. Fluorescent quantification of dOri_S3 over time for every trap size and media condition, including single-inducer controls.



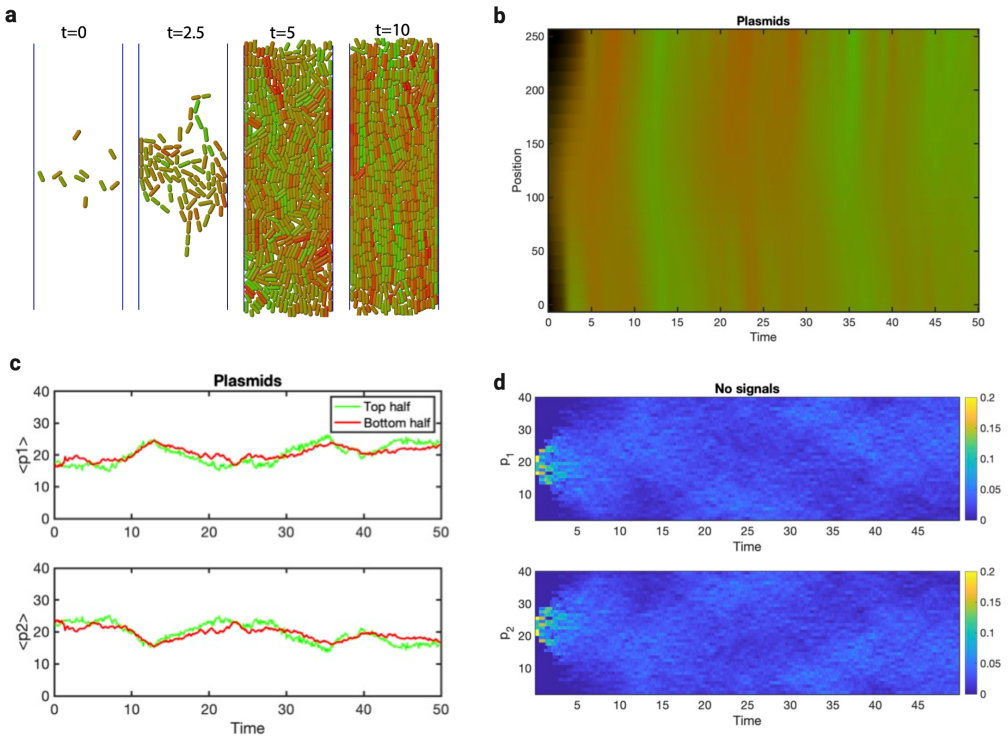
Supplemental Figure 2.3. Fluorescent quantification of the control strain with different origins of replication on each plasmid over time for every trap size and media condition. Without plasmid coupling, large-scale cell death occurred across all cell traps.



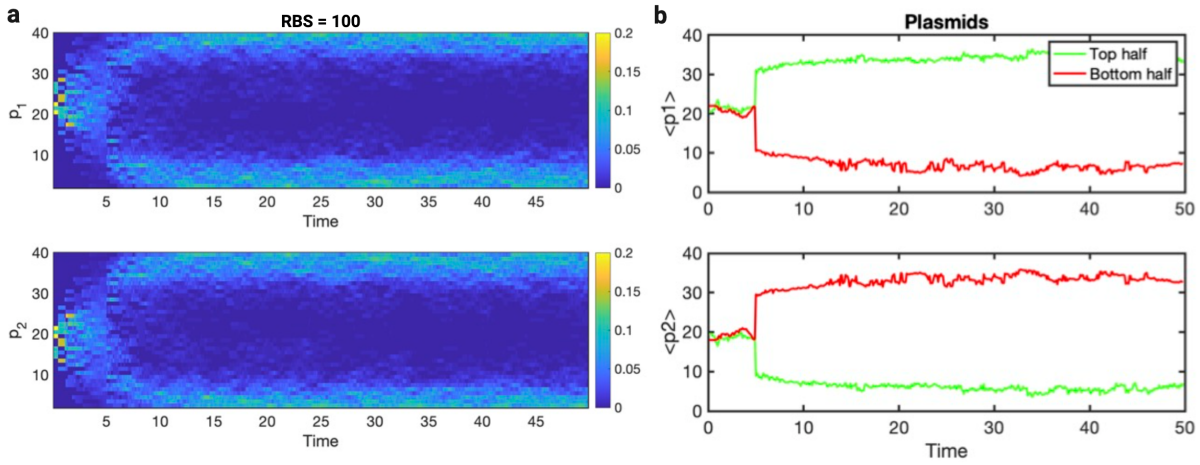
Supplemental Figure 2.4. Fluorescent quantification of dOri_S1 over time for every trap size and mixed-media condition.



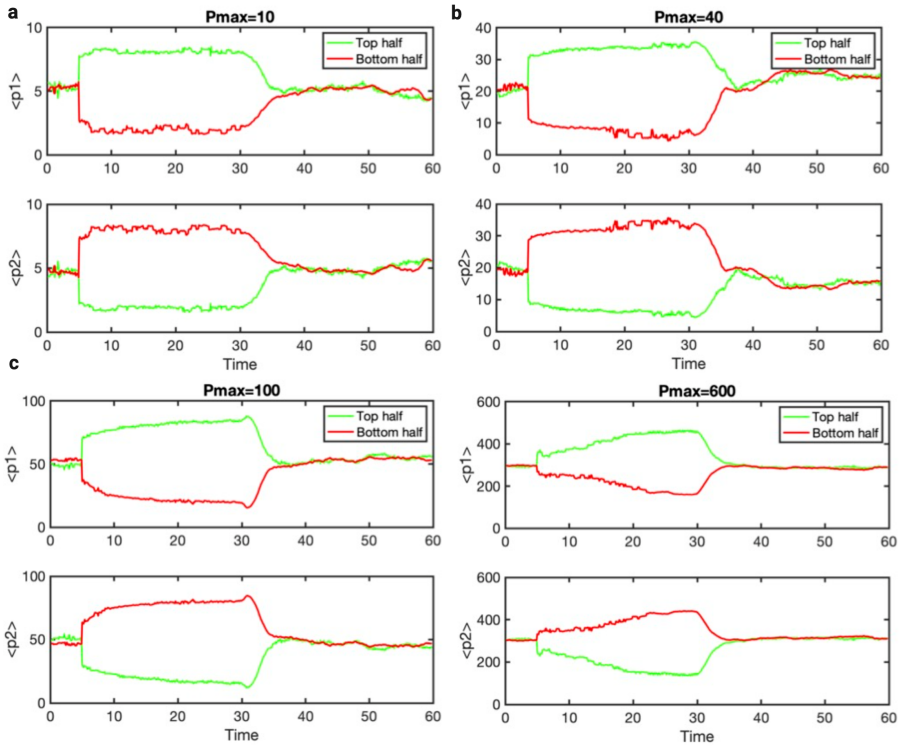
Supplemental Figure 2.5. Fluorescent quantification of dOri_S2 over time for every trap size and mixed-media condition.



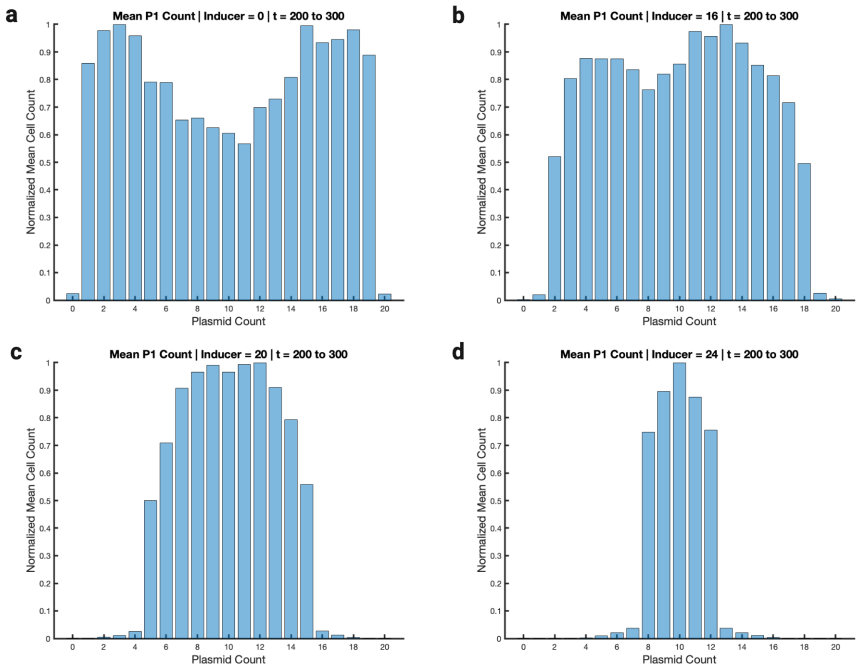
Supplemental Figure 2.6. Simulation with no environmental inducer. **a** Video time points of phenotype distribution in cell trap. **b** Heat maps showing random phenotype distribution throughout entire 50-hour simulation. **c** Plasmid copy number quantification in each half of cell trap. **d** Distribution of plasmid copy number over time.



Supplemental Figure 2.7. Simulation with sustained environmental inducers. **a** Distribution of plasmid copy number over time. **b** Quantification of plasmid copy numbers in each half of cell trap.



Supplemental Figure 2.8. Plasmid quantification over time with inducer removal at varying maximum plasmid capacities. **a** $p_{\max} = 10$. **b** $p_{\max} = 40$. **c** $p_{\max} = 100$. **d** $p_{\max} = 600$.



Supplemental Figure 2.9. Histograms depicting simulated frequency of p_1 plasmid counts for a colony under various strengths of dual, uniform inducers. Inducer is turned on at $t = 100$ and data collected from $t = 200$ to 300. **a** No inducer. **b** Inducer variable at 16. **c** Inducer variable at 20. **d** Inducer variable at 24.

Chapter 2, in full, is a reprint of the material as it appears in Steppe, P., Rey-Bedón, C.*, Kumar, S., Forrest, E., Van Der Wagt, N., Tayal, A., Tsimring, L., and Hasty, J. Phenotypic Patterning through Copy Number Adaptation to Environmental Gradients. ACS Synthetic Biology (2024). The dissertation author was a primary investigator and co-first author of this paper.*

Chapter 3

Physiological Context Reshapes the Dynamics of Coupled Bacterial Circuits

3.1 Abstract

Engineered bacterial circuits are typically characterized in homogeneous liquid culture, yet their target environments, including solid tumors, the gut lumen, and inflamed tissues, impose gradients of oxygen, matrix mechanics, and cell density that fundamentally reshape circuit dynamics. Here, we use a modular tissue-scale testbed to interrogate how physiological context alters the behavior of therapeutic and diagnostic bacterial circuits. In a tumor microenvironment module, hypoxia extends the synchronized lysis circuit period from approximately five hours in standard microfluidic traps to approximately sixteen hours in collagen under oxygen limitation, approaching dynamics observed in murine tumor models, while extracellular matrix stiffness attenuates AHL-mediated quorum coupling across tissue-relevant distances. A co-culture module reveals that bacterial chassis and motility determine the spatial reach and timing of cancer cell killing independently of the genetic payload. In a gut lumen module, DNA biosensing activity varies spatially along oxygen and substrate gradients in ways not captured by batch culture assays. Across all modules, the testbed exposes circuit behaviors that are inaccessible to existing models and provides a physiologically grounded framework for resolving the mechanisms that govern engineered bacterial function at the point of therapeutic or diagnostic deployment.

3.2 Introduction

Engineered bacteria are at the forefront of living medicines, spanning applications from oncology to metabolic disorders[60, 61, 62, 11, 63]. For instance, engineered bacteria have been programmed to deliver anticancer drugs in tumors cyclically[64, 17], to detect circulating DNA mutations[65, 66, 67], and to colonize the gut microbiome to correct metabolic dysfunction[68, 69]. These applications have been streamlined by advances in gene circuit design, computational modeling, DNA synthesis, and assembly, driving a recent surge of proof-of-concept bacterial therapeutic and diagnostic studies in the literature[70, 71]. However, their predicted dynamics are mostly characterized in oversimplified *in vitro* formats, which manifests as either translational failure or a wide discrepancy with the dynamics observed *in vivo*[72, 8]. Despite the expansion in synthetic biology tools, the lack of a platform to modulate bacterial gene circuits in physiological contexts remains a major translational bottleneck for living medicines[73, 74, 75].

Century-old microbiology techniques still dominate the evaluation of engineered bacteria, where homogeneous batch cultures are tracked optically to infer population and gene-expression dynamics[76, 77]. In recent decades, microfluidic bacterial monolayers have aided synthetic biologists to analyze engineered bacteria at high-throughput single-cell resolution[78, 79, 80]. While foundational, these methods still fail to replicate the complex composition and architecture of host niches where bacterial medicines aim to be deployed[8, 11]. Simultaneously in disease modeling, microphysiological systems (MPS), also known as "organ-chips," offer a state-of-the-art approach to recapitulate complex human microenvironments *in vitro*[81, 82, 83, 84]. MPS technology has been used to model a variety of diseases and organ contexts, from tumor angiogenesis to liver metabolic syndrome to neurodegeneration[85, 86, 87]. Current organ-chips, however, mostly focus on mammalian cell culture and either exclude live bacteria or oversimplify their presence[88, 89, 90, 91]. Existing models rarely allow a controlled culture of engineered bacteria with human cells under physiological conditions, leaving a critical gap in our ability to test synthetic gene circuits in settings that mimic the targeted environments.

Here, we deploy a modular tissue-scale testbed to ask how physiological context reshapes the behavior of engineered bacterial circuits across therapeutic and diagnostic applications. We demonstrate the versatility of this resource through tumor and gut-like illustrative modules aligned with therapeutic and diagnostic applications. In a tumor microenvironment (TME) testbed, we show that *E. coli* carrying the synchronized lysis circuit (SLC) exhibit spatially patterned activation and drug release in response to hypoxia and quorum signals across a collagen matrix. We also developed a co-culture protocol in which engineered bacteria and cancer cells are grown in adjacent hydrogel sections, enabling direct observation of bacteria–tumor interactions and quantification of the diffusion range of a bacterially delivered cytotoxic protein while comparing a motile versus a non-motile SLC-carrying bacterial chassis. As a proof-of-concept for diagnostics, we deploy naturally competent *Acinetobacter baylyi* in a gut-mimicking testbed to detect cell-free DNA diffusing through a mucin-rich matrix. These testbeds allowed us to recapitulate dynamics observed *in vivo* and to further reveal emergent behaviors previously inaccessible in any model.

3.3 Results

Recapitulating the physicochemical architecture of a tissue requires more than growing cells in a dish; it demands independent control over chemical gradients, matrix mechanics, and cellular composition simultaneously and at physiologically relevant spatial scales. To achieve this, we designed a modular testbed with isolated yet diffusely coupled compartments[92]. An upper media flow chamber customizes the distribution of small molecules, while a lower chamber measuring 10 mm $\times$ 2 mm $\times$ 0.2 mm contains a hydrogel matrix housing engineered bacteria, along with any supportive mammalian cell types. A thin, porous membrane between chambers permits molecular diffusion and provides physical support, effectively simulating an epithelial or endothelial barrier interface (Fig. 3.1A). This architecture combines the classic dual-chamber coupling of MPS technology with modular gradient generators used in high-throughput bacterial

microfluidics (Fig. 3.1B,C). This modular testbed is highly flexible in composition and geometry, accommodating different gradient patterns, matrix formulations, and multicellular co-cultures, rapidly reconfiguring the platform to culture bacteria under various pathological niches of interest, such as tumor-like or gut-like settings (Fig. 3.1D). In this testbed, engineered bacteria grow as three-dimensional colonies under a custom combination of physiological signatures while high-resolution imaging captures bacterial dynamics in real time. Along with this resource, we provide an image analysis pipeline that outputs a stitched time-lapse sequence along with automatic quantification of individual colony growth and gene-expression dynamics throughout the entire length of the testbed (Fig. 3.1E). This pipeline requires no specialized image analysis expertise beyond standard Fiji and R installations, and all macros and scripts are provided as open-access resources to enable immediate adoption alongside the testbed design files.

3.3.1 Microfluidic Platform Design and Fabrication

A central contribution of this chapter is the design and fabrication of the modular testbed itself. Existing bacterial microfluidic platforms are optimized for monolayer culture at micron scale, while organ-chip systems are designed for mammalian cells and rarely accommodate live bacteria under controlled chemical gradients. Bridging these two paradigms required building a device from scratch: a three-layer PDMS architecture that couples a gradient-generating flow chamber to a hydrogel cell culture chamber across a porous membrane, at a spatial scale of 10 mm that is directly analogous to the physical dimensions of a solid tumor at clinical presentation. The design supports interchangeable gradient geometries, matrix compositions, and multicellular arrangements, making it reconfigurable across disease contexts without requiring a new fabrication run.

Microfluidic device features were designed using AutoCAD software. Photomasks were printed from these designs and used for wafer fabrication. Master molds were generated using standard photolithography techniques with SU-8 2075 negative photoresist[79]. SU-8 was dispensed onto a 4-inch silicon wafer and allowed to spread for 10 seconds, then spun

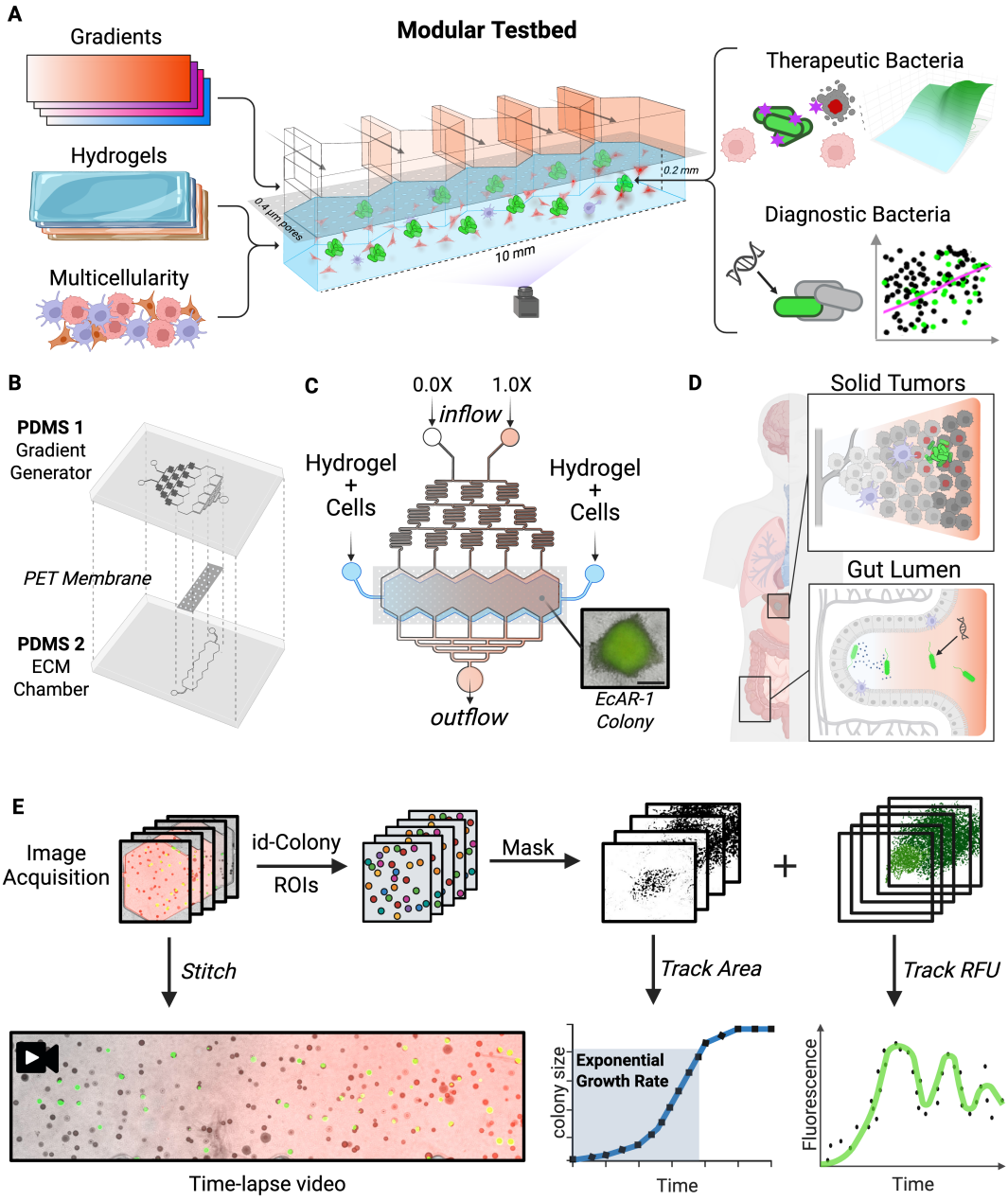


Figure 3.1. Modular testbed for engineered bacteria. **(A)** A customizable microenvironmental testbed combines nutrient gradients, hydrogel matrices, and human cells of choice, where therapeutic or diagnostic bacterial dynamics are monitored and characterized. **(B)** Chip assembly for the customized testbed following bonding of PDMS flow gradient layer and hydrogel cell culture chamber separated by a porous PET membrane. **(C)** Schematic of the top view of the constructed testbed with representative microscopy of an engineered bacterial colony. **(D)** Example of replicable environments for intratumoral bacterial drug delivery and gastric DNA biosensing. **(E)** Imaging and data gathering pipeline outputs stitched time-lapse recording and single colony growth and gene expression dynamics.

at 2,400 rpm for 30 seconds to achieve a uniform channel height of approximately 200 μm. Following spin-coating, wafers were soft-baked at 95°C for 1 hour on a programmable hot plate. After UV exposure and post-exposure bake, features were developed using SU-8 developer solution, rinsed, and dried with nitrogen gas.

PDMS molds were fabricated using standard soft lithography procedures. A 10:1 ratio of Dow Corning Sylgard 184 elastomer base to curing agent was thoroughly mixed and degassed in a vacuum desiccator for 15–30 minutes. The degassed PDMS was poured over the SU-8 patterned silicon wafer and baked at 95°C for 1 hour. Once cooled, the cured PDMS was released from the mold. The device was assembled as a three-layer PDMS–membrane–PDMS stack bonded to glass. The cultivation chamber measured approximately 10 mm $\times$ 2 mm $\times$ 0.2 mm, corresponding to a total culture volume of 4 μL. A 0.4 μm pore PET membrane was trimmed to match the footprint of the cell chamber. The top PDMS layer and membrane were exposed to oxygen plasma and immediately brought into contact, then aligned and bonded to the bottom PDMS slab. The bottom PDMS surface was plasma-treated and bonded to a No. 1.5 glass coverslip to complete the three-layer stack. The assembled device was baked at 37°C for 2 hours to reinforce all plasma bonds before use.

3.3.2 SLC Dynamics under Hypoxic Conditions

We constructed a TME testbed by overlaying a hypoxic gradient across a type I collagen matrix. Within this environment, we embedded StSLC-1 cells, a *S. typhimurium* strain engineered with the synchronized lysis circuit (SLC), a design that couples the positive feedback of Lux operon quorum sensing to the bacteriophage ϕX174 E lysis gene[64]. This genetic circuit enables a coordinated colony-wide burst and subsequent release of a therapeutic payload cloned under SLC regulation (Fig. 3.2A). The testbed's tunable oxygenation relies on the O_2 scavenging properties of a 0–1% sodium sulfite gradient for cell culture from normoxia to anoxia, as previously established[93, 86]. This configuration serves to monitor SLC dynamics in the targeted environment of a diffusion-limited avascular fibrotic tumor stroma (Fig. 3.2B)[94]. The

10 mm length of the TME testbed is analogous to solid tumors of 2 cm in diameter, representative of the physical scale of colorectal cancer at diagnosis (Fig. 3.2C).

Before examining spatial responses across the hypoxia gradient, we first asked whether three-dimensional growth in collagen altered the temporal dynamics of the SLC itself. Time-lapse imaging revealed that StSLC-1 colonies underwent cycles of activation and lysis approximately 16 hours apart under hypoxic conditions (Fig. 3.2D, Video S1). This period, compared with approximately 5 hours in 2D microfluidic traps, approximately 10 hours in 3D normoxia, and approximately 23 hours in reported *in vivo* murine tumor studies, demonstrates that dimensional context and oxygen availability are independent contributors to circuit activation timing, and their combination in the TME testbed places SLC dynamics within the same order of magnitude as those observed in living tumors[64]. Beyond approaching *in vivo* dynamics, these experiments revealed an oxygen-dependent suppression of SLC effective carrying capacity, manifested as a gradual dampening of the population threshold required for quorum activation across conditions (Fig. 3.3).

To visualize how the TME modulates the circuit's activity, we imaged SLC-regulated GFP fluorescence along the 10 mm hypoxic gradient over time. Colonies positioned near normoxia exhibited earlier and stronger activation, which dampened and delayed towards the hypoxic region over 90 minutes (Fig. 3.2E, Video S2). This effect manifested as a wave-like propagation of SLC activation from the normoxic towards the hypoxic end of the chamber, suggesting oxygen availability influences quorum signal accumulation of N-acyl homoserine lactone (AHL) and therefore circuit timing. Through our imaging pipeline, we mapped the spatiotemporal activation of the SLC, quantifying and confirming the observed behavior (Fig. 3.2F). Single colony tracking showed an oxygen-dependent effect on growth and timing of SLC triggering (Fig. 3.2G,H), which revealed a strong correlation between hypoxia-modulated growth rate and circuit activation (Fig. 3.2I).

Although the TME hypoxic gradient clearly affects bacterial growth rate and therefore SLC dynamics, we investigated the potential coupling of inter-colony quorum sensing. We

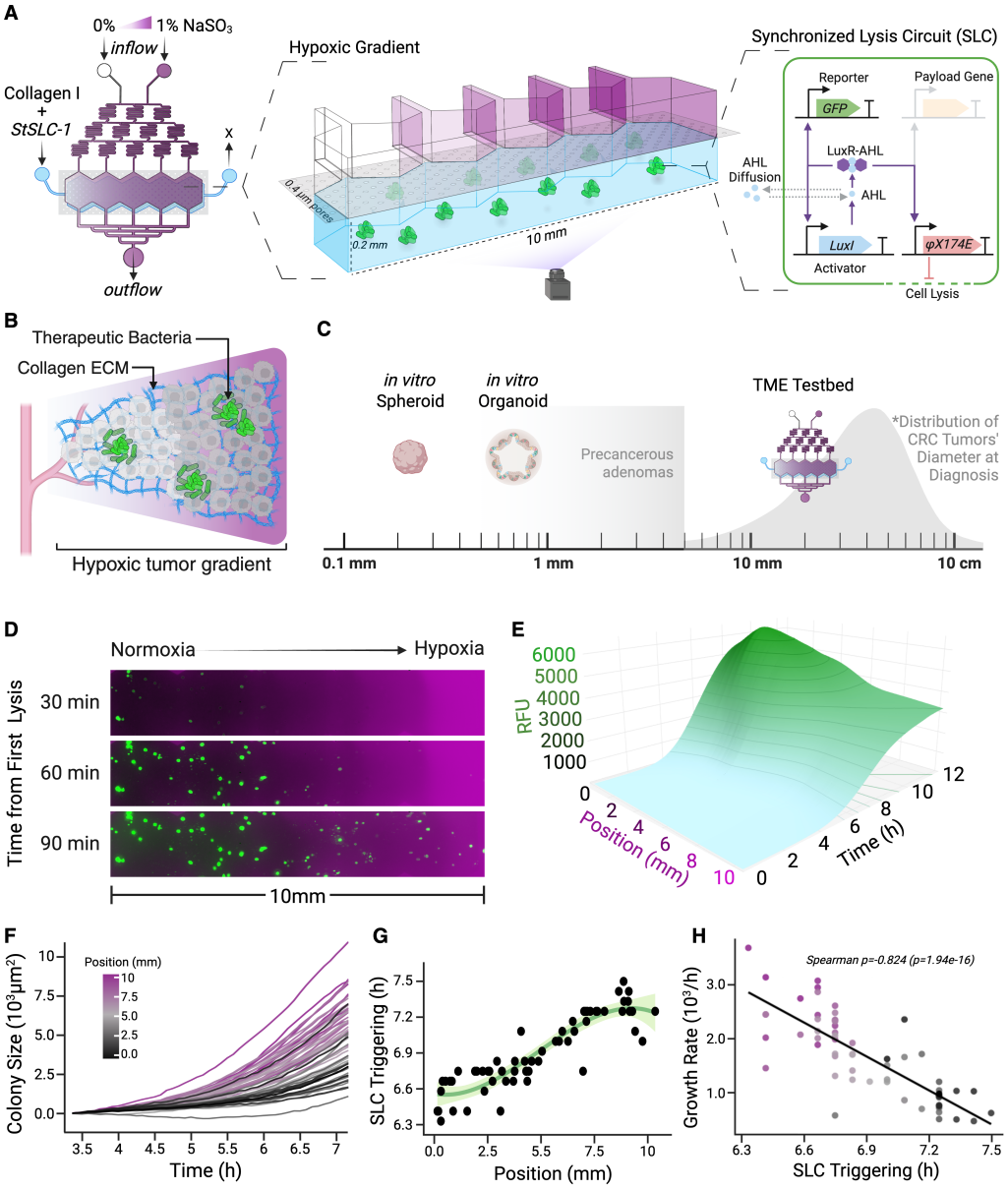


Figure 3.2. TME testbed recapitulates *in vivo* SLC dynamics. **(A)** Schematic of the TME testbed: oxygen quencher gradient over a 10 mm collagen type I matrix embedded with StSLC-1, an *S. typhimurium* strain carrying the SLC. **(B)** Time-lapse imaging of a single StSLC-1 colony in 3D collagen; brightfield (top) and GFP (bottom) show growth-lysis cycles. Scale bars, 100 µm. **(C)** Oscillatory SLC dynamics across conditions of increasing physiological complexity. **(D)** SLC inter-peak intervals: ∼5 h (2D traps), ∼10 h (3D normoxia), ∼16 h (hypoxia), ∼23 h (*in vivo*). **(E)** Wave-like SLC colony triggering along the hypoxic gradient. **(F)** Spatiotemporal map of SLC triggering across the chamber. **(G)** Population tracking of StSLC-1 colonies during pre-lysis growth. **(H)** SLC inflection time versus position along the hypoxic gradient. **(I)** Growth rate correlates with inflection time, indicating hypoxia-dependent SLC modulation.

introduced an AHL-biosensing strain, EcAHL-1, into the TME testbed alongside StSLC-1 cells. This biosensor circuit carries an mScarlet gene under the regulation of the pLux promoter, allowing us to map the diffusion of AHL in real time (Fig. 3.2A). As the StSLC-1 activation wave emerged, AHL diffused and propagated ahead of the SLC activation front, indicating that an AHL cascade contributes to the wave-like triggering of the SLC towards hypoxia (Fig. 3.2B,C, Video S3). To further test how physical properties of the matrix modulate this coupling, we spatially arranged the testbed with StSLC-1 confined to the first section of the chamber and EcAHL-1 in the remaining regions, while tuning extracellular matrix (ECM) stiffness by varying telopeptide content in the collagen hydrogel (Fig. 3.2D). Under stiffer conditions, AHL diffusion significantly dampened from 3.3 mm/h to 0.66 mm/h (Fig. 3.2E,F). Together, these results demonstrate that tissue-scale circuit behavior emerges from the interplay between oxygen-dependent growth and matrix-dependent quorum coupling, both of which shape SLC activation across the TME. Having established that the physical environment actively reshapes a well-characterized circuit, we next asked whether the same physiological constraints alter the copy number patterning behavior of the duplicate origin strain introduced in Chapter 2.

3.3.3 Duplicate Origin Strain Behavior in the Microfluidic Testbed

The SLC and chassis comparison experiments established how the physical properties of the testbed reshape circuit dynamics and therapeutic reach. We next asked whether the three-dimensional, diffusion-limited environment of the testbed similarly reshapes the copy number patterning behavior of the duplicate origin strain characterized in Chapter 2. In the standard microfluidic monolayer device, phenotypic separation of the dOri_AHL strain emerged within approximately 4 hours under opposing AHL and arabinose gradients, with clear spatial partitioning of GFP- and RFP-dominant subpopulations across the trap. Translating this experiment into the testbed context requires the strain to pattern not across a 250 μm monolayer trap but across a 10 mm collagen matrix, a scale that introduces substantially longer diffusion times for both inducers and imposes the same three-dimensional growth constraints that shifted SLC timing by

nearly an order of magnitude.

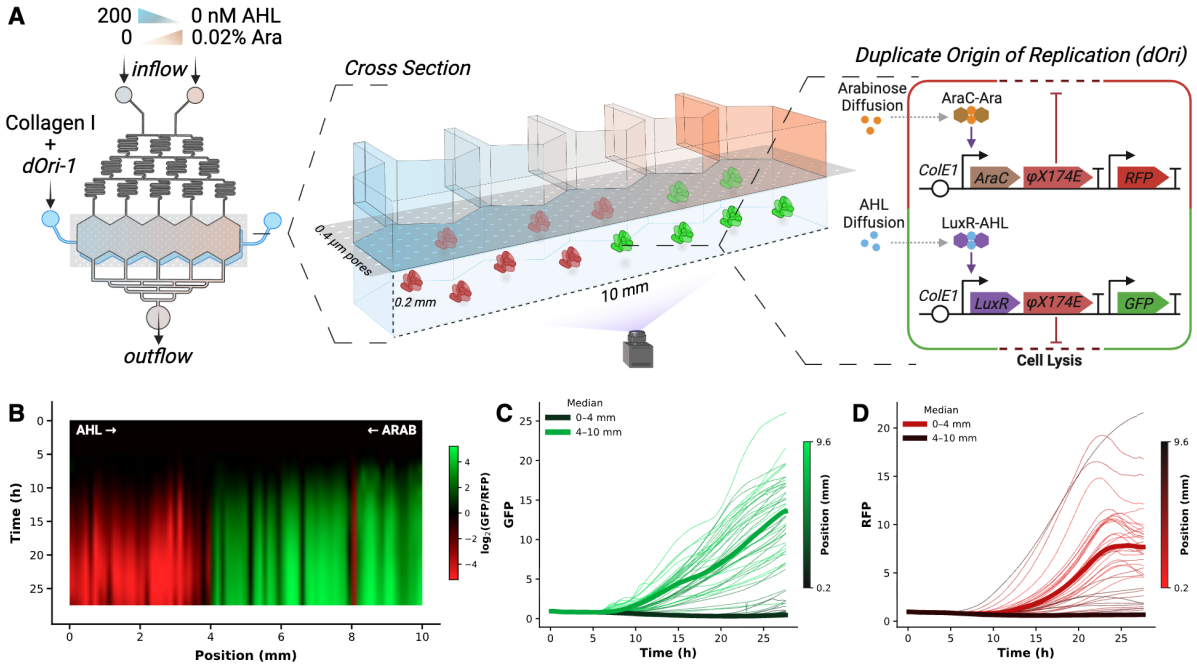


Figure 3.3. Duplicate origin strain patterning in the microfluidic testbed. **(A)** Testbed schematic with dOri_AHL embedded in a type I collagen matrix under opposing gradients of 200 nM AHL and 0.02% arabinose, with circuit diagram showing the duplicate ColE1 origin architecture. **(B)** Kymograph of $\log_2$(GFP/RFP) ratio over 25 hours across the 10 mm chamber. AHL-proximal colonies shift toward GFP dominance while arabinose-proximal colonies shift toward RFP dominance; patterning stabilizes within approximately 10 hours. **(C)** GFP fluorescence traces of individual colonies colored by position; colonies in the 0–4 mm region accumulate substantially higher GFP. **(D)** RFP fluorescence traces showing the inverse relationship: 4–10 mm colonies accumulate RFP while 0–4 mm colonies remain low.

We deployed dOri_AHL in the testbed under an opposing gradient of 200 nM AHL and 0.02% arabinose across a type I collagen matrix, using the same chip geometry and imaging pipeline applied to the SLC and co-culture experiments (Fig. 3.3A). Time-lapse imaging of both GFP and RFP fluorescence channels revealed that spatial patterning emerged and stabilized within approximately 10 hours, comparable to the timescale observed in the monolayer device despite the substantially larger spatial domain (Fig. 3.3B). Colonies in the AHL-proximal region of the chamber progressively accumulated GFP fluorescence, indicating preferential expansion of cells with high copy number of the AHL-responsive plasmid, while colonies in the arabinose-proximal region showed the inverse behavior, accumulating RFP as copy number shifted toward

the arabinose-responsive plasmid (Fig. 3.3C,D). The spatial boundary between GFP-dominant and RFP-dominant subpopulations was reproducible across replicates and persisted for the duration of imaging, consistent with the long-term phenotypic memory described in Chapter 2.

These results establish that coupled plasmid patterning is not restricted to the well-controlled, convection-dominated environment of the monolayer microfluidic trap but operates robustly under the diffusion-limited, three-dimensional conditions of the testbed. The persistence of spatial patterning across a tissue-scale collagen matrix, where chemical gradients form through passive diffusion rather than imposed flow, directly supports the translational premise of Chapter 4: that coupled plasmid dynamics can generate and maintain phenotypically distinct subpopulations across the gradients present in solid tumors, without requiring external inputs or additional regulatory circuitry.

3.3.4 Cancer Co-culture and Chassis-Dependent Therapeutic Reach

To quantify how engineered bacteria kill cancer cells across tissue-scale distances, we optimized a co-culture testbed that supports both microbial growth and HCT116 viability. We developed a unified culture medium by supplementing DMEM with tryptone and yeast extract, which enabled stable long-term co-culture and allowed us to monitor therapeutic efficacy continuously (Fig. 3.4). Bacteria were confined to the first 2 mm of the culture chamber, while HCT116 cells occupied the remaining 8 mm (Fig. 3.4A). Engineered strains carry the SLC driving expression of Hemolysin E (HlyE), a pore-forming toxin that disrupts mammalian membranes and permits nuclear accumulation of ethidium homodimer (EtHD), providing a direct fluorescent readout of cancer cell death across space and time (Fig. 3.4B). This configuration allowed us to directly compare two therapeutic chassis, non-motile *E. coli* EcSLC-2 versus motile *Salmonella typhimurium* StSLC-2, and determine how chassis traits influence the spatial reach of lysis-based delivery.

Quantitative viability analysis showed that HCT116 cell death was primarily driven by the presence of HlyE, with an additional contribution from the *S. typhimurium* chassis (Fig. 3.4C).

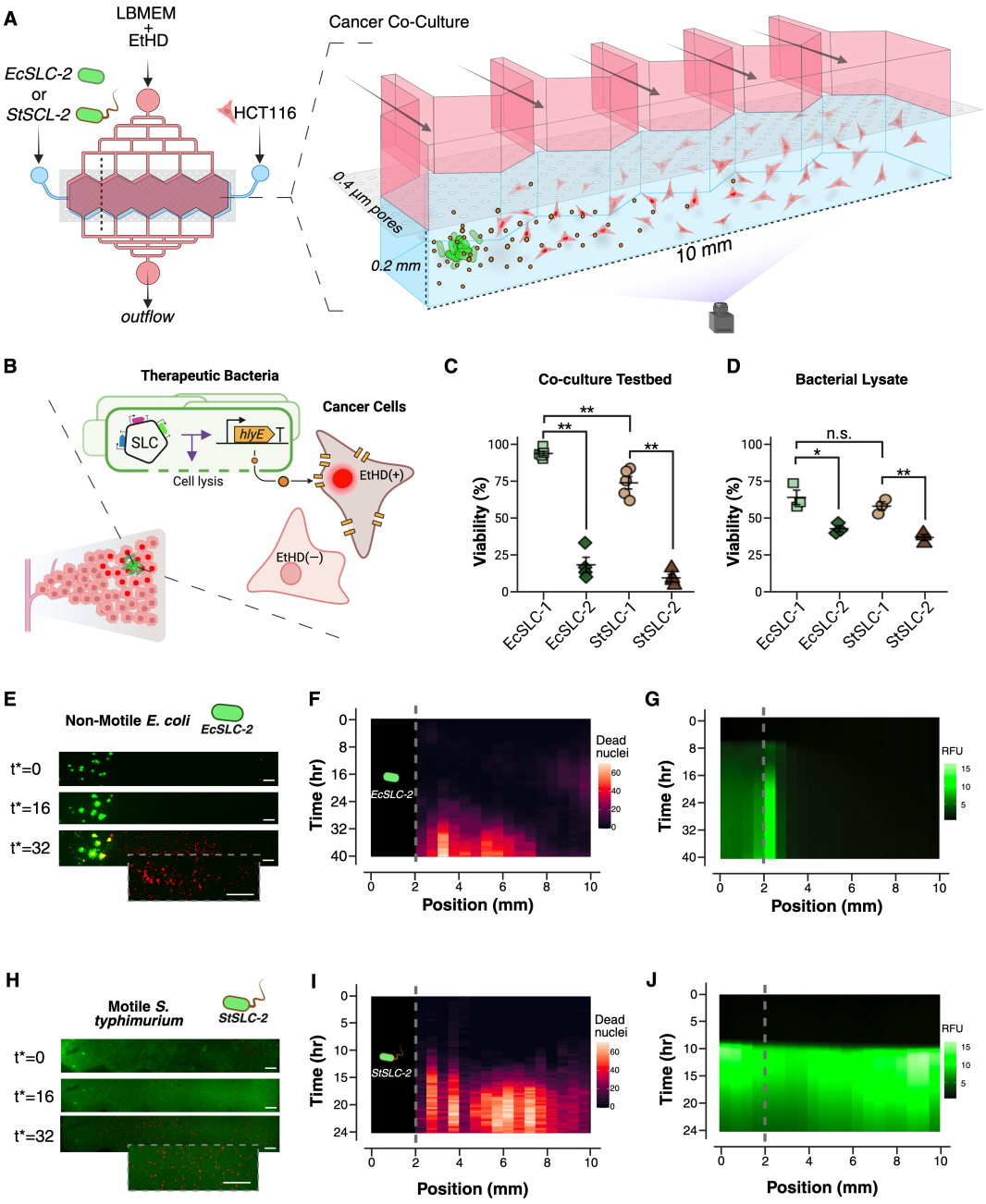


Figure 3.4. Cancer co-culture testbed reveals effect of therapeutic chassis. **(A)** Co-culture setup: SLC bacteria (EcSLC-2 or StSLC-2) seeded in the first 2 mm, HCT116 cells in the remaining 8 mm. **(B)** SLC bacteria release HlyE upon lysis; affected HCT116 cells are visualized by nuclear EtHD accumulation. **(C)** Cancer cell viability is primarily driven by HlyE, with an additional contribution from the *S. typhimurium* chassis. Student's t-test ($n = 5$). **(D)** Lysate treatment reproduces cytotoxicity independent of chassis ($n = 3$). **(E)** Localized EcSLC-2 triggering and proximal HCT116 death. Scale bar = 0.5 mm. **(F)** Spatiotemporal viability map: HCT116 death localized near the EcSLC-2 zone at 48 h. **(G)** Localized triggering of non-motile EcSLC-2 over time. **(H)** Widespread StSLC-2 triggering. Scale bar = 0.5 mm. **(I)** Widespread HCT116 death within 24 h. **(J)** Widespread triggering of motile StSLC-2 over time.

To distinguish toxin activity from chassis-specific effects, we treated plated HCT116 cells with bacterial lysates. This reproduced the cytotoxic response in a chassis-independent manner, confirming that HlyE activity rather than live infection accounted for the observed cell death (Fig. 3.4D). The residual viability loss observed with live StSLC-2 in the testbed is likely linked to extensive motile expansion, which increases resource competition and environmental stress on co-cultured HCT116 cells rather than reflecting additional toxin activity.

When spatially resolved, the two chassis showed drastically different localization and therapeutic reach. Non-motile EcSLC-2 colonies lysed locally in their seeded region, followed by a progressive HCT116 cell death proximal to the interface over 32 hours, indicating slow therapeutic diffusion (Fig. 3.4E–G). In contrast, motile StSLC-2 exhibited widespread activation across the chamber, resulting in more rapid HCT116 cell death throughout the testbed starting around 5 hours after lysis (Fig. 3.4H–J). These findings demonstrate that bacterial chassis and motility substantially expand the therapeutic reach of lysis-based payload delivery within tissue-like environments. Together with the SLC hypoxia results, they reinforce the broader argument that circuit output in the testbed is determined as much by physical and biological context as by the genetic design, a principle that extends beyond therapeutic delivery to detection applications as well.

3.3.5 DNA Biosensing across Physiological Matrices

Beyond their therapeutic potential, bacteria can be engineered to detect disease signatures *in vivo*[67, 65, 95, 66]. We constructed a gut lumen testbed composed of a mucin type III hydrogel, where we explored the efficacy of the recently developed diagnostic strain AbDNA-1[65]. This *Acinetobacter baylyi* chassis couples natural competence with a recombination-based genetic switch to detect environmental target DNA. When target DNA containing a homologous "landing pad" sequence enters AbDNA-1 cells, the fragment is homologously recombined to disrupt tetR-mediated repression of a GFP reporter gene.

After confirming positive AbDNA-1 reporting with 1 ng/μL of target DNA in the mucin

type III testbed, we overlaid an oxygen-quencher gradient to mimic the hypoxic and viscous environment of the intestinal lumen (Fig. 3.5A,B)[96, 93]. Time-lapse imaging revealed GFP-positive colonies localized near normoxia had a higher detection frequency, from 60% to 20%, and increased fluorescence intensity by twofold (Fig. 3.5C). Colonies within oxygen-limited regions exhibited slower growth rate and fewer activation events, suggesting that lumen hypoxia influences the efficacy and timing of DNA uptake (Fig. 3.5D).

To evaluate the diagnostic range of AbDNA-1 to detect circulating DNA diffused into solid tissue, we also assessed a collagen I testbed under a target DNA gradient (0–1 ng/μL) across the 10 mm chamber (Fig. 3.5E). The fraction of GFP-positive colonies increased with target DNA concentration, rising from approximately 2% in the 0–2 mm region to approximately 24% at 8–10 mm (Fig. 3.5F). These results show that AbDNA-1 functions as a sensitive and spatially resolved biosensor of extracellular DNA across both mucinous and collagenous matrices, maintaining activity across physiological gradients.

The testbed also provides a natural framework for characterizing engineered bacterial ecologies whose dynamics are intrinsically dependent on spatial context. As a demonstration of this generalizability, we deployed the three-strain Survival of the Weakest (SOW) ecology[97], in which cyclic toxin-antitoxin interactions between strains produce coexistence dynamics that are only resolvable in spatially structured environments. Spatiotemporal imaging captured the redistribution of strain densities across the chamber between 20 and 40 hours, revealing emergent spatial segregation inaccessible in well-mixed culture (Fig. 3.5).

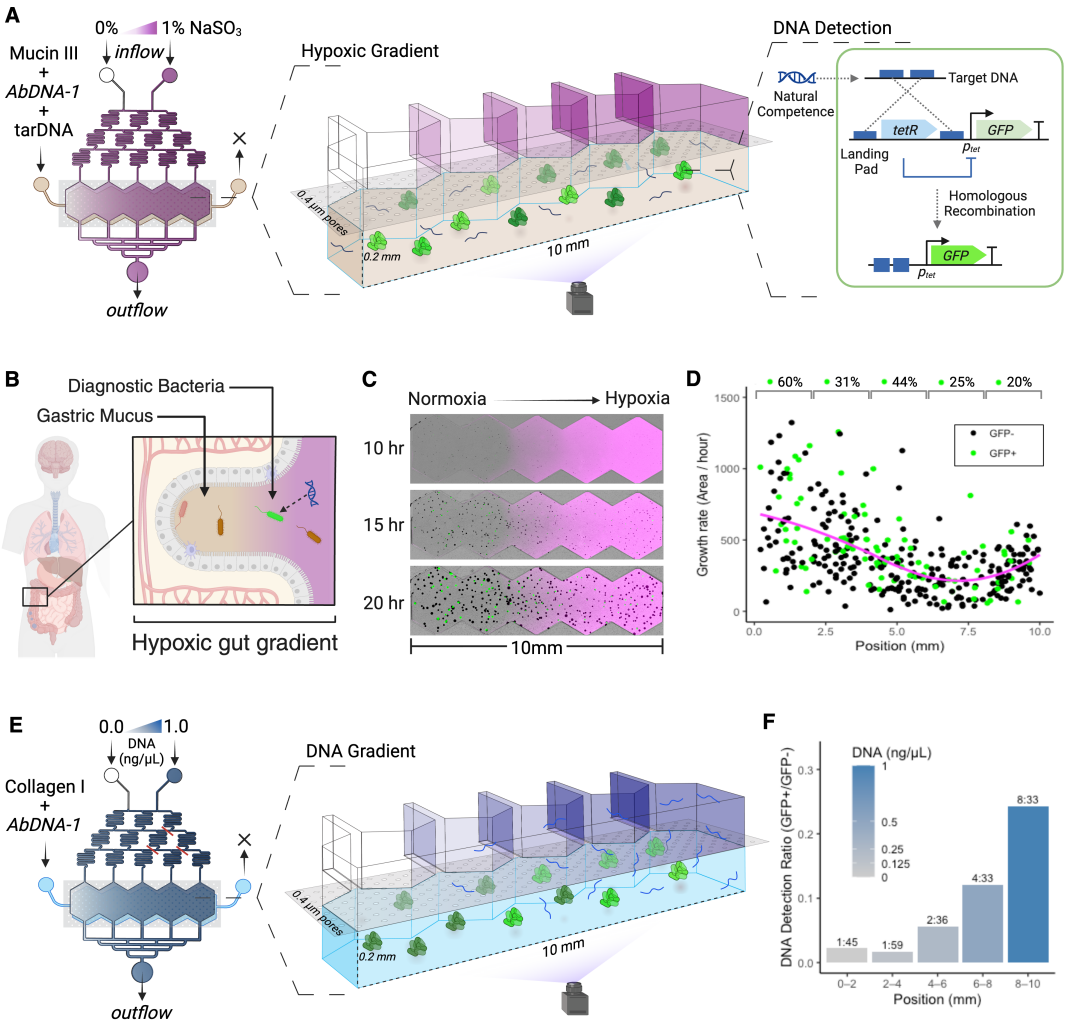


Figure 3.5. DNA biosensing in the gut lumen and solid tissue testbed. **(A)** Gut lumen testbed features an oxygen quencher gradient over a mucin type III alginate hydrogel embedded with target DNA and AbDNA-1 diagnostic bacterial strain. *A. baylyi* natural competence allows for homologous recombination of target DNA and subsequent disruption of tetR repression of the GFP reporter gene. **(B)** Major features of gut lumen microenvironment mimicked by testbed. **(C)** Microscopy images of AbDNA-1 colonies detecting target DNA along hypoxic gradient. **(D)** Growth rate scatter distribution of AbDNA-1 colonies along hypoxic testbed. **(E)** DNA gradient testbed features a 0–1 ng/µL target DNA distribution over a collagen I matrix embedded with AbDNA-1 bacteria. **(F)** Effective frequency of DNA detection of stepwise concentrations of diffusing target DNA into collagen ECM.

3.4 Discussion

As engineered bacteria advance toward clinical testing as smart therapeutics and diagnostics, resolving their physiological circuit behaviors hinges on studying them within the environmental context of their target niche. Chapter 2 established that the environment is not merely a backdrop for genetic circuit function but an active parameter that determines which behaviors a population expresses: the coupled plasmid patterning capacity was always encoded in the duplicate origin architecture, but only became accessible when a spatially structured environment gave fitness-based selection something to act on. This chapter extends that logic from a model gradient system to a physiologically grounded one. By modulating gradients, extracellular matrices, and multicellular arrangements, our testbeds reveal that the spatial organization and physicochemical properties of tissues reshape how engineered bacteria grow, communicate, and activate genetic programs in ways that neither standard *in vitro* systems nor *in vivo* models can resolve.

The TME and quorum-coupling results together make a single point that neither microfluidic traps nor tumor spheroids can make alone: circuit timing and colony-to-colony communication are both governed by physical context. The SLC period shift from approximately 5 hours in 2D microfluidic traps toward approximately 16 hours in collagen under hypoxia, approaching the range observed in murine tumor models[64], emerges from unconfined three-dimensional growth in combination with oxygen-dependent growth rate suppression, a condition that spheroid models approximate but cannot resolve at the scale required to capture the underlying mechanism[98, 8]. That mechanism is an oxygen-dependent dampening of growth rate propagating as a wave of AHL-driven SLC activation across a centimeter-long tissue analog, which is only resolvable when gradient, matrix, and circuit readout are simultaneously accessible. The stiffness-dependent attenuation of AHL propagation is a direct example of circuit-relevant information that no existing model could have produced.

The therapeutics co-culture and diagnostic modules extend this logic across circuit

architectures and disease contexts. In the co-culture testbed, the contrast between non-motile *E. coli* and motile *S. typhimurium* demonstrates that therapeutic reach, timing, and the spatial profile of cancer cell death are all design variables whose values are determined by the tissue environment beyond the genetic circuit alone[99, 75, 100]. In the gut lumen testbed, the spatial variation in AbDNA-1 detection frequency along oxygen and DNA gradients reveals that even genome-integrating biosensors typically evaluated in homogeneous liquid culture exhibit performance landscapes shaped by physiological gradients[65, 67]. Collectively, these results establish that the choice of chassis, matrix, and microenvironmental conditions is as consequential to circuit output as the genetic design itself.

Collectively, these findings reframe the microenvironment as an active and tractable design parameter. Circuit dynamics are not hardwired in DNA alone, and the same genetic payload behaves with drastically different timing, reach, and efficacy depending on the physical context in which it operates. By offering a controlled yet life-like setting, this testbed enables mechanistic interpretation of those effects, helping to explain the discrepancies that consistently emerge when circuits transition from culture flasks to animal models[72, 75]. If the microenvironment is a functional control layer over circuit behavior, then physiological modulation becomes a second programmable axis that can be rationally explored, and ultimately exploited, to improve the predictability and performance of engineered bacteria at the point of deployment.

3.4.1 Limitations of the Study

While the system expands the experimental space for microbial therapeutics, certain limitations should be considered. Although the platform reproduces several fundamental features of tissue physiology, it does not yet incorporate mechanical forces, full immune pressure, or microbiome interactions that could also shape engineered bacterial behavior. Certain disease contexts, such as fluctuating luminal shear or immune-driven clearance, will require additional modules or coupling with tissue-specific organ-chip systems. Likewise, while the platform supports centimeter-scale gradients, larger structures or long-term colonization dynamics may

exceed the current chamber geometry. Future interrogations could incorporate dynamic flow regimes, adaptive ECM remodeling, or patient-derived stromal components.

3.5 Materials and Methods

3.5.1 Microfluidic Device Development and Fabrication

Microfluidic device features were designed using AutoCAD software. Photomasks were printed from these designs and used for wafer fabrication. Master molds were generated using standard photolithography techniques with SU-8 2075 negative photoresist[79]. SU-8 was dispensed onto a 4-inch silicon wafer and spun at 2,400 rpm for 30 seconds to achieve a uniform channel height of approximately 200 µm. Following spin-coating, wafers were soft-baked at 95°C for 1 hour. After UV exposure and post-exposure bake, features were developed using SU-8 developer solution, rinsed, and dried with nitrogen gas. PDMS molds were fabricated at a 10:1 base-to-curing-agent ratio, degassed, poured over the patterned wafer, and cured at 95°C for 1 hour. Individual devices were cut, assembled as a three-layer PDMS–membrane–PDMS stack bonded to a No. 1.5 glass coverslip, and baked at 37°C for 2 hours to reinforce all plasma bonds before use.

3.5.2 Bacterial Strain Preparation

Bacterial strains were revived from -80°C glycerol stocks by inoculating 5 mL of LB medium containing appropriate antibiotic. Cultures were supplemented with 20 µg mL^{-1} of chloramphenicol or 60 µg mL^{-1} of spectinomycin depending on the plasmid selection marker. Cells were incubated overnight at 37°C with shaking at 250 rpm. For strains carrying the ϕX174E lysis gene, 0.2% (w/v) glucose was included in all preculture steps to suppress premature lysis. Overnight cultures were diluted 1:100 into 200 µL fresh LB medium with antibiotic in a flat-bottom 96-well plate and incubated in a Tecan Infinite M200 Pro plate reader at 37°C with continuous orbital shaking. When cultures reached mid-exponential phase ($OD_{600} \approx 0.1$), 2 µL

of culture was transferred and diluted 1:100 into 200 µL of fresh selective medium to generate the working inoculum for matrix incorporation.

3.5.3 Media Preparation

Hypoxic Media.

To generate hypoxic media, a chemical oxygen scavenging system was used as described by Kang et al. (2020). Standard LB media was supplemented with 1% (w/v) sodium sulfite and 100 µM cobalt(II) chloride hexahydrate immediately prior to use. All hypoxic media were freshly prepared and stored in airtight containers until loaded into the chip.

DNA-supplemented Media.

Purified genomic DNA from *A. baylyi* ADP1 containing the GFP insertion at the Ntrl1 locus was added to standard LB medium at a final concentration of 5 ng μL^{-1} immediately prior to use. DNA-enriched media was prepared fresh for each experiment to minimize degradation during long-term perfusion.

Composite LB–MEM Co-culture Media.

For bacterial and HCT116 co-culture experiments, a composite formulation of LB and DMEM (designated LB–MEM) was prepared by dissolving 10 g tryptone, 5 g yeast extract, and 7 g of DMEM powder without glucose in 1 L of deionized water, followed by autoclaving for sterilization.

3.5.4 Mammalian Cell Culturing

HCT116 human colorectal carcinoma cells (ATCC CCL-247) were maintained in RPMI 1640 medium supplemented with 10% FBS and 1% penicillin–streptomycin at 37°C in a humidified 5% CO_2 incubator. Cells were maintained below passage 20 and subcultured at approximately 80% confluence before use in experiments.

3.5.5 Microfluidic Device Loading

Prior to loading, the assembled microfluidic chips were placed under vacuum for at least 45 minutes to remove trapped air from the PDMS and facilitate subsequent matrix filling. A 10 µL aliquot of the cell/ECM mixture was loaded slowly into the chamber inlet. Loading was performed by gently inserting the pipette tip into the chamber port and allowing capillary action and light pressure to guide the gel into the chamber. After confirming the chamber was fully filled, 20 µL of cell-free media was added to each media inlet port before inserting inlet and outlet syringes to seal the device and prepare for flow setup.

3.5.6 Microscopy

Glass-bonded microfluidic chips were placed directly onto the stage of a Nikon Ti-2 inverted microscope housed within a temperature-controlled (37°C) plexiglass incubation chamber. Samples were imaged at 4× magnification, focusing on the center of the 200 µm chamber height corresponding to the middle of the collagen matrix layer. Brightfield, GFP, and RFP channels were acquired every 10 minutes throughout each experiment. For higher-resolution visualization of bacterial colonies, z-stacks were collected at 20× magnification using 10 µm step intervals.

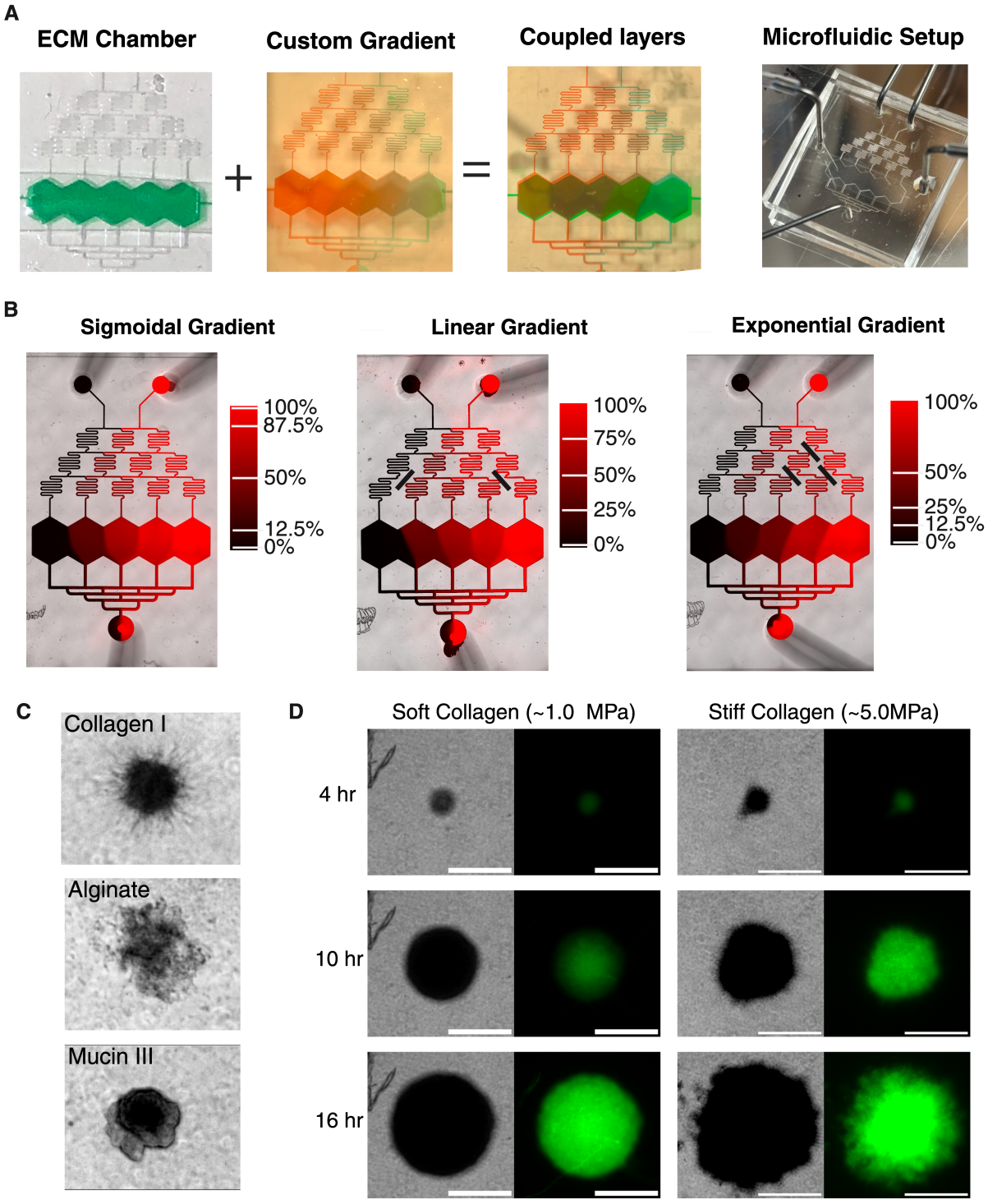
3.5.7 Data Processing

Time-lapse microscopy datasets were exported as ND2 files and stitched into single hyperstacks using an automated ImageJ macro (Fiji, version 2.17.0). The macro aligned sequential fields of view and quantified each bacterial colony's fluorescence intensity and area over time. Growth rates were calculated by fitting the exponential region of the colony area over time to a nonlinear regression model. All subsequent statistical analyses and data visualization were performed in R (version 7.3-55) using base functions and the `ggplot2` package.

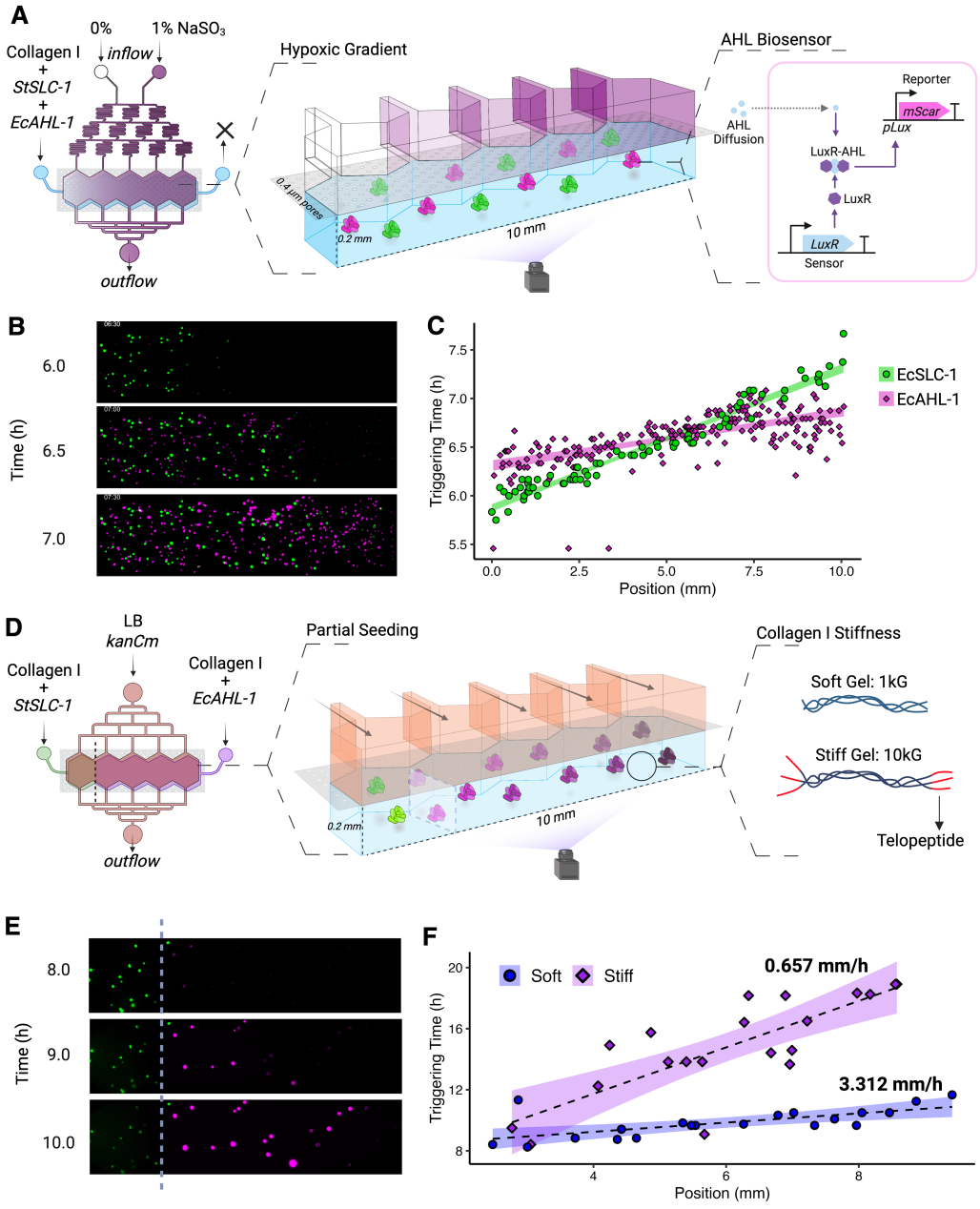
3.6 Supplemental Figures

Table 3.1. Engineered bacterial strains used throughout this dissertation.

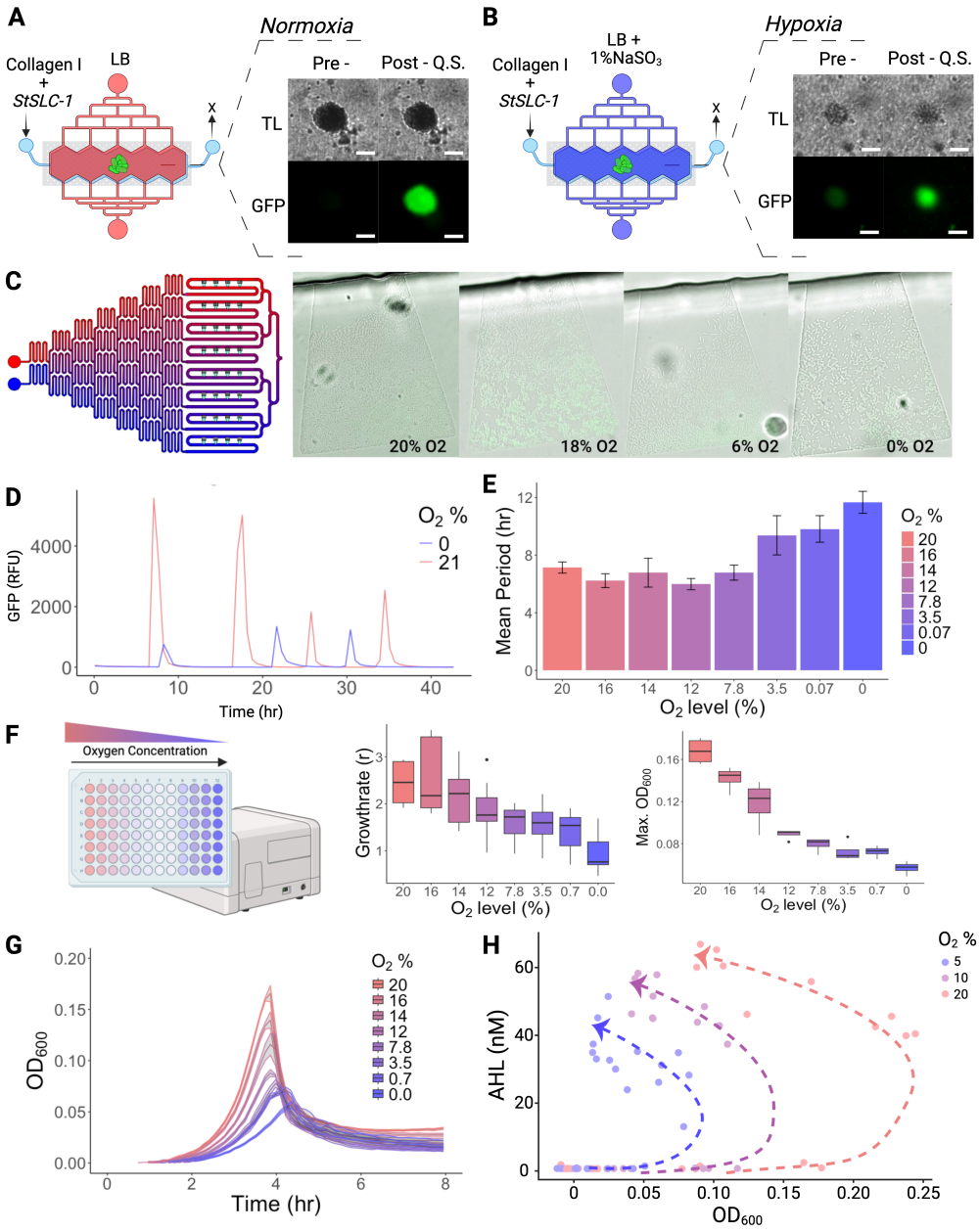
Strain Name	Chassis	Circuit Description	Chapter	Source
dOri_S1	*Escherichia coli*	Coupled plasmid strain encoding AHL-inducible and arabinose-inducible lysis on a shared ColE1 origin of replication; RBS library variant 1	2	Hasty Lab [30]
dOri_S2	*Escherichia coli*	Coupled plasmid strain encoding AHL-inducible and arabinose-inducible lysis on a shared ColE1 origin of replication; RBS library variant 2	2	Hasty Lab [30]
dOri_S3	*Escherichia coli*	Coupled plasmid strain encoding AHL-inducible and arabinose-inducible lysis on a shared ColE1 origin of replication; RBS library variant 3	2	Hasty Lab [30]
dOri_AHL	*Escherichia coli*	Coupled plasmid strain encoding AHL-inducible and arabinose-inducible lysis on a shared ColE1 origin of replication	2, 3	Hasty Lab [30]
EcSLC-1	*Escherichia coli*	Synchronized lysis circuit without therapeutic payload	3	Hasty Lab [14]
EcSLC-2	*Escherichia coli*	Synchronized lysis circuit driving HlyE expression	3	Hasty Lab [14]
StSLC-1	*Salmonella typhimurium*	Synchronized lysis circuit without therapeutic payload	3	Hasty Lab [14]
StSLC-2	*Salmonella typhimurium*	Synchronized lysis circuit driving HlyE expression	3	Hasty Lab [14]
EcAHL-1	*Escherichia coli*	AHL-responsive biosensor reporter circuit	3	This study
AbDNA-1	*Acinetobacter baylyi*	Homologous recombination DNA biosensor circuit	3	Hasty Lab [101]
EcSOW-1	*Escherichia coli*	Survival-of-the-weakest ecological circuit encoding Tox1–Anti1–Anti2–GFP	3	Hasty Lab [97]
EcSOW-2	*Escherichia coli*	Survival-of-the-weakest ecological circuit encoding Tox3–Anti3–Anti1–RFP	3	Hasty Lab [97]
EcSOW-3	*Escherichia coli*	Survival-of-the-weakest ecological circuit encoding Tox2–Anti2–Anti3–CFP	3	Hasty Lab [97]
dOri_Lac	*Escherichia coli*	Coupled plasmid strain encoding lactate/arabinose lysis on a shared ColE1 origin of replication	4	This study
dOri_SLC-A	*Escherichia coli*	Coupled plasmid strain encoding arabinose-inducible lysis and the synchronized lysis circuit on a shared ColE1 origin of replication	4	This study
dOri_SLC	*Escherichia coli*	Lactate-gated synchronized lysis circuit within the coupled plasmid framework	4	This study



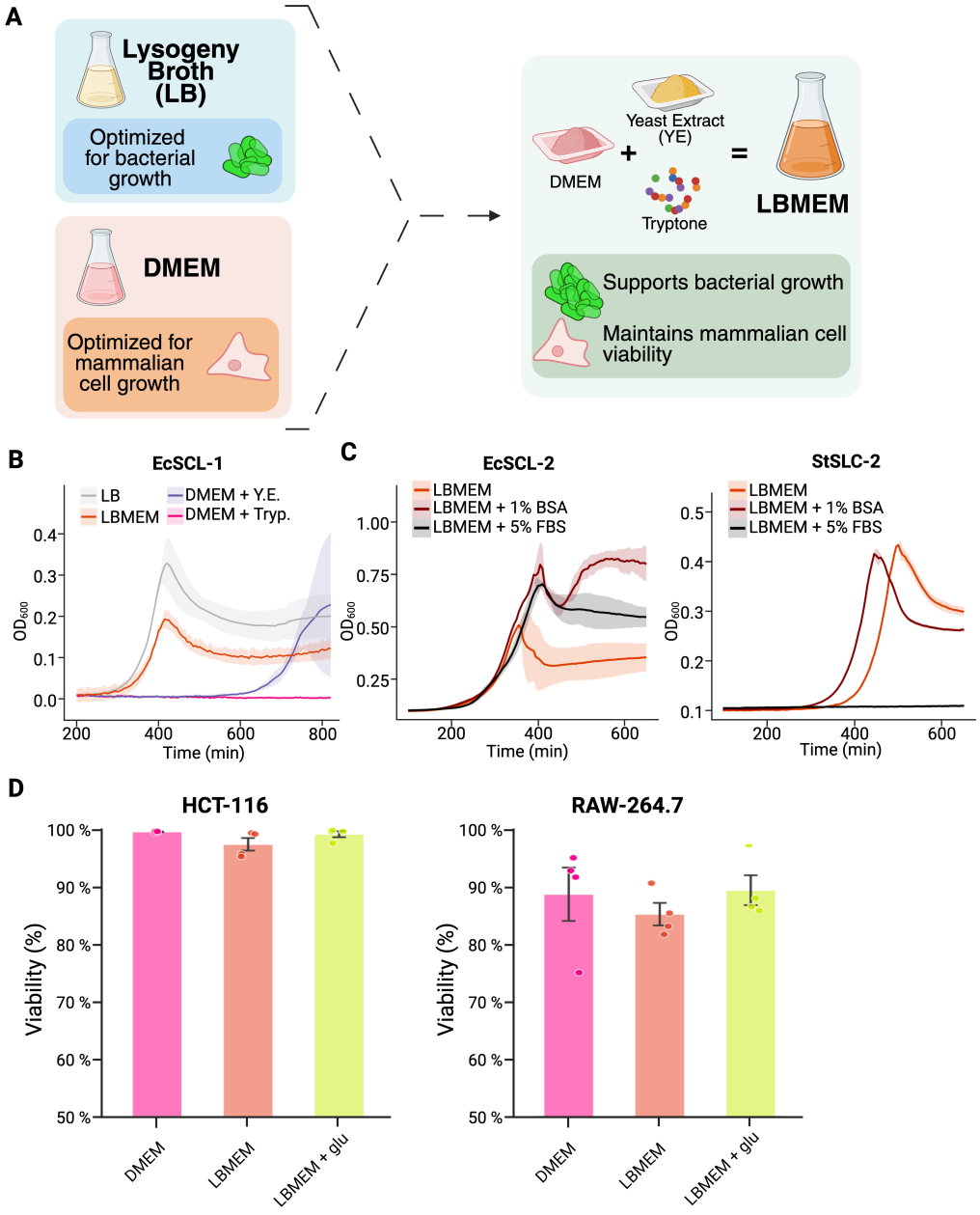
Supplemental Figure 3.1. Independent modularity of nutrient distribution and hydrogel composition. **(A)** Representative photographs of gradient generating layer, ECM culturing chamber, and device assembly. **(B)** Top layer designs can be customized to generate different nutrient distributions, such as sigmoidal, linear, or exponential gradient shapes. **(C)** Morphology effects of hydrogel composition on *E. coli* MG1655 colonies. **(D)** Growth and gene expression of EcGFP-1 strain in soft or stiff collagen type I matrix.



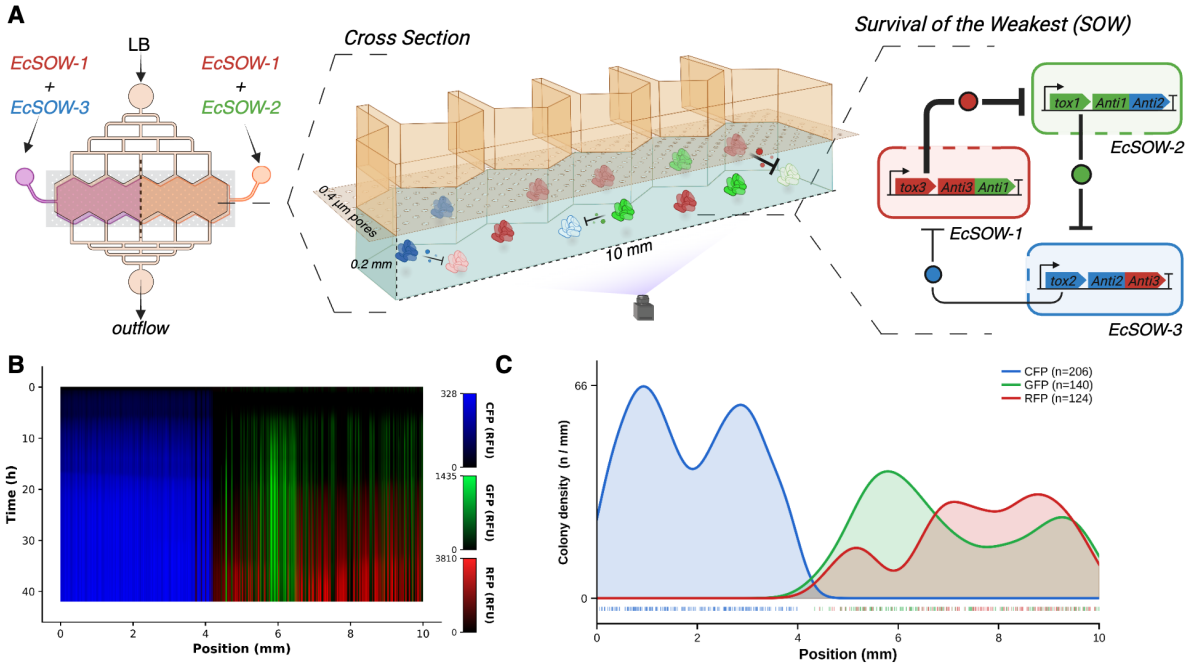
Supplemental Figure 3.2. Quorum coupling propagation and matrix mechanics. **(A)** TME testbed co-embedded with StSLC-1 and EcAHL-1, which reports AHL via mScarlet under pLux regulation. **(B) and (C)** EcAHL-1 activation precedes StSLC-1 triggering along the hypoxic gradient, confirming that AHL diffusion propagates ahead of the SLC activation front. Linear regression with shaded 95% CI. StSLC-1: slope = 0.143 ± 0.004 h/mm (R^2 = 0.95, $p < 2 \times 10^{-16}$, n = 77); EcAHL-1: slope = 0.055 ± 0.005 h/mm (R^2 = 0.41, $p < 2 \times 10^{-16}$, n = 209). **(D)** Stiffness-perturbation schematic: StSLC-1 confined to the first section, EcAHL-1 downstream, in collagen matrices of varying telopeptide content. **(E) and (F)** Increasing matrix stiffness reduces AHL propagation rate from 3.3 mm/h to 0.66 mm/h. Soft: slope = 0.302 ± 0.079 h/mm (R^2 = 0.45, $p = 1.3 \times 10^{-3}$); stiff: slope = 1.521 ± 0.270 h/mm (R^2 = 0.64, $p = 2.4 \times 10^{-5}$).



Supplemental Figure 3.3. Oxygen-dependent modulation of SLC circuit dynamics. **(A) and (B)** Validation of hypoxic testbed: StSLC-1 colonies under normoxia (LB) and hypoxia (LB + 1% $NaSO_3$) confirm lysis in both conditions by brightfield and GFP imaging. **(C)** Brightfield images of StSLC-1 at 20%, 18%, 6%, and 0% O_2 showing graded suppression of quorum density in 2D traps. **(D)** Representative GFP traces under normoxia (21% O_2) and anoxia (0% O_2), showing extended period and dampened amplitude under oxygen limitation. **(E)** Mean inter-peak interval across eight O_2 levels demonstrates a graded, nonlinear dependence of circuit period on oxygen availability. **(F)** Plate reader characterization of SLC growth rate and maximum OD_{600} across O_2 levels, showing progressive suppression under hypoxia. **(G)** OD_{600} time courses across all O_2 conditions. **(H)** AHL vs. OD_{600} phase diagram at 5%, 10%, and 20% O_2, revealing kinetic coupling between bacterial growth and AHL accumulation as the mechanistic basis for hypoxia-dependent delays in SLC activation.



Supplemental Figure 3.4. LBMEM supports mammalian viability while preserving strain-specific SLC dynamics. **(A)** Schematic of LBMEM, a hybrid medium formed by supplementing DMEM with tryptone and yeast extract to combine compatibility with mammalian cells and support for bacterial growth. **(B)** EcSLC-1 growth in LB, LBMEM, DMEM + yeast extract, and DMEM + tryptone. LBMEM supports growth followed by a sharp OD decrease, consistent with SLC-mediated lysis. **(C)** EcSLC-2 and StSLC-2 growth in LBMEM with or without 1% BSA or 5% FBS. These dynamics were differentially affected by mammalian culture additives, with BSA altering EcSLC-2 behavior and FBS strongly suppressing StSLC-2 lysis-associated dynamics. **(D)** HCT116 and RAW-264.7 viability in DMEM, LBMEM, and glucose-supplemented LBMEM. LBMEM maintained high viability in both mammalian cell lines, enabling continuous bacterial–mammalian co-culture.



Supplemental Figure 3.5. Survival of the Weakest ecology in the microfluidic testbed. **(A)** Schematic of the Survival of the Weakest (SOW) testbed, featuring spatial co-seeding of three *E. coli* strains (EcSOW-1, EcSOW-2, EcSOW-3) engaged in cyclic toxin-antitoxin interactions[97]. Each strain produces a toxin targeting one competitor while carrying antitoxins against the other, creating a non-transitive ecological dynamic analogous to a rock-paper-scissors game. **(B)** Spatiotemporal fluorescence heatmap across the chamber over 40 hours, showing the emergence of spatially structured strain coexistence from an initially mixed population. **(C)** Colony density distributions by position for CFP, GFP, RFP, and lysed colonies at 24 hours, revealing progressive spatial segregation and strain-specific expansion dynamics inaccessible in well-mixed culture.

Chapter 3, in part, is currently being prepared for submission for publication of the material. Rey-Bedón, C., Steppe, P.*, Rosen, A., Emmanuele, P., Cooper, R., Zarrinpar, A., and Hasty, J. Microphysiological test-bed for engineered bacteria. Cell Resources (2026, Final Editing Stage). The dissertation author was a primary investigator and co-first author of this paper.*

Chapter 4

A Lactate-Gated Synchronized Lysis Circuit within a Coupled Plasmid Framework

4.1 Abstract

Live bacterial therapeutics are emerging as a powerful platform for precision oncology. Their inherent tumor-tropism, persistence in hypoxic and necrotic regions, and amenability to genetic programming make them ideal candidates for therapeutic delivery within the tumor microenvironment (TME). Yet most current designs rely on fixed genetic architectures that fail to capture the spatial and temporal heterogeneity of solid tumors. Here, we present an adaptive framework for bacterial cancer therapy that integrates tumor-responsive sensing, population-level coordination, and plasmid-based adaptability. Using a plasmid system with coupled origins of replication, we show that bacterial populations can dynamically shift plasmid copy number to align therapeutic output with environmental lactate gradients. By coupling lactate-inducible lysis with a synchronized lysis circuit (SLC), we demonstrate cyclical, biomarker-dependent therapeutic release that is both spatially confined and self-regulated. This plasmid-level mechanism transforms copy-number variation from a source of instability into a programmable tool, enabling a single bacterial strain to autonomously alternate between sensing and delivery modes. Together, these results establish coupled plasmid systems as a generalizable strategy for engineering spatially and temporally adaptive microbial therapies.

4.2 Introduction

Harnessing bacteria as living cancer therapeutics has moved from proof-of-concept studies to a rapidly expanding field, driven by advances in synthetic biology and a growing recognition of the unique advantages of bacterial tumor colonization[9, 102, 11, 63]. Bacteria have been widely explored as therapeutic platforms because they naturally colonize solid tumors, persist in hypoxic and necrotic regions, and elicit host immune responses[103, 7, 104]. These properties make them attractive chassis for programming therapeutic delivery within the tumor microenvironment (TME), where poor vascularization and metabolic heterogeneity limit conventional treatments[105, 106, 63].

Engineering efforts have focused on programming bacteria to release therapeutic agents in a controlled manner. One of the first approaches in the field, the synchronized lysis circuit (SLC), uses quorum sensing to drive pulsatile lysis and release of intracellular payloads[14]. This mechanism of therapeutic delivery also integrated quorum-based population control, serving as a built-in safeguard for bacterial biocontainment[14]. Since this initial design, subsequent efforts have sought to achieve finer spatiotemporal control over therapeutic activity, aiming to restrict bacterial function specifically to tumor tissue[8, 18, 107]. Several complementary strategies have emerged to achieve this localization. TME-responsive promoters have been used to regulate essential genes, thereby enhancing colonization within tumors while reducing growth in healthy tissue[19]. More recently, these same TME-responsive promoters have been linked to lysis functions, localizing therapeutic release to regions of the TME characterized by elevated lactate, hypoxia, and acidity[18]. External control inputs have also been connected to the SLC, but integration of clinically relevant tumor-responsive signals with therapeutic delivery circuits remains limited[59, 108]. Collectively, these strategies established a foundation for microbial cancer therapy, but they rely on fixed genetic architectures and do not account for spatial and temporal heterogeneity across tumors.

The preceding chapters established that conventional plasmid engineering, which relies

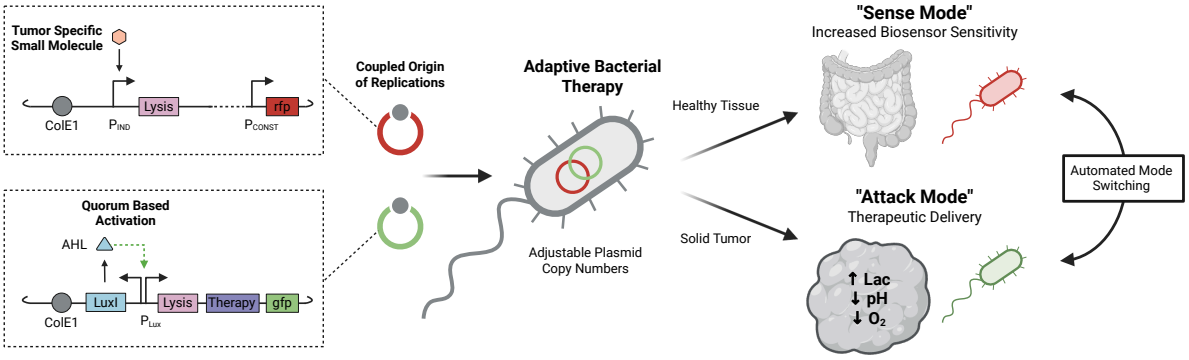


Figure 4.1. Conceptual overview of adaptive bacterial therapy. Schematic representation of a coupled-plasmid framework that regulates therapeutic release within solid tumors. Bacteria dynamically adjust plasmid copy number in response to environmental cues, aligning lysis and therapeutic output with tumor-specific conditions while restricting release outside the TME.

on orthogonal origins of replication to fix copy number and stabilize circuit output, sacrifices the adaptive potential that phenotypic heterogeneity provides. Chapters 2 and 3 demonstrated that coupling two plasmids through a shared origin generates a continuously shifting copy number distribution that organizes into stable spatial structure in response to environmental gradients, and that this behavior is robust across both monolayer microfluidic and physiologically relevant three-dimensional contexts. What remained to be shown is whether that architecture can be directly harnessed for therapeutic function: specifically, whether copy number competition driven by a clinically relevant tumor signal can gate the SLC delivery mechanism in a way that is spatially confined, cyclically self-regulated, and responsive to the metabolic heterogeneity of a solid tumor.

Building on these principles, we present a framework for applying coupled plasmid systems to bacterial cancer therapy. Whereas previous approaches employed TME-responsive promoters to bias colonization[19] or directly drive therapeutic release[18], these designs lacked mechanisms for population-level coordination. Here, we integrate TME signals with cyclical therapeutic delivery using synchronized lysis, and further implement this control within a coupled plasmid framework. This design allows copy-number-mediated phenotypic shifts to align therapeutic output with TME gradients, while also providing built-in safeguards for

biocontainment (Fig. 4.1). By combining environmental sensing, population-level control, and plasmid-based adaptability, this approach expands the toolkit for engineering microbial cancer therapies and establishes a generalizable mechanism for programming spatial and temporal functionality into live bacterial therapeutics.

4.3 Results

4.3.1 Construction of TME-Sensing Reporters and Lactate-Induced Burden

To build strains that functionally respond to the TME, we first constructed and characterized three TME sensing reporter plasmids (Fig. 4.2a). Each plasmid carries a small molecule-responsive promoter upstream of fluorescence expression on a ColE1 origin with spectinomycin resistance (Fig. 4.2b). Here, we employ the lldR, cadC, and FNR bacterial transcription factors, which are regulated by lactate, pH, and oxygen, respectively. FNR and CadC are both transcriptional activators while LldR is a repressor released by lactate. Since LldR is a repressor, we also include constitutive expression of this transcription factor on our plasmid to reduce background GFP expression (Fig. 4.2d). Additionally, to control for oxygen-dependence of GFP folding, FNR constructs drive crLOV expression instead, an oxygen-independent fluorophore. Each sensor strain was grown in 200 µL of LB supplemented with 60 µg/mL spectinomycin and physiological levels of inducer within a Tecan microplate for validation. Our results show increased fluorescence expression across all three constructs when induced, validating promoter sensitivity (Fig. 4.2c). Hypoxia and pH sensor strains imposed measurable growth burdens independent of the encoded lysis circuit, complicating the interpretation of copy number competition dynamics (Fig. 4.2f). Lactate was therefore selected as the model TME signal: it is elevated across the metabolically active tumor core, imposes minimal chassis burden at physiological concentrations, and provides a clean background against which the specifically engineered copy number response can be isolated and characterized (Fig. 4.2e). The lactate sensor exhibits low leak from the pLldR

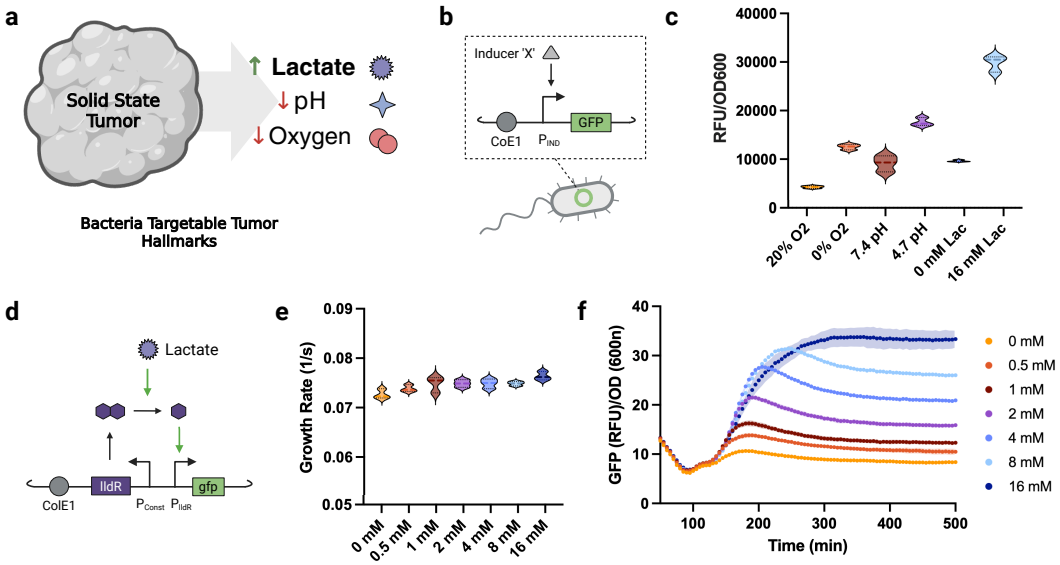


Figure 4.2. Characterization of tumor-microenvironment-responsive biosensors. **(a)** Principal metabolic and chemical hallmarks of solid tumors that inform biosensor design. **(b)** Schematic of a general GFP-reporter circuit in *E. coli* MG1655 used to quantify promoter activity. **(c)** Induction profiles of three biosensors responsive to oxygen, hydrogen, and lactate, showing promoter-specific GFP activation ($n = 3$). **(d)** Circuit diagram of the lactate-inducible biosensor under the lldR promoter driving GFP expression. **(e)** Growth rates of the lactate-responsive strain across increasing lactate concentrations ($n = 3$). **(f)** Time-resolved GFP fluorescence (RFU/OD_{600}) across variable lactate levels ($n = 3$).

promoter and a stepwise fourfold induction between 0 and 16 mM lactate, a dynamic range that, as the following sections demonstrate, is sufficient to drive sharp population-level phenotypic switching when placed within the coupled plasmid framework (Fig. 4.2f).

4.3.2 Lactate-Responsive Copy Number Shifting in the dOri_Lac System

Next, we connected environmental lactate sensing to induced cellular burden by driving expression of the phage lysis protein phiX174E following pLldR (Fig. 4.3a). To optimize lactate sensitivity of the LldR dimer to physiological ranges, we constructed three circuit variants with altered ribosome binding sites upstream of LldR protein expression. We found that a medium-strength RBS led to the strongest lysis response in 20 mM lactate while retaining no induced burden in 0 mM lactate (Fig. 4.3b). For our chosen lactate concentration, the strain with the strongest RBS likely resulted in high levels of dimerized repressor while the weakest did not

produce enough activated monomer.

We then coupled the lactate-inducible lysis plasmid to an analogous arabinose-inducible lysis plasmid on the same ColE1 origin, producing dOri_Lac, a strain in which competing replication burdens drive bidirectional phenotypic adaptation (Fig. 4.3c). This design follows the dual-inducer coupled plasmid architecture described by Kumar et al.[30], with the AHL-responsive plasmid replaced by the lactate-inducible lysis construct. The lactate plasmid carries a constitutive GFP marker and the arabinose plasmid carries RFP, allowing continuous fluorescence-based readout of copy number distribution across the population. Batch culture growth under varied arabinose and lactate concentrations shows that the population shifts copy number to reduce replication burden: under high lactate (32 mM) the population is RFP-dominant, reflecting selective depletion of lactate-plasmid-carrying cells, while under high arabinose (0.02%) and low lactate the population shifts to GFP dominance (Fig. 4.3d). RFP enrichment is detectable across all lactate-positive conditions even in the absence of arabinose, indicating that lactate-driven copy number selection is sufficient to shift population composition without an opposing inducer, a property that makes dOri_Lac potentially responsive to the unidirectional lactate gradients present in vivo.

To visualize how this copy number competition plays out across space and time, we cultured dOri_Lac in a microfluidic gradient device at 20× magnification under opposing gradients of 0.02% arabinose and 8 mM lactate, which generates eight discrete media conditions through branched channel mixing. Within 10 hours, the population diverged spatially, with red-biased cells dominating lactate-containing conditions and green-biased cells concentrated in high-arabinose regions, consistent with the batch culture results (Fig. 4.3e). The high sensitivity to even low lactate concentrations observed in continuous culture may be advantageous for TME detection, where lactate levels span a broad dynamic range across the tumor core and periphery.

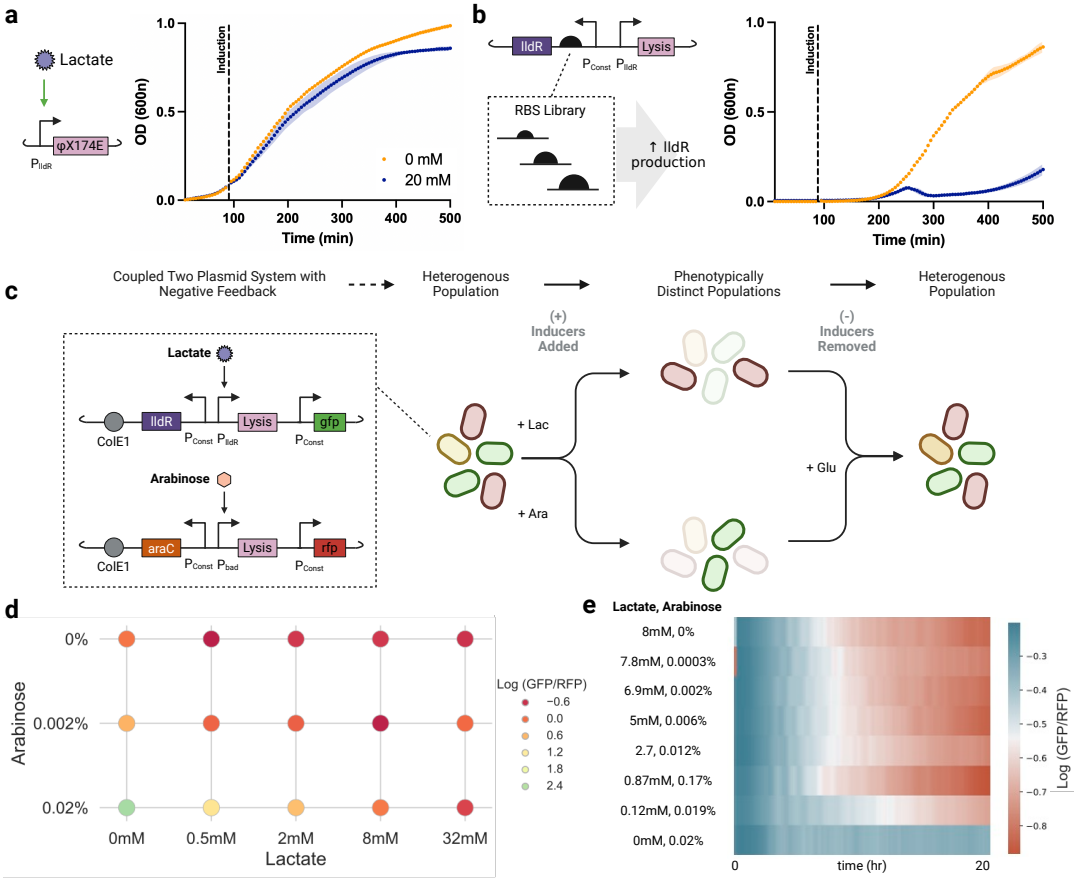


Figure 4.3. Shifting plasmid copy number in response to lactate. **(a)** Genetic circuit schematic of the lactate-inducible lysis module (phiX174 E) and corresponding growth curves (OD_{600}) of *E. coli* MG1655 cultured in 0 mM or 20 mM lactate ($n = 3$). **(b)** Lactate-inducible lysis constructs containing an lldR ribosome-binding-site (RBS) strength library; representative growth dynamics of the strong-RBS variant in 0 mM and 20 mM lactate ($n = 3$). **(c)** Schematic of the coupled two-plasmid system (dOri_Lac) sharing a ColE1 origin of replication, with plasmid 1 encoding lactate-induced lysis and plasmid 2 encoding arabinose-induced lysis. Inducer addition or withdrawal shifts the population between distinct phenotypes. **(d)** Batch-culture fluorescence ratio $\log(\text{GFP}/\text{RFP})$ for dOri_Lac measured across arabinose (%) and lactate (mM) concentrations at time 21.5 hrs ($n = 3$). **(e)** Heatmap quantification of fluorescence ratio $\log(\text{GFP}/\text{RFP})$ over time in continuous microfluidic culture under combined arabinose–lactate gradients.

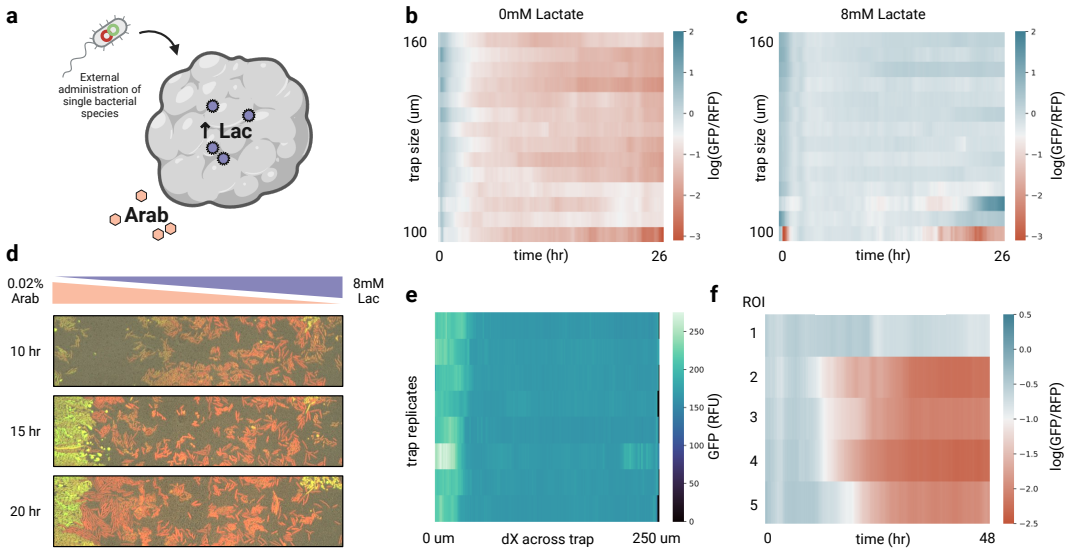


Figure 4.4. Spatial patterning in coupled-origin bacterial populations. **(a)** Illustration of a tumor-relevant lactate gradient and bacterial administration with or without arabinose. **(b–c)** Time-resolved microfluidic fluorescence ratios $\log(\mathrm{GFP}/\mathrm{RFP})$ of dOri_Lac grown in 0 mM (b) or 8 mM (c) lactate across traps of varying widths ranging from 160 µm to 100 µm in 10 µm increments. **(d)** Transmitted-light, GFP, and RFP fluorescence images collected at 10 h, 15 h, and 20 h under opposing continuous gradients ($8 \rightarrow 0$ mM lactate; $0 \rightarrow 0.02\%$ arabinose). **(e)** GFP fluorescence intensity as a function of trap length at 48 hrs from the gradient run. **(f)** Mean fluorescence ratio $\log(\mathrm{GFP}/\mathrm{RFP})$ across $n = 8$ replicates, averaged from five equally spaced regions of interest spanning each trap.

4.3.3 Spatial Patterning to Discrete and Continuous Lactate Gradients

To test whether dOri_Lac responds to lactate gradients without exogenous arabinose, conditions more representative of in vivo administration, we cultured the strain across 0 to 8 mM lactate in a discrete gradient device with varied trap sizes. The GFP-to-RFP ratio shows clear red dominance in high lactate and green dominance in the absence of lactate across all trap sizes examined (Fig. 4.4b,c). Smaller traps exhibited greater phenotypic variability than larger ones, consistent with the expectation that competitive copy number dynamics require sufficient population size for fitness differences to drive stable phenotypic separation. In the TME, lactate gradients are continuous rather than discrete, with a metabolically active tumor core serving as the source and well-perfused peripheral tissue acting as a sink. To recapitulate this geometry, we cultured dOri_Lac in a continuous gradient device in which opposing channels supply 8 mM lactate and 0.02% arabinose across a long trap geometry (Fig. 4.1a). A segmented spatial pattern emerged within 16 hours: green-biased cells accumulated within the first 50 μm of the arabinose-proximal end while red-biased cells occupied the remaining 200 μm (Fig. 4.4d–f). The narrow zone of green bias likely reflects higher lactate diffusivity relative to arabinose and the steep induction response of the lactate lysis plasmid. That dOri_Lac produces stable, spatially organized phenotypic structure across a continuous chemical gradient without additional regulatory circuitry sets the stage for the therapeutic application developed in the following section: replacing the arabinose sensing plasmid with the SLC so that the same lactate-driven copy number shift actively gates cyclical therapeutic delivery.

4.3.4 Functional Modulation of Delivery Strains in Response to Lactate

With the goal of developing a functionally adaptive strain for delivery within the heterogeneous TME, we next coupled our inducible lysis plasmids to a synchronized lysis circuit (SLC) (Fig. 4.5a). The SLC drives cycles of population-coordinated lysis for periodic therapeutic delivery. We used a single-plasmid version of the SLC constructed by Lezia et al.[109], which

has the AHL-responsive pLux promoter driving both lysis and AHL synthase, LuxI. The LuxR transcriptional regulator is weakly expressed in reverse from the same pLux promoter. This construct allows for production of the quorum molecule AHL6 with positive feedback until a certain population density is reached, leading to lysis and subsequent reseeding of the population. When this SLC plasmid is coupled with an environmentally inducible lysis plasmid on the same ColE1 origin, we hypothesize that the strain will diverge into two functionally distinct phenotypes: a cyclical delivery mode and a sensing mode (Fig. 4.5d). In the presence of environmental signal, cells with high copy number of the sensing plasmid will die, leading to dominance by the SLC plasmid and the delivery phenotype. In the absence of biomarker, the low-burden sensing plasmid will dominate the population instead, yielding increased sensitivity and no SLC-driven delivery.

To test this two-plasmid circuit design, we first coupled the arabinose-inducible lysis plasmid to the SLC to produce dOri_SLC-A. Batch culture OD measurements showed lysis of dOri_SLC-A in both 0.02% arabinose and no-inducer conditions but no lysis in 0.2% glucose (Fig. 4.3). Additionally, constitutive RFP expression by the arabinose lysis plasmid in this strain was low in arabinose media and glucose media but high in the no-inducer condition. These results suggest that without inducer the arabinose lysis plasmid is dominant across the population while in both glucose and arabinose media the SLC plasmid is instead dominant (Fig. 4.3). Glucose suppresses SLC-driven lysis, consistent with known catabolite repression of the *plux* promoter [109], allowing the SLC plasmid to dominate the population without driving delivery in this condition. When cultured in arabinose, cells containing high copy number of the arabinose lysis plasmid died, leading to takeover of the SLC phenotype as expected.

We showed proof-of-principle that an environmental sensor plasmid driving cell lysis can drive functional modulation of a delivery strain when the plasmid is coupled to the SLC. We then replaced the arabinose lysis plasmid in this coupled strain with the lactate lysis plasmid to demonstrate functional modulation in response to a relevant biomarker within the TME. To this end, we modified our lactate lysis plasmid to constitutively express red fluorescence, since

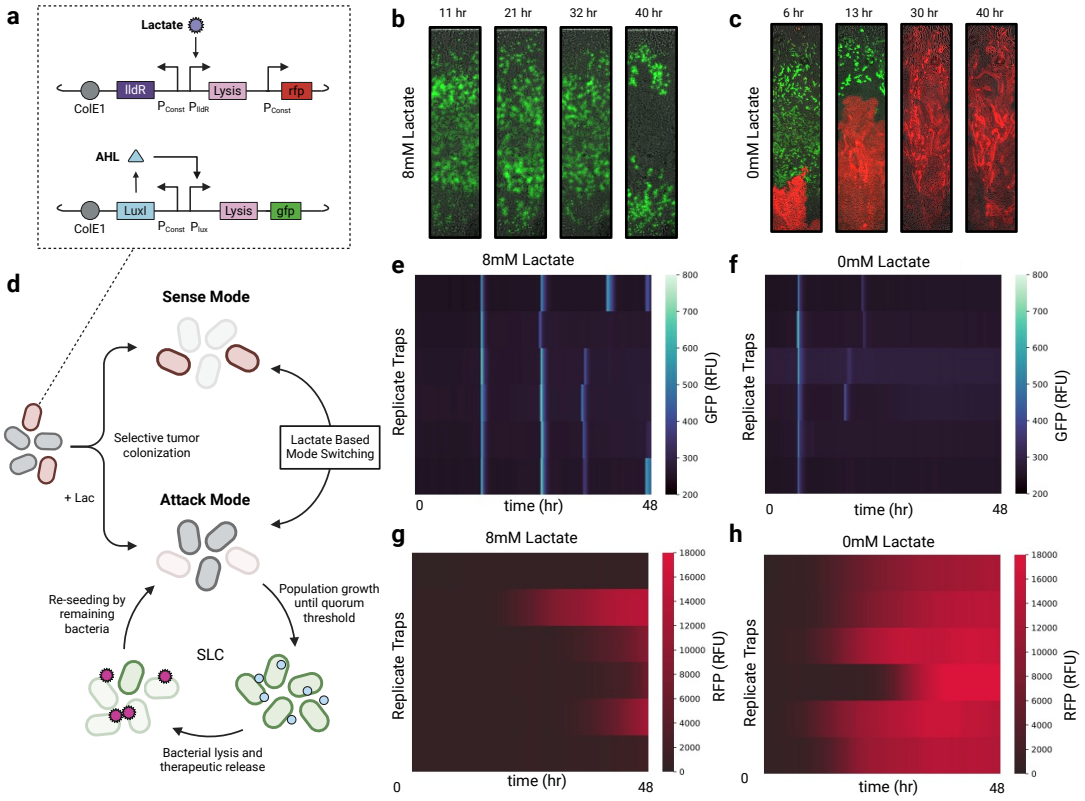


Figure 4.5. Lactate-induced synchronized lysis circuit. **(a)** Genetic circuit integrating lactate-inducible lysis with the synchronized lysis circuit (SLC), both operating from a shared ColE1 origin of replication. **(b–c)** Microfluidic stills of dOri_SLC showing population-wide lysis events in 8 mM lactate (b) and biosensor maintenance in 0 mM lactate (c). **(d)** Conceptual schematic depicting switch between high-copy biosensor and active therapeutic states within a heterogeneous population governed by lactate concentration. **(e–h)** Microfluidic fluorescence quantification of GFP (e–f) and RFP (g–h) signals over time in 8 mM and 0 mM lactate, illustrating synchronized cycles of lysis and recovery.

the SLC plasmid drives quorum-triggered GFP. After co-transforming these two plasmids, we first tested this strain within the variable trap size gradient device. In 0 mM lactate media, larger capacity traps were taken over by the red sensing phenotype following 1–2 lysis cycles. In 8 mM lactate, however, the population died out following 1 lysis cycle (Fig. 4.4). To improve population re-seeding for robust cycling, we next cultured our coupled strain within a microfluidic device with extended 50 by 250 μm cell chambers. In this device, the strain was capable of at least 3–4 cycles within a 48-hour run time (Fig. 4.5b,e). Confirming our prior findings, in 0 mM lactate the population underwent a single early lysis event within the first 16 hours, after which the red sensing phenotype stably dominated, consistent with sensor plasmid takeover in the absence of lactate-driven selection pressure (Fig. 4.5e,f,h). These results demonstrate the ability of our system to regulate delivery as a function of local biomarkers and gradients. Using this plasmid system, the lactate-producing core of a tumor would receive sustained therapeutic delivery while low-lactate outer or off-target regions would retain cells in biomarker sensing mode.

4.4 Discussion

This work establishes a framework for programming adaptive therapeutic behaviors in bacteria through coupled plasmid systems that respond to tumor-associated environmental cues. By linking plasmid copy number dynamics to lactate-inducible gene expression and synchronized lysis, we demonstrate that a single bacterial population can autonomously transition between sensing and delivery modes in response to spatial metabolic gradients representative of the TME. These findings illustrate how plasmid-level coupling, traditionally viewed as a source of instability, can instead serve as a powerful design element for achieving environmental plasticity and population-level coordination in live therapeutics.

Recent work has demonstrated the construction of synthetic differentiating populations in bacterial and mammalian cell communities, producing multifunctional subpopulations through programmed cell-cell interactions and transcriptional circuit logic[110, 111, 112]. Those systems

typically require dedicated signaling architectures to specify each functional state. The approach described here differs in that phenotypic differentiation is not encoded at the level of gene regulation but emerges from fitness-mediated competition between plasmids sharing a replication origin. Environmental signals do not instruct cells to adopt a particular state; they alter the selective landscape such that one plasmid copy number ratio becomes more viable than another. The result is a population that self-organizes in response to continuous gradients rather than discrete thresholds, and whose functional composition tracks the spatial metabolic structure of the tumor without requiring an explicit sensing-and-response circuit for each phenotypic output.

The ability to couple therapeutic release with local biomarkers addresses a major limitation of earlier microbial therapy platforms, which often relied on constitutive or externally triggered lysis[14, 8]. Bacteria serve as excellent whole-cell biosensors capable of detecting disease-biased metabolites, DNA markers, and numerous chemical signatures[113, 101, 114]. While promoter-driven sensing architectures have improved localization, they remain constrained by fixed genetic contexts and lack mechanisms for balancing multiple functional states[107, 8, 115]. Integrating these circuits within a coupled-origin framework enables generation of population copy number heterogeneity, effectively distributing distinct circuit modes across a population[30, 47]. This property allows bacteria to sense and adapt to continuous tumor gradients rather than binary environmental inputs, aligning their functional heterogeneity with the physiological heterogeneity observed in solid tumors. By embedding the synchronized lysis circuit within this framework, therapeutic delivery becomes both environmentally informed and cyclically coordinated, providing a built-in safeguard for biocontainment and improved temporal control.

Beyond demonstrating functional modulation, this work builds upon a broader conceptual advance: the use of copy-number-mediated feedback as an additional layer of regulation orthogonal to transcriptional or translational control[116, 26, 46, 117]. Plasmid coupling expands the design space of genetic circuits, offering a tunable mechanism for encoding dynamic equilibria between competing modules. In therapeutic contexts, such behavior could enable live microbial

populations to self-organize spatially, allocate metabolic resources adaptively, and sustain activity over clinically relevant timescales. These properties mirror the distributed decision-making strategies observed in natural microbial communities, suggesting that population heterogeneity may be leveraged to improve robustness and therapeutic efficacy of synthetic systems[118, 119, 120].

4.5 Materials and Methods

4.5.1 Cell Culturing

All plasmids were transformed into *E. coli* strain MG1655. Strains were cultured in lysogeny broth (LB) with appropriate antibiotic selection (20 μg mL^{-1} chloramphenicol, 60 μg mL^{-1} spectinomycin) in a 37°C shaker. For DNA validation, plasmid sequencing was conducted on all constructs within the study. Low pH media was created by adding HCl until pH measured at 4.7. Hypoxic media was created using a cupric sulfate quencher system with microwells sealed using optically clear film. Lactate was added to standard media using a 60% potassium lactate solution.

4.5.2 Anaerobic Cell Culturing

Two orthogonal approaches were used to deplete environmental oxygen when culturing strains. Thermo Scientific AnaeroPack-Anaero Anaerobic Gas Generator packages were used in an airtight container to replicate conditions of a traditional anaerobic chamber[121]. Cell cultures were prepared as noted above then air sealed in a container with both the AnaeroPack and an additional oxygen sensing strip to ensure no oxygen leaks were present. For real-time monitoring of strains outside of the chamber, standard media was supplemented with 1% sodium sulfite and 100 μM cobalt for oxygen depletion[93].

4.5.3 Microfluidic Runs

Microfluidic devices were fabricated from PDMS following established soft lithography protocols similar to those described previously by our group. PDMS was poured over a silicon

wafer patterned with micron-scale channel features defined by cross-linked photoresist and cured at 65°C for approximately 12 hours. The polymerized PDMS was then peeled from the master mold, and individual devices were cut and punctured to form inlet and outlet ports. Devices were bonded to glass coverslips using plasma activation and subsequently mounted on an inverted microscope stage for cell loading and imaging.

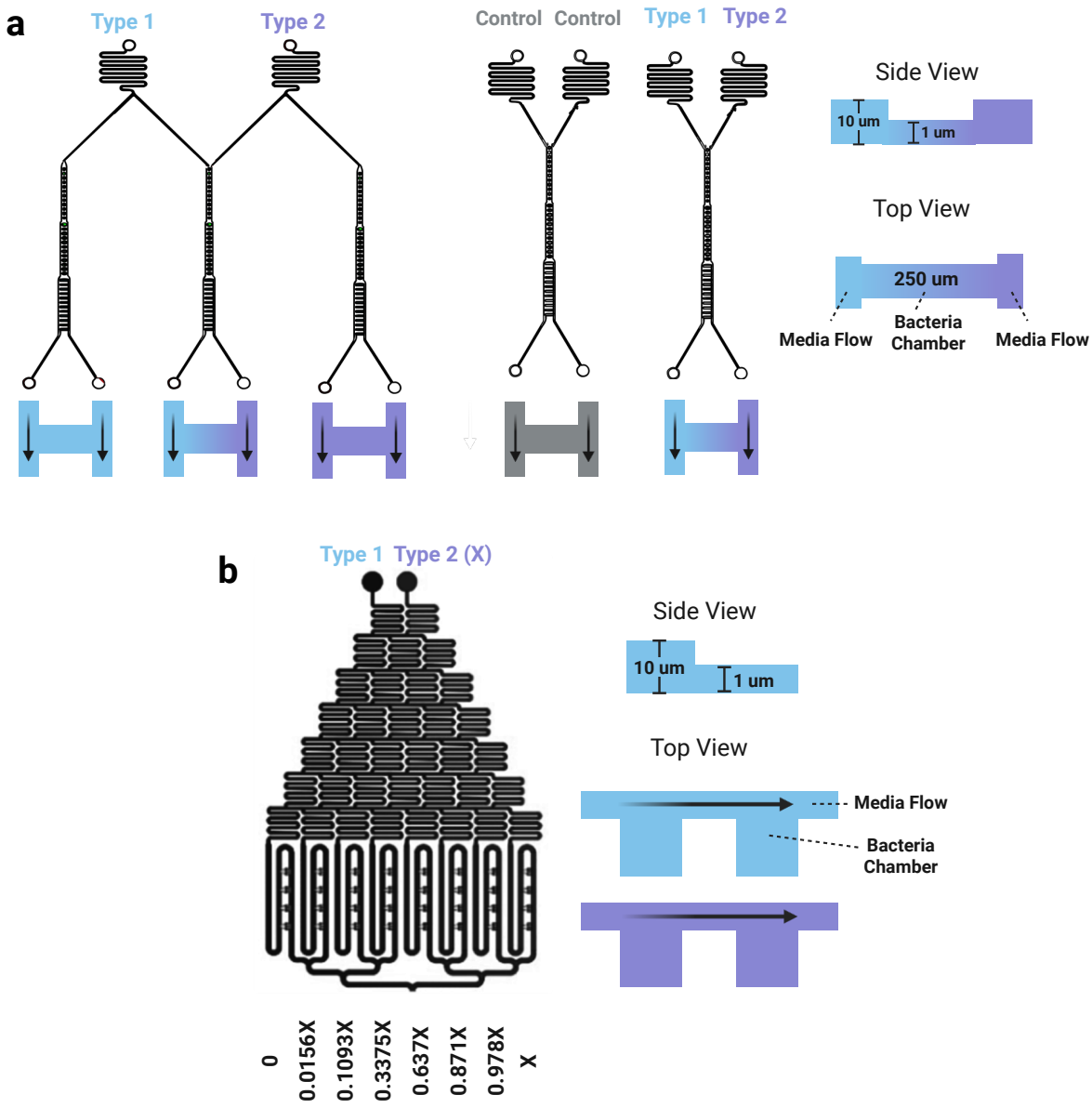
Prior to use, devices were degassed for 45 minutes in a vacuum chamber. Following degassing, 10 µL droplets of bacterial suspension were placed on the outlet ports and 10 µL droplets of sterile medium were added to the inlets to initiate flow by capillary action. The medium consisted of LB supplemented with appropriate antibiotics and one of three conditions: no additive, 8 mM lactate, or 0.02% arabinose. Tween 20 (0.075%) was included in all media to prevent cell adhesion to PDMS channel surfaces. Once wetted, the devices were connected to syringes supplying fresh medium or waste collection, and hydrostatic pressure was controlled by adjusting relative syringe heights to generate passive flow across the chamber.

All imaging was performed on a Nikon Ti-2 inverted microscope housed within a temperature-controlled (37°C) plexiglass incubation chamber. Phase-contrast images were acquired at 20× magnification. Fluorescence was captured with exposure settings of 50 ms at 50% illumination for mCherry and 40 ms at 50% for GFP. Images were collected every 10 minutes throughout each experiment.

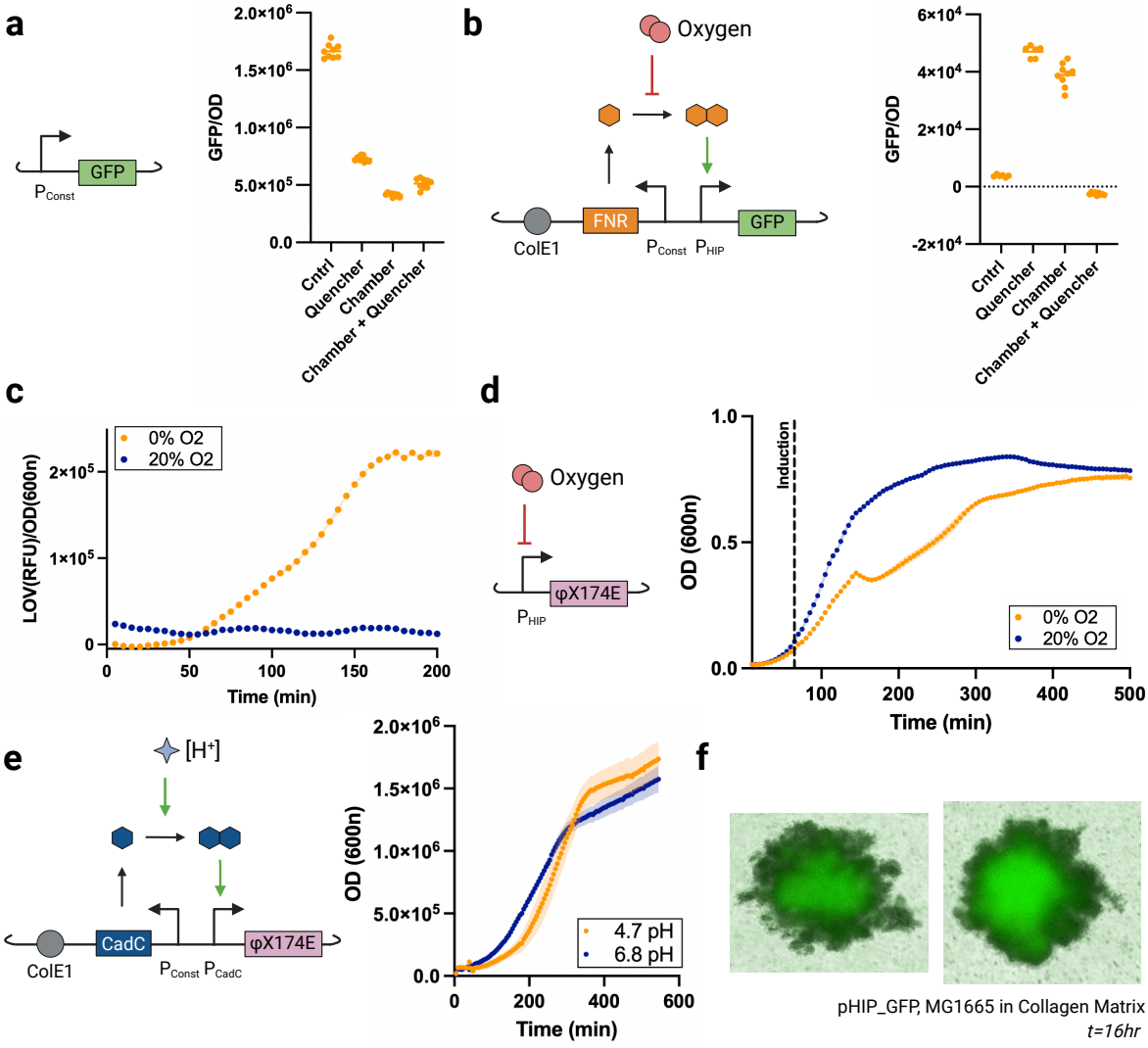
4.5.4 Data Analysis

Fluorescence intensity profiles were obtained by analyzing frames with ImageJ from the fluorescent channel recorded on the Nikon Ti-2. Growth rates were calculated in GraphPad Prism by fitting the exponential phase of OD_{600} growth curves to a nonlinear regression model using an exponential growth equation.

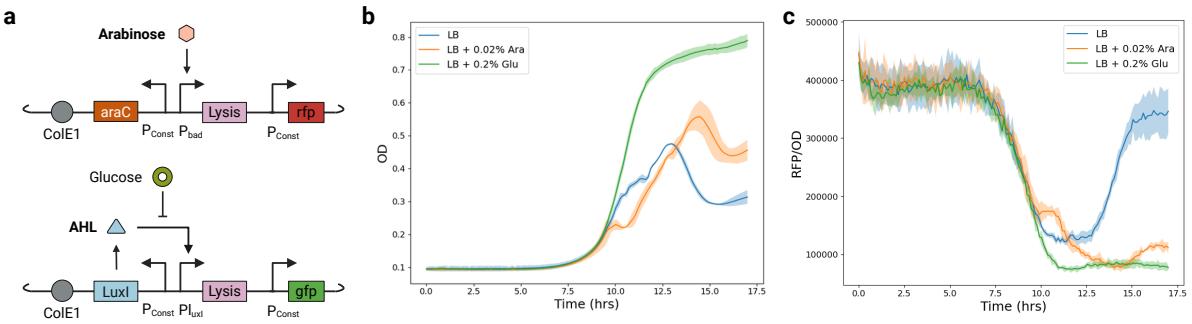
4.6 Supplemental Figures



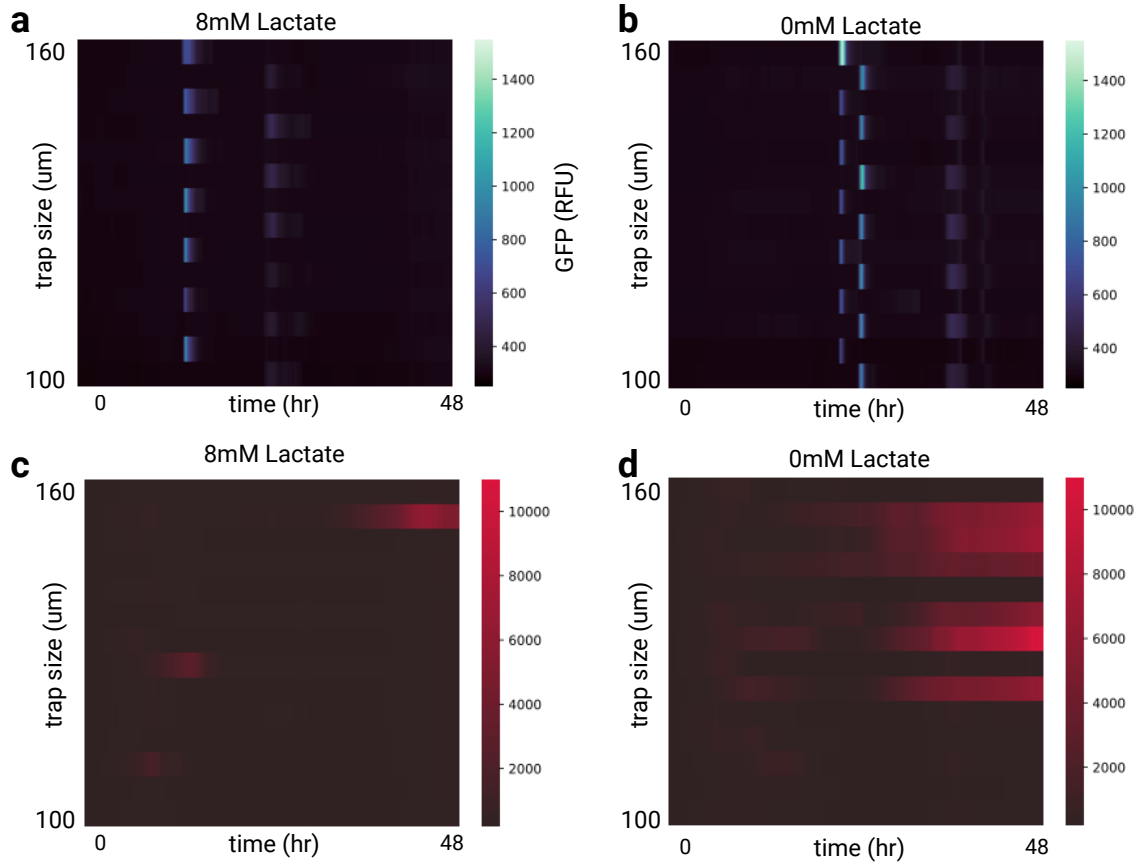
Supplemental Figure 4.1. Microfluidic chip design and fabrication details for Chapter 4 experiments. Includes device schematics for the discrete gradient chip and continuous gradient chip configurations used for dOri_Lac and dOri_SLC patterning experiments.



Supplemental Figure 4.2. Additional TME biosensor construction and validation data. Includes characterization of hypoxia and pH sensor strains and growth impact analysis across TME-relevant inducer concentrations.



Supplemental Figure 4.3. dOri_SLC-A batch culture characterization. OD_{600} and fluorescence measurements of the arabinose-lysis plasmid coupled to the SLC in arabinose, glucose, and no-inducer conditions, demonstrating SLC plasmid dominance under glucose repression and arabinose-lysis plasmid dominance in the absence of inducer.



Supplemental Figure 4.4. dOri_SLC behavior in variable trap size gradient device. In 0 mM lactate, larger capacity traps were taken over by the red sensing phenotype following 1–2 lysis cycles. In 8 mM lactate, the population failed to sustain continuous cycling in all tested trap sizes, motivating the use of extended 50 × 250 µm chambers for robust delivery cycling.

Chapter 4, in full, is currently being prepared for submission for publication of the material. Steppe, P., Kumar, S.*, Erkok, D., Tayal, A., and Hasty, J. Adaptive therapeutic delivery through plasmid coupling in bacteria. Genome Biology (2026, Submitted). The dissertation author was the primary investigator and author of this paper.*

Chapter 5

General Discussion

The central premise of this dissertation is that bacterial populations do not need to be uniformly programmed to perform complex therapeutic functions. They need to be given the right conditions to differentiate. This distinction matters because the field of engineered bacterial therapeutics has largely operated under the assumption that tighter genetic control produces better outcomes: orthogonal origins of replication to fix copy number, constitutive promoters to guarantee expression, well-mixed culture conditions to eliminate spatial variability. Each of these choices reflects a reasonable engineering instinct, but collectively they produce systems that are maximally brittle at exactly the point where robustness is most needed, inside a living tumor.

The three chapters of this dissertation develop an alternative design philosophy grounded in a single architectural choice: coupling two plasmids through a shared origin of replication. This choice introduces heritable copy number heterogeneity into the population, not as a side effect to be managed, but as the primary regulatory mechanism. The result is a system in which phenotypic diversity is generated continuously, selection pressure from the local environment determines which phenotype dominates, and the population retains memory of its most recent environmental state through plasmid inheritance. No additional sensors, no toggle switches, no transcriptional logic gates. The architecture itself performs the computation.

5.1 From Controlled Clones to Adaptive Populations

The standard synthetic biology paradigm treats genotypic uniformity as a prerequisite for predictable function. Engineering a bacterial population to perform a specific task begins with minimizing sources of variation: identical plasmid copy numbers, tightly regulated promoters, antibiotic selection to eliminate non-producers. Chapter 2 demonstrates that deliberately violating this principle, by introducing copy number heterogeneity through duplicate origins of replication, produces a qualitatively different kind of functional output. Rather than a population of identical effectors, the dOri_AHL strain generates a distribution of phenotypic states whose spatial organization is determined by the chemical gradients present in the local environment. Distinct subpopulations emerge and stabilize across opposing inducer gradients within hours, and this organization persists long after the inducing signal is removed, reflecting a form of population-level memory that does not require dedicated bistable circuitry.

This behavior is ecologically familiar: it is a synthetic instantiation of bet-hedging, where phenotypic diversity across a clonal population distributes risk across environments and ensures that some fraction of cells is pre-adapted to whatever conditions emerge. What Chapter 2 adds to the existing coupled plasmid literature is the spatial dimension. Prior work established that copy number heterogeneity enables adaptive burden minimization in well-mixed conditions[30]. The microfluidic gradient experiments demonstrate that this same heterogeneity can be organized into stable spatial structure by environmental gradients, transforming a population-level statistical property into a spatially resolved functional architecture. The coupled plasmid system can therefore translate the chemical geography of a complex environment directly into a corresponding phenotypic geography, without any additional sensing or regulatory circuitry.

5.2 Physiological Context as a Design Variable

A persistent gap in the bacterial therapeutics literature is the disconnect between *in vitro* characterization and *in vivo* performance. Circuits that behave predictably in batch culture

or microfluidic monolayers routinely fail to reproduce those dynamics in animal models, and the mechanisms underlying this discrepancy have been difficult to dissect because no existing platform can systematically vary physiological parameters while maintaining single-colony resolution of circuit output. Chapter 3 addresses this gap directly, and its most important finding is not any single result about a specific circuit but the broader demonstration that the physical microenvironment is an active regulator of circuit behavior rather than a passive backdrop.

Three-dimensional growth in an extracellular matrix decouples bacterial colony dynamics from the overcrowding artifacts of confined monolayer culture, allowing population density to accumulate and AHL to diffuse on timescales that more closely approximate the spatial scale of a solid tumor. This shift in physical context is what drives the SLC period from approximately 5 hours in 2D monolayer microfluidics toward approximately 16 hours in collagen under hypoxia, approaching the range observed in murine tumor models. The testbed does not just recapitulate *in vivo* dynamics; it resolves the mechanism that produces them: oxygen-dependent growth rate modulation propagating as a wave of AHL-driven SLC activation across a centimeter-scale tissue analog.

The dOri_AHL strain results in Chapter 3 extend this finding to the coupled plasmid architecture. Phenotypic patterning persists in the three-dimensional collagen environment across a 10 mm spatial domain, establishing that the copy number competition mechanism underlying Chapter 2 is not an artifact of the monolayer geometry. The dOri_AHL strain organizes into spatially stable GFP- and RFP-dominant subpopulations across opposing inducer gradients in collagen on a timescale comparable to the monolayer experiments, despite the substantially different physical constraints. This robustness across experimental contexts is a necessary condition for the therapeutic application developed in Chapter 4, and Chapter 3 establishes it directly rather than assuming it.

5.3 Adaptive Delivery through Copy Number Competition

Chapter 4 applies the coupled plasmid framework to a fully integrated therapeutic design, and the result is qualitatively different from what promoter-based sensing approaches have achieved. Previous strategies for tumor-restricted bacterial therapy have linked TME-responsive promoters to essential genes or lysis functions, achieving a degree of spatial localization but operating in a fixed genetic mode: the circuit is on or off depending on whether the environmental threshold is crossed, and the same genetic architecture governs behavior in both states[19, 18]. The dOri_Lac and dOri_SLC systems do not work this way. In the presence of lactate, copy number competition selects for cells dominated by the SLC plasmid, driving population-coordinated therapeutic lysis. In the absence of lactate, the sensing plasmid dominates, and the population maintains a high-copy biosensor state with no SLC-driven delivery. The transition between these states is a continuous, reversible shift in the copy number distribution that tracks the local lactate concentration.

What makes this behavior particularly notable is that it achieves sharp phenotypic switching despite modest promoter sensitivity. The pLldR promoter produces only a fourfold change in expression between 0 and 16 mM lactate, a dynamic range that would be considered inadequate for most sense-and-respond circuit designs. Yet when this promoter drives lysis in the context of copy number competition, the population shows clear all-or-nothing phenotype switching: sensing-plasmid dominance at low lactate and SLC-plasmid dominance at high lactate, with minimal intermediate states. The coupled plasmid architecture amplifies a weak transcriptional signal into a discrete population-level switch through the nonlinear dynamics of fitness-based selection, allowing the system to exploit a promoter that no fixed-architecture design could use effectively. The practical implication is that the choice of inducible promoter is no longer constrained by its intrinsic dynamic range, substantially expanding the set of TME signals that can be used to gate therapeutic function.

The functional consequence of this architecture is that the two states reinforce each

other in a way that purely transcriptional designs cannot replicate. In the sensing-dominant state, elevated copy number of the lactate-responsive plasmid increases the sensitivity of the population to lactate, so cells in the sensing state become increasingly primed to detect the very signal that will push them into delivery mode. This adaptive gain property emerges without dedicated feedback circuitry because the regulatory variable and the functional output are the same quantity: copy number. A population carrying more copies of the sensor is simply a better sensor, and that improvement in sensitivity is what closes the loop.

The dOri_SLC system also provides a natural solution to the biocontainment problem that has complicated bacterial therapeutics since the earliest clinical studies. The SLC's pulsatile lysis mechanism already constrains bacterial accumulation through periodic population reset. The coupled plasmid architecture adds a second layer: outside the lactate-rich tumor core, the sensing plasmid dominates and SLC-driven lysis does not occur. The therapeutic activity of the strain is therefore gated both temporally by quorum dynamics and spatially by metabolic context, without requiring dedicated kill switches or auxotrophies that introduce additional evolutionary escape routes.

5.4 Generalizability and Future Directions

The framework developed in this dissertation is not specific to lactate or to colorectal cancer. The lactate-responsive pLldR promoter was chosen because it is well-characterized, physiologically relevant to solid tumors broadly, and imposes minimal growth burden on the chassis at the concentrations tested. Any inducible promoter that drives a metabolic burden through lysis, growth arrest, or resource-intensive expression should generate the same copy number competition dynamics when placed on a shared-origin plasmid coupled to the SLC construct. Critically, this principle is also not restricted to any particular origin of replication. The duplicate origin architecture functions across replication classes, including ColE1, p15a, pUC, and SC101 variants, meaning the design framework is accessible with standard cloning backbones

without requiring custom replication machinery[30]. What matters is that the environmental signal modulates the relative fitness cost of carrying one plasmid over the other, and that this fitness differential is large enough to drive population-level copy number shifts. That condition can be satisfied across a wide range of promoters, chassis, and target environments.

The most immediate experimental priority is validating dOri_Lac and dOri_SLC patterning behavior in three-dimensional tumor models. The data in Chapter 4 establish the circuit dynamics in microfluidic culture; the testbed platform developed in Chapter 3 provides a direct path to characterizing those dynamics under physiological oxygen gradients and extracellular matrix architecture. Spheroid co-culture experiments with the dOri_Lac and dOri_SLC strains would allow direct quantification of copy number-dependent patterning and lysis dynamics at a spatial scale directly analogous to early-stage colorectal tumors, and would provide the *in vitro* validation needed before committing to animal experiments.

Beyond the therapeutic context, the coupled plasmid architecture has broader implications for how synthetic biologists approach circuit stability under evolutionary pressure. Designing synthetic systems that harness copy number competition rather than suppressing it offers a path to circuits that are more reliable not because they resist evolutionary pressure but because they channel it productively. This principle extends well beyond bacterial cancer therapy. In environmental bioremediation, a single engineered strain could allocate metabolic investment between pollutant sensing and degradation activity in response to local contaminant concentration, self-organizing into functional spatial zones within a contaminated soil matrix without external coordination. In bioproduction, coupled plasmid systems could distribute metabolic load across a fermentation population dynamically, shifting the balance between biosynthetic pathway expression and growth maintenance as substrate availability fluctuates. In living diagnostics, the sensing-dominant state's enhanced detection sensitivity could be exploited to lower detection thresholds for disease biomarkers in complex biological samples, with the circuit automatically shifting into a reporting mode once signal exceeds a fitness-defined threshold. In each of these cases, the coupled plasmid architecture offers something that fixed-design circuits cannot: a

population whose functional organization continuously adapts to the environment it actually encounters rather than the environment it was designed for.

Bibliography

[1] Andriy Marusyk, Michalina Janiszewska, and Kornelia Polyak. Intratumor heterogeneity: the rosetta stone of therapy resistance. *Cancer cell*, 37(4):471–484, 2020.

[2] Kimberly D Miller, Leticia Nogueira, Angela B Mariotto, Julia H Rowland, K Robin Yabroff, Catherine M Alfano, Ahmedin Jemal, Joan L Kramer, and Rebecca L Siegel. Cancer treatment and survivorship statistics, 2019. *CA: a cancer journal for clinicians*, 69(5):363–385, 2019.

[3] Douglas Hanahan. Hallmarks of cancer: new dimensions. *Cancer discovery*, 12(1):31–46, 2022.

[4] Susy M Kim, Peggy H Faix, and Jan E Schnitzer. Overcoming key biological barriers to cancer drug delivery and efficacy. *Journal of Controlled Release*, 267:15–30, 2017.

[5] Triantafyllos Stylianopoulos and Rakesh K Jain. Combining two strategies to improve perfusion and drug delivery in solid tumors. *Proceedings of the National Academy of Sciences*, 110(46):18632–18637, 2013.

[6] Mohammad Amin Manavi, Mohammad Hosein Fathian Nasab, Razieh Mohammad Jafari, and Ahmad Reza Dehpour. Mechanisms underlying dose-limiting toxicities of conventional chemotherapeutic agents. *Journal of Chemotherapy*, 36(8):623–653, 2024.

[7] Mai Thi-Quynh Duong, Yeshan Qin, Sung-Hwan You, and Jung-Joon Min. Bacteria-cancer interactions: bacteria-based cancer therapy. *Experimental & molecular medicine*, 51(12):1–15, 2019.

[8] Candice R Gurbatri, Nicholas Arpaia, and Tal Danino. Engineering bacteria as interactive cancer therapies. *Science*, 378(6622):858–864, 2022.

[9] William B Coley. The treatment of malignant tumors by repeated inoculations of erysipelas: With a report of ten original cases. 1. *The American Journal of the Medical Sciences (1827-1924)*, 105(6):487, 1893.

[10] Sebastian Felgner, Dino Kocijancic, Michael Frahm, and Siegfried Weiss. Bacteria in cancer therapy: renaissance of an old concept. *International journal of microbiology*, 2016(1):8451728, 2016.

[11] Edward R Ballister, Alexander Michels, Rosa L Vincent, Lior Kreindler, Sreyan Chowdhury, Samik Upadhaya, Ana Rosa Saez-Ibañez, Tao Tu, Juraj Gottweis, and Tal Danino. The emerging landscape of engineered bacteria cancer therapies. *Nature Biotechnology*, pages 1–5, 2025.

[12] Ming Q Wei, Asferd Mengesha, David Good, and Jozef Anné. Bacterial targeted tumour therapy-dawn of a new era. *Cancer letters*, 259(1):16–27, 2008.

[13] Ming Q Wei, Kay AO Ellem, Paul Dunn, Malcolm J West, Chun Xue Bai, and Bert Vogelstein. Facultative or obligate anaerobic bacteria have the potential for multimodality therapy of solid tumours. *European journal of cancer*, 43(3):490–496, 2007.

[14] M Omar Din, Tal Danino, Arthur Prindle, Matt Skalak, Jangir Selimkhanov, Kaitlin Allen, Ellixis Julio, Eta Atolia, Lev S Tsimring, Sangeeta N Bhatia, et al. Synchronized cycles of bacterial lysis for in vivo delivery. *Nature*, 536(7614):81–85, 2016.

[15] Sara Sadr, Bahram Zargar, Marc G Aucoin, and Brian Ingalls. Construction and functional characterization of a heterologous quorum sensing circuit in clostridium sporogenes. *bioRxiv*, pages 2025–08, 2025.

[16] Andrew Redenti, Jongwon Im, Benjamin Redenti, Fangda Li, Mathieu Rouanne, Zeren Sheng, William Sun, Candice R Gurbatri, Shunyu Huang, Meghna Komaranchath, et al. Probiotic neoantigen delivery vectors for precision cancer immunotherapy. *Nature*, 635(8038):453–461, 2024.

[17] Candice R Gurbatri, Georgette A Radford, Laura Vrbanac, Jongwon Im, Elaine M Thomas, Courtney Coker, Samuel R Taylor, YoungUk Jang, Ayelet Sivan, Kyu Rhee, et al. Engineering tumor-colonizing e. coli nissle 1917 for detection and treatment of colorectal neoplasia. *Nature Communications*, 15(1):646, 2024.

[18] Tuoyu Zhou, Jingyuan Wu, Haibo Tang, Dali Liu, Byong-Hun Jeon, Weilin Jin, Yiqing Wang, Yuanzhang Zheng, Aman Khan, Huawen Han, et al. Enhancing tumor-specific recognition of programmable synthetic bacterial consortium for precision therapy of colorectal cancer. *npj Biofilms and Microbiomes*, 10(1):6, 2024.

[19] Tiffany Chien, Tetsuhiro Harimoto, Benjamin Kepecs, Kelsey Gray, Courtney Coker, Nicholas Hou, Kelly Pu, Tamjeed Azad, Andoni Nolasco, Martina Pavlicova, et al. Enhancing the tropism of bacteria via genetically programmed biosensors. *Nature biomedical engineering*, 6(1):94–104, 2022.

[20] Hye-In Son, Andrea Weiss, and Lingchong You. Design patterns for engineering genetic stability. *Current opinion in biomedical engineering*, 19:100297, 2021.

[21] Daniel M Stoebel, Antony M Dean, and Daniel E Dykhuizen. The cost of expression of escherichia coli lac operon proteins is in the process, not in the products. *Genetics*, 178(3):1653–1660, 2008.

[22] Ruth Grady and Finbarr Hayes. Axe–txe, a broad-spectrum proteic toxin–antitoxin system specified by a multidrug-resistant, clinical isolate of enterococcus faecium. *Molecular microbiology*, 47(5):1419–1432, 2003.

[23] Alex JH Fedorec, Tanel Ozdemir, Anjali Doshi, Yan-Kay Ho, Luca Rosa, Jack Rutter, Oscar Velazquez, Vitor B Pinheiro, Tal Danino, and Chris P Barnes. Two new plasmid post-segregational killing mechanisms for the implementation of synthetic gene networks in escherichia coli. *Iscience*, 14:323–334, 2019.

[24] Jean-Yves Bouet and Barbara E Funnell. Plasmid localization and partition in enterobacteriaceae. *EcoSal Plus*, 8(2):10–1128, 2019.

[25] Tanita Wein, Yiqing Wang, Myriam Barz, Fenna T Stücker, Katrin Hammerschmidt, and Tal Dagan. Essential gene acquisition destabilizes plasmid inheritance. *PLoS Genetics*, 17(7):e1009656, 2021.

[26] Shivang Hina-Nilesh Joshi, Chentao Yong, and Andras Gyorgy. Inducible plasmid copy number control for synthetic biology in commonly used e. coli strains. *Nature communications*, 13(1):6691, 2022.

[27] Zhijun Wang, Li Jin, Zhenghong Yuan, Grzegorz Wegrzyn, and Alicja Wegrzyn. Classification of plasmid vectors using replication origin, selection marker and promoter as criteria. *Plasmid*, 61(1):47–51, 2009.

[28] Nileena Velappan, Daniele Sblattero, Leslie Chasteen, Peter Pavlik, and Andrew RM Bradbury. Plasmid incompatibility: more compatible than previously thought? *Protein engineering, design & selection*, 20(7):309–313, 2007.

[29] Weixin Tang and David R Liu. Rewritable multi-event analog recording in bacterial and mammalian cells. *Science*, 360(6385):eaap8992, 2018.

[30] Shalni Kumar, Andrew Lezia, and Jeff Hasty. Engineering plasmid copy number heterogeneity for dynamic microbial adaptation. *Nature microbiology*, 9(8):2173–2184, 2024.

[31] Shalni Kumar, Andrew Lezia, and Jeff Hasty. Exploiting heterogeneity in coupled, two plasmid systems for dynamic population adaptation. *bioRxiv*, pages 2023–02, 2023.

[32] Adrian Racovita, Satya Prakash, Clenira Varela, Mark Walsh, Roberto Galizi, Mark Isalan, and Alfonso Jaramillo. Engineered gene circuits capable of reinforcement learning allow bacteria to master gameplaying. *bioRxiv*, pages 2022–04, 2022.

[33] Paige Steppe, Camilo Rey-Bedón, Shalni Kumar, Emerald Forrest, Niklas Van Der Wagt, Arnav Tayal, Lev Tsimring, and Jeff Hasty. Phenotypic patterning through copy number adaptation to environmental gradients. *ACS synthetic biology*, 13(3):728–735, 2024.

[34] Martin Ackermannk. A functional perspective on phenotypic heterogeneity in microorganisms. *Nature Reviews Microbiology*, 13(8):497–508, 2015.

[35] Domitilla Del Vecchio, Yili Qian, Richard M. Murray, and Eduardo D. Sontag. Future systems and control research in synthetic biology. *Annual Reviews in Control*, 45:5–17, 2018.

[36] Leila M. Reyes Ruiz, Caitlin L. Williams, and Rita Tamayo. Enhancing bacterial survival through phenotypic heterogeneity. *PLOS Pathogens*, 16(5):e1008439, May 2020.

[37] Ard Jan Grimbergen, Jeroen Siebring, Ana Solopova, and Oscar P Kuipers. Microbial bet-hedging: the power of being different. *Current Opinion in Microbiology*, 25:67–72, June 2015.

[38] Catherine R Armbruster, Calvin K Lee, Jessica Parker-Gilham, Jaime De Anda, Aiguo Xia, Kun Zhao, Keiji Murakami, Boo Shan Tseng, Lucas R Hoffman, Fan Jin, Caroline S Harwood, Gerard Cl Wong, and Matthew R Parsek. Heterogeneity in surface sensing suggests a division of labor in Pseudomonas aeruginosa populations. *eLife*, 8:e45084, June 2019.

[39] Arjun Raj and Alexander Van Oudenaarden. Nature, Nurture, or Chance: Stochastic Gene Expression and Its Consequences. *Cell*, 135(2):216–226, October 2008.

[40] HarleyH. McAdams and Adam Arkin. Stochastic mechanisms in gene expression. *Proceedings of the National Academy of Sciences*, 94(3):814–819, February 1997.

[41] John R. S. Newman, Sina Ghaemmaghami, Jan Ihmels, David K. Breslow, Matthew Noble, Joseph L. DeRisi, and Jonathan S. Weissman. Single-cell proteomic analysis of S. cerevisiae reveals the architecture of biological noise. *Nature*, 441(7095):840–846, June 2006.

[42] Arren Bar-Even, Johan Paulsson, Narendra Maheshri, Miri Carmi, Erin O'Shea, Yitzhak Pilpel, and Naama Barkai. Noise in protein expression scales with natural protein abundance. *Nature Genetics*, 38(6):636–643, June 2006.

[43] Olin K. Silander, Nela Nikolic, Alon Zaslaver, Anat Bren, Ilya Kikoin, Uri Alon, and Martin Ackermann. A Genome-Wide Analysis of Promoter-Mediated Phenotypic Noise in Escherichia coli. *PLoS Genetics*, 8(1):e1002443, January 2012.

[44] Roy D. Dar and Ron Weiss. Perspective: Engineering noise in biological systems towards predictive stochastic design. *APL Bioengineering*, 2(2):020901, June 2018.

[45] Nathalie Q. Balaban, Jack Merrin, Remy Chait, Lukasz Kowalik, and Stanislas Leibler. Bacterial Persistence as a Phenotypic Switch. *Science*, 305(5690):1622–1625, September 2004.

[46] Miles V Rouches, Yasu Xu, Louis Brian Georges Cortes, and Guillaume Lambert. A plasmid system with tunable copy number. *Nature Communications*, 13(1):3908, 2022.

[47] Isaac N Nuñez, Tamara F Matute, Ilenne D Del Valle, Anton Kan, Atri Choksi, Drew Endy, Jim Haseloff, Timothy J Rudge, and Fernan Federici. Artificial symmetry-breaking for morphogenetic engineering bacterial colonies. *ACS synthetic biology*, 6(2):256–265, 2017.

[48] Thomas G Bernhardt, William D Roof, and Ry Young. Genetic evidence that the bacteriophage φx174 lysis protein inhibits cell wall synthesis. *Proceedings of the National Academy of Sciences*, 97(8):4297–4302, 2000.

[49] Sonali Gupta, Tyler D Ross, Marcella M Gomez, Job L Grant, Philip A Romero, and Ophelia S Venturelli. Investigating the dynamics of microbial consortia in spatially structured environments. *Nature communications*, 11(1):2418, 2020.

[50] Dmitri Volfson, Scott Cookson, Jeff Hasty, and Lev S Tsimring. Biomechanical ordering of dense cell populations. *Proceedings of the National Academy of Sciences of the United States of America*, 105(40):15346–15351, October 2008.

[51] Timothy J Rudge, Paul J Steiner, Andrew Phillips, and Jim Haseloff. Computational modeling of synthetic microbial biofilms. *ACS synthetic biology*, 1(8):345–352, 2012.

[52] Seunghee S Jang, Kevin T Oishi, Robert G Egbert, and Eric Klavins. Specification and simulation of synthetic multicelled behaviors. *ACS synthetic biology*, 1(8):365–374, 2012.

[53] Karthik Nagarajan, Congjian Ni, and Ting Lu. Agent-based modeling of microbial communities. *ACS synthetic biology*, 11(11):3564–3574, 2022.

[54] Mya R Warren, Hui Sun, Yue Yan, Jonas Cremer, Bo Li, and Terence Hwa. Spatiotemporal establishment of dense bacterial colonies growing on hard agar. *Elife*, 8:e41093, 2019.

[55] Cheemeng Tan, Philippe Marguet, and Lingchong You. Emergent bistability by a growth-modulating positive feedback circuit. *Nature chemical biology*, 5(11):842–848, 2009.

[56] Javier Santos-Moreno and Yolanda Schaerli. Using synthetic biology to engineer spatial patterns. *Advanced Biosystems*, 3(4):1800280, 2019.

[57] Subhayu Basu, Yoram Gerchman, Cynthia H Collins, Frances H Arnold, and Ron Weiss. A synthetic multicellular system for programmed pattern formation. *Nature*, 434(7037):1130–1134, 2005.

[58] Nan Luo, Shangying Wang, and Lingchong You. Synthetic pattern formation. *Biochemistry*, 58(11):1478–1483, 2019.

[59] Arianna Miano, Michael J Liao, and Jeff Hasty. Inducible cell-to-cell signaling for tunable dynamics in microbial communities. *Nature communications*, 11(1):1193, 2020.

[60] Andres Cubillos-Ruiz, Tingxi Guo, Anna Sokolovska, Paul F. Miller, James J. Collins, Timothy K. Lu, and Jose M. Lora. Engineering living therapeutics with synthetic biology. *Nature Reviews Drug Discovery*, 20(12):941–960, 2021.

[61] Michael A Fischbach, Jeffrey A Bluestone, and Wendell A Lim. Cell-based therapeutics: the next pillar of medicine. *Science translational medicine*, 5(179):179ps7–179ps7, 2013.

[62] Christopher A Voigt. Synthetic biology 2020–2030: six commercially-available products that are changing our world. *Nature Communications*, 11(1):6379, 2020.

[63] Neil S Forbes. Engineering the perfect (bacterial) cancer therapy. *Nature Reviews Cancer*, 10(11):785–794, 2010.

[64] M. Omar Din, Tal Danino, Arthur Prindle, Matt Skalak, Jangir Selimkhanov, Kaitlin Allen, Ellixis Julio, Eta Atolia, Lev S. Tsimring, Sangeeta N. Bhatia, and Jeff Hasty. Synchronized cycles of bacterial lysis for in vivo delivery. *Nature*, 536(7614):81–85, 2016.

[65] Robert M. Cooper, Josephine A. Wright, Jia Q. Ng, Jarrad M. Goyne, Nobumi Suzuki, Young K. Lee, Mari Ichinose, Georgette Radford, Feargal J. Ryan, Shalni Kumar, Elaine M. Thomas, Laura Vrbanac, Rob Knight, Susan L. Woods, Daniel L. Worthley, and Jeff Hasty. Engineered bacteria detect tumor dna. *Science*, 381(6658):682–686, 2023.

[66] Xuefei Angelina Nou and Christopher A Voigt. Sentinel cells programmed to respond to environmental dna including human sequences. *Nature Chemical Biology*, 20(2):211–220, 2024.

[67] Katherine O'Connor, Paige Steppe, Daniel Worthley, Jeff Hasty, and Robert Cooper. Bacteria as living biosensors for dna. *Nature Reviews Bioengineering*, pages 1–13, 2025.

[68] Baylee J. Russell, Steven D. Brown, Nicole Siguenza, Irene Mai, Anand R. Saran, Amulya Lingaraju, Erica S. Maissy, Ana C. Dantas Machado, Antonio F. M. Pinto, Concepcion Sanchez, Leigh-Ana Rossitto, Yukiko Miyamoto, R. Alexander Richter, Samuel B. Ho, Lars Eckmann, Jeff Hasty, David J. Gonzalez, Alan Saghatelian, Rob Knight, and Amir Zarrinpar. Intestinal transgene delivery with native *E. coli* chassis allows persistent physiological changes. *Cell*, 185(17):3263–3277.e15, 2022.

[69] Xiaowu Bai, Ziyu Huang, Anna M Duraj-Thatte, Matthias P Ebert, Fen Zhang, Elke Burgermeister, Xue Liu, Benjamin M Scott, Guoxin Li, and Tao Zuo. Engineering the gut microbiome. *Nature Reviews Bioengineering*, 1(9):665–679, 2023.

[70] David T. Riglar and Pamela A. Silver. Engineering bacteria for diagnostic and therapeutic applications. *Nature Reviews Microbiology*, 16(4):214–225, 2018.

[71] Lu Zhao, Jiaoyu Xin, Mingyang Hu, Chenyu Xue, and Na Dong. Programmable microbial therapeutics: advances in engineered bacteria for targeted in vivo delivery and precision medicine. *Journal of Advanced Research*, 2025.

[72] Ana P Teixeira and Martin Fussenegger. Synthetic gene circuits for regulation of next-generation cell-based therapeutics. *Advanced Science*, 11(8):2309088, 2024.

[73] Jens Puschhof, Cayetano Pleguezuelos-Manzano, and Hans Clevers. Organoids and organs-on-chips: Insights into human gut-microbe interactions. *Cell host & microbe*, 29(6):867–878, 2021.

[74] Soudamini Chintalapati, Nina Sang, Mikako Miyahara, Seigo Iwata, Kei Nishida, and Eijiro Miyako. Living drugs: A wonderful evolution for therapeutic applications. *Cell Biomaterials*, 2025.

[75] Mark R Charbonneau, Vincent M Isabella, Ning Li, and Caroline B Kurtz. Developing a new class of engineered live bacterial therapeutics to treat human diseases. *Nature communications*, 11(1):1738, 2020.

[76] Joseph McFarland. The nephelometer: an instrument for estimating the number of bacteria in suspensions used for calculating the opsonic index and for vaccines. *Journal of the American Medical Association*, 49(14):1176–1178, 1907.

[77] Jacob Beal, Natalie G Farny, Traci Haddock-Angelli, Vinoo Selvarajah, Geoff S Baldwin, Russell Buckley-Taylor, Markus Gershater, Daisuke Kiga, John Marken, Vishal Sanchania, et al. Robust estimation of bacterial cell count from optical density. *Communications biology*, 3(1):512, 2020.

[78] Matthew R Bennett and Jeff Hasty. Microfluidic devices for measuring gene network dynamics in single cells. *Nature Reviews Genetics*, 10(9):628–638, 2009.

[79] Mike S Ferry, Ivan A Razinkov, and Jeff Hasty. Microfluidics for synthetic biology: from design to execution. In *Methods in enzymology*, volume 497, pages 295–372. Elsevier, 2011.

[80] Chiara Leal-Alves, Zhiyang Deng, Natalia Kermeci, and Steve CC Shih. Integrating microfluidics and synthetic biology: advancements and diverse applications across organisms. *Lab on a Chip*, 24(11):2834–2860, 2024.

[81] Donald E. Ingber. Human organs-on-chips for disease modelling, drug development and personalized medicine. *Nature Reviews Genetics*, 23:467–491, 2022.

[82] Dongeun Huh, Benjamin D Matthews, Akiko Mammoto, Martín Montoya-Zavala, Hong Yuan Hsin, and Donald E Ingber. Reconstituting organ-level lung functions on a chip. *Science*, 328(5986):1662–1668, 2010.

[83] Chak Ming Leung, Pim De Haan, Kacey Ronaldson-Bouchard, Ge-Ah Kim, Jihoon Ko, Hoon Suk Rho, Zhu Chen, Pamela Habibovic, Noo Li Jeon, Shuichi Takayama, et al. A guide to the organ-on-a-chip. *Nature Reviews Methods Primers*, 2(1):33, 2022.

[84] Yimu Zhao, Shira Landau, Sargol Okhovatian, Chuan Liu, Rick Xing Ze Lu, Benjamin Fook Lun Lai, Qinghua Wu, Jennifer Kieda, Krisco Cheung, Shravanthi Rajasekar, et al. Integrating organoids and organ-on-a-chip devices. *Nature Reviews Bioengineering*, 2(7):588–608, 2024.

[85] Sharath M. Bhat, Vaishnavi A. Badiger, Sampara Vasishta, Juhi Chakraborty, Seetharam V. Prasad, Kartik J. Rangarajan, Ashok M. Raichur, and Santanu Dhara. 3d tumor angiogenesis models: recent advances and challenges. *Journal of Cancer Research and Clinical Oncology*, 147:3477–3494, 2021.

[86] Beyza Bulutoglu, Camilo Rey-Bedón, Yoon-Been A. Kang, Sevgi Mert, Martin L. Yarmush, and Oben B. Usta. A microfluidic patterned model of non-alcoholic fatty liver disease: applications to disease progression and zonation. *Lab on a Chip*, 19(18):3022–3031, 2019.

[87] Paul M. Holloway, Sandrine Willaime-Morawek, Richard Siow, Melissa Barber, Roísín M. Owens, Anup D. Sharma, Wendy Rowan, Eric Hill, and Michele Zagnoni. Advances in microfluidic in vitro systems for neurological disease modeling. *Journal of Neuroscience Research*, 99(5):1276–1307, 2021.

[88] Marzieh Ramezani Farani, Saber Saharkhiz, Kimia Feiz, Iraj Alipourfard, and Yun Suk Huh. Microbiome on a chip: a promising technology for modeling of human organ microbiomes and their interactions. *Critical Reviews in Biotechnology*, pages 1–16, 2025.

[89] Raquel Alonso-Roman, Alexander S Mosig, Marc Thilo Figge, Kai Papenfort, Christian Eggeling, Felix H Schacher, Bernhard Hube, and Mark S Gresnigt. Organ-on-chip models for infectious disease research. *Nature microbiology*, 9(4):891–904, 2024.

[90] M Tyler Nelson, Mark R Charbonneau, Heidi G Coia, Mary J Castillo, Corey Holt, Eric S Greenwood, Peter J Robinson, Elaine A Merrill, David Lubkowicz, and Camilla A Mauzy. Characterization of an engineered live bacterial therapeutic for the treatment of phenylketonuria in a human gut-on-a-chip. *Nature communications*, 12(1):2805, 2021.

[91] Woojung Shin and Hyun Jung Kim. 3d in vitro morphogenesis of human intestinal epithelium in a gut-on-a-chip or a hybrid chip with a cell culture insert. *Nature protocols*, 17(3):910–939, 2022.

[92] Chunching Li, Liliang Ouyang, James PK Armstrong, and Molly M Stevens. Advances in the fabrication of biomaterials for gradient tissue engineering. *Trends in Biotechnology*, 39(2):150–164, 2021.

[93] Young Bok Kang, Jinsu Eo, Beyza Bulutoglu, Martin L Yarmush, and O Berk Usta. Progressive hypoxia-on-a-chip: An in vitro oxygen gradient model for capturing the effects of hypoxia on primary hepatocytes in health and disease. *Biotechnology and bioengineering*, 117(3):763–775, 2020.

[94] Zhou Chen, Fangfang Han, Yan Du, Huaqing Shi, and Wence Zhou. Hypoxic microenvironment in cancer: molecular mechanisms and therapeutic interventions. *Signal transduction and targeted therapy*, 8(1):70, 2023.

[95] Yu-Yu Cheng, Zhengyi Chen, Xinyun Cao, Tyler D Ross, Tanya G Falbel, Briana M Burton, and Ophelia S Venturelli. Programming bacteria for multiplexed dna detection. *Nature communications*, 14(1):2001, 2023.

[96] Lindsey Albenberg, Tatiana V Esipova, Colleen P Judge, Kyle Bittinger, Jun Chen, Alice Laughlin, Stephanie Grunberg, Robert N Baldassano, James D Lewis, Hongzhe Li, et al. Correlation between intraluminal oxygen gradient and radial partitioning of intestinal microbiota. *Gastroenterology*, 147(5):1055–1063, 2014.

[97] Michael J Liao, Arianna Miano, Chloe B Nguyen, Lin Chao, and Jeff Hasty. Survival of the weakest in non-transitive asymmetric interactions among strains of *E. coli*. *Nature Communications*, 11(1):6055, 2020.

[98] Tetsuhiro Harimoto, Zakary S Singer, Oscar S Velazquez, Joanna Zhang, Samuel Castro, Taylor E Hinchliffe, William Mather, and Tal Danino. Rapid screening of engineered microbial therapies in a 3d multicellular model. *Proceedings of the National Academy of Sciences*, 116(18):9002–9007, 2019.

[99] BL Adams. The next generation of synthetic biology chassis: moving synthetic biology from the laboratory to the field. acs synth biol 5: 1328–1330, 2016.

[100] Xiangcheng Zhao, Nuli Xie, Hailong Zhang, Wenhu Zhou, and Jinsong Ding. Bacterial drug delivery systems for cancer therapy:"why" and "how". *Pharmaceutics*, 15(9):2214, 2023.

[101] Robert M Cooper, Josephine A Wright, Jia Q Ng, Jarrad M Goyne, Nobumi Suzuki, Young K Lee, Mari Ichinose, Georgette Radford, Feargal J Ryan, Shalni Kumar, et al. Engineered bacteria detect tumor dna. *Science*, 381(6658):682–686, 2023.

[102] John F Toso, Vee J Gill, Patrick Hwu, Francesco M Marincola, Nicholas P Restifo, Douglas J Schwartzentruber, Richard M Sherry, Suzanne L Topalian, James C Yang, Frida Stock, et al. Phase i study of the intravenous administration of attenuated salmonella typhimurium to patients with metastatic melanoma. *Journal of clinical oncology*, 20(1):142–152, 2002.

[103] Shibin Zhou, Claudia Gravekamp, David Bermudes, and Ke Liu. Tumour-targeting bacteria engineered to fight cancer. *Nature Reviews Cancer*, 18(12):727–743, 2018.

[104] Seong-Young Kwon, Hien Thi-Thu Ngo, Jinbae Son, Yeongjin Hong, and Jung-Joon Min. Exploiting bacteria for cancer immunotherapy. *Nature reviews Clinical oncology*, 21(8):569–589, 2024.

[105] Mansour Sedighi, Abed Zahedi Bialvaei, Michael R Hamblin, Elnaz Ohadi, Arezoo Asadi, Masoumeh Halajzadeh, Vahid Lohrasbi, Nima Mohammadzadeh, Taghi Amiriani, Marcela Krutova, et al. Therapeutic bacteria to combat cancer; current advances, challenges, and opportunities. *Cancer medicine*, 8(6):3167–3181, 2019.

[106] Tetsuhiro Harimoto and Tal Danino. Engineering bacteria for cancer therapy. *Emerging topics in life sciences*, 3(5):623–629, 2019.

[107] Xiaotu Ma, Xiaolong Liang, Yao Li, Qingqing Feng, Keman Cheng, Nana Ma, Fei Zhu, Xinjing Guo, Yale Yue, Guangna Liu, et al. Modular-designed engineered bacteria for precision tumor immunotherapy via spatiotemporal manipulation by magnetic field. *Nature Communications*, 14(1):1606, 2023.

[108] Rohita Roy and Michaëlle N Mayalu. Design of a modular inducible circuit for pulsatile population control of engineered bacteria. *bioRxiv*, pages 2025–05, 2025.

[109] Andrew Lezia, Nicholas Csicsery, and Jeff Hasty. Design, mutate, screen: multiplexed creation and arrayed screening of synchronized genetic clocks. *Cell Systems*, 13(5):365–375, 2022.

[110] David S Glass, Anat Bren, Elizabeth Vaisbourd, Avi Mayo, and Uri Alon. A synthetic differentiation circuit in escherichia coli for suppressing mutant takeover. *Cell*, 187(4):931–944, 2024.

[111] Noreen Wauford, Akshay Patel, Jesse Tordoff, Casper Enghuus, Andrew Jin, Jack Toppen, Melissa L Kemp, and Ron Weiss. Synthetic symmetry breaking and programmable multicellular structure formation. *Cell systems*, 14(9):806–818, 2023.

[112] Ronghui Zhu, Jesus M del Rio-Salgado, Jordi Garcia-Ojalvo, and Michael B Elowitz. Synthetic multistability in mammalian cells. *Science*, 375(6578):eabg9765, 2022.

[113] Imen Tanniche and Bahareh Behkam. Engineered live bacteria as disease detection and diagnosis tools. *Journal of Biological Engineering*, 17(1):65, 2023.

[114] Troels Holger Vaaben, Ruben Vazquez-Uribe, and Morten Otto Alexander Sommer. Characterization of eight bacterial biosensors for microbial diagnostic and therapeutic applications. *ACS Synthetic Biology*, 11(12):4184–4192, 2022.

[115] Zhuo Feng, Yuchen Wang, Haiheng Xu, Yunfei Guo, Wen Xia, Chenxuan Zhao, Xiaozhi Zhao, and Jinhui Wu. Recent advances in bacterial therapeutics based on sense and response. *Acta Pharmaceutica Sinica B*, 13(3):1014–1027, 2023.

[116] Yuanli Gao, Lei Wang, and Baojun Wang. Customizing cellular signal processing by synthetic multi-level regulatory circuits. *Nature Communications*, 14(1):8415, 2023.

[117] Leo Baumgart, William Mather, and Jeff Hasty. Synchronized dna cycling across a bacterial population. *Nature genetics*, 49(8):1282–1285, 2017.

[118] Bianca Striednig and Hubert Hilbi. Bacterial quorum sensing and phenotypic heterogeneity: how the collective shapes the individual. *Trends in Microbiology*, 30(4):379–389, 2022.

[119] Alma Dal Co, Charlotte Brannon, and Martin Ackermann. Division of labor in bacteria. *Elife*, 7:e38578, 2018.

[120] Ryan Tsoi, Feilun Wu, Carolyn Zhang, Sharon Bewick, David Karig, and Lingchong You. Metabolic division of labor in microbial systems. *Proceedings of the National Academy of Sciences*, 115(10):2526–2531, 2018.

[121] Mary L Delaney and Andrew B Onderdonk. Evaluation of the anaeropack system for growth of clinically significant anaerobes. *Journal of clinical microbiology*, 35(3):558–562, 1997.